PHOTONIC STRUCTURES BASED ON HYBRID NANOCOMPOSITES

By

Saima Husaini

A dissertation submitted to the Graduate Faculty in Physics in partial fulfillment of the requirements for the degree of Doctor of Philosopy,
The City University of New York
2011

© 2011
Saima Husaini
All Rights Reserved

This manuscript has been read and accepted for the
Graduate Faculty in Physics in satisfaction of the dissertation
requirement for the degree of Doctor of Philosophy.

Prof. Vinod M. Menon
Name

Date

Chair of Examining Committee

Prof. Steven Greenbaum
Name

Date

Executive Officer

Prof. Sajan Saini

Prof. Igor Kuskovsky

Prof. Lev Deych

Supervisory Committee

THE CITY UNIVERSITY OF NEW YORK

ABSTRACT

Photonic Structures Based on Hybrid Nanocomposites

by

Saima Husaini

Advisor: Professor Vinod M. Menon

In this thesis, photonic structures embedded with two types of nanomaterials, (i) quantum dots and (ii) metal nanoparticles are studied. Both of these exhibit optical and electronic properties different from their bulk counterpart due to their nanoscale physical structure. By integrating these nanomaterials into photonic structures, in which the electromagnetic field can be confined and controlled via modification of geometry and composition, we can enhance their linear and nonlinear optical properties to realize functional photonic structures.

Before embedding quantum dots into photonic structures, we study the effect of various host matrices and fabrication techniques on the optical properties of the colloidal quantum dots. The two host matrices of interest are SU8 and PMMA. It is shown that the emission properties of the quantum dots are significantly altered in these host matrices (especially SU8) and this is attributed to a high rate of nonradiative quenching of the dots. Furthermore, the effects of fabrication techniques on the optical properties of quantum dots are also investigated. Finally a microdisk resonator embedded with quantum dots is fabricated using soft lithography and luminescence from the quantum dots in the disk is observed.

We investigate the absorption and effective index properties of silver nanocomposite films. It is shown that by varying the fill factor of the metal nanoparticles and fabrication parameters such as heating time, we can manipulate the optical properties of the metal nanocomposite. Optimizing these parameters, a silver nanocomposite film with a 7% fill factor is prepared. A one-dimensional photonic crystal consisting of alternating layers of the silver nanocomposite and a polymer (Polymethyl methacrylate) is fabricated using spin coating and its linear and nonlinear optical properties are investigated. Using reflectivity measurements we demonstrate that the one-dimensional silver-nanocomposite-dielectric photonic crystal exhibits a 200% enhancement of the reflection band which is attributed to the interplay between the plasmon resonance of the silver nanoparticles and the Bloch modes of the photonic crystal.

Nonlinear optical studies on this one-dimensional silver-nanocomposite-dielectric structure using z-scan measurements are conducted. These measurements indicate a three-fold enhancement in the nonlinear absorption coefficient when compared to a single film of comparable metal composite thickness.

ACKNOWLEDGEMENTS

"It was the best of times, it was the worst of times, it was the age of wisdom, it was the age of foolishness, it was the epoch of belief, it was the epoch of incredulity, it was the season of Light, it was the season of Darkness, it was the spring of hope, it was the winter of despair."

Charles Dickens opened his tale of two cities with these words. For me, however, they describe everything that could be said for the past five years of my life with unerring accuracy. Having survived those moments of insanity where everything threatened to fall apart – from my experiments to the somewhat vulnerable grey matter - I am compelled to thank a number of people for bearing with me with the patience and the fortitude that I did not always deserve.

This thesis would not have been made possible without the constant guidance, motivation and support of my advisor and mentor, Professor Vinod Menon, who has a way of bringing out the best in even the most obtuse and trying of students. Learning under his tutelage has been an immense privilege and I am grateful for having had the opportunity.

I must also thank David Goldberg, Harish Krishnamoorthy and Bidisha Roy for their continuous assistance, counsel and friendship. I would have been unable to reach this far without David's constant vigilance and annoying perfectionism over the years, which in the end turned out to be exactly what I needed to counteract my own eccentric behavior. An equal amount of thanks goes to Harish for his unbelievable forbearance. Whatever

little sanity I have left, I owe to Bidisha who was always around to offer some valuable perspective.

My thesis would not have materialized without the valuable support and advice of my thesis committee – Professor Deych, Professor Kuskovsky, Professor Kowach and Professor Saini – who were always willing to offer suggestions on how to better my work.

I would also like to thank Dr Matt Sfier and Dr Dmytro Nykypanchuk from the Brookhaven National Laboratory for opening their labs for me when I needed to use their facilities in order to complete my research.

This thesis would not have survived the days of stagnant despair and seeming hopelessness without the unshakable belief and unfailing support of my family. I would like to thank my husband, Mirza, for his constant encouragement and conviction in my work, my cousins, Rabia and Ahmed, for their much appreciated humor and relentless optimism, my sister, Saira, for her undying faith in my efforts and my grandmother, Rashida Muzaffar, who instilled in me the value of science and the difference it can make.

Lastly, I would like to thank my parents, Salma and Majeedullah Husaini, for their unyielding belief, support and encouragement. It is to them that I dedicate this thesis.

Table of Contents

LIST OF FIGURES

OVERVIEW OF THESIS

The thesis is organized as follows. The first chapter introduces the theoretical framework of the nanomaterials as pertaining to the work done in this thesis. The intention of this chapter is to familiarize the reader with the fundamental optical properties of quantum dots and metal nanoparticles and discuss the factors that contribute to their spectral properties.

Chapter 2 covers details of experimental techniques used in this thesis. The first part of this chapter covers specifics of the optical techniques and the second part gives a general overview of fabrication techniques carried out. Details and specifics of fabrication techniques however, are discussed accordingly in each section pertaining to the work.

Chapter 3 focuses on the work done solely using colloidal quantum dots. The first section presents results obtained on the investigation of the dependence of the optical properties of the quantum dots on the host and fabrication techniques. The chapter aims to give the reader an overview of fabrication techniques compatible with the integration of colloidal quantum dots in photonic structures. Finally, optical characterization of a microdisk embedded with quantum dots is presented

The first part of chapter 4 focuses on the linear and nonlinear optical properties of single metal nanocomposite film. The Maxwell Garnett effective medium theory is also discussed. The second part of this chapter reports on the linear and nonlinear properties of the one-dimensional photonic crystal embedded with the metal nanocomposite.

Chapter 1. THEORY OF NANOMATERIALS

The inclusion of nanomaterials in photonic structures has been a topic of research not only in the academic arena but also in industry due to their wide range of potential applications. However, these nanomaterials by themselves, exhibit a wide array of interesting optical properties. This chapter briefly discusses basic concepts of two types of nanomaterials (i) Quantum Dots and (ii) Metal Nanoparticles and explains the physics behind their optical properties and the factors that distinguish them from their bulk equivalent. The chapter is divided into two sections. The first section outlines the basic optical properties and typical fabrication methods of quantum dots with an emphasis on colloidal quantum dots. The second section lays down basic principles put forth over decades to describe optical behavior of metals. Also optical properties of metal nanoparticles are discussed and focus is given on differentiating properties of metal nanoparticles from their bulk counterpart. The section ends with an overview of nonlinear optical processes in metals.

1.1 QUANTUM DOTS

1.1.1. CHARACTERISTICS OF QUANTUM DOTS

In recent years quantum dots (QDs) have attracted much interest due to their unique spectral properties. As a diverse class of nanomaterials, whose optical and electronic properties can be engineered depending on application they have led to a wide range of potential applications such as solar cells, bio-sensing/imaging, telecommunication, displays and quantum cryptography [1, 2]. QDs are semiconductor nanocrystals having a size of about 2-10nm in diameter, which provide three-dimensional confinement for conduction band electrons and valence band holes. The most exciting feature of QDs is

their size dependence on their optical properties. One of the defining features in a semiconductor is its band gap which separates the conduction and valance energy bands and determines the energy of photon absorption and emission (in the case of direct bandgap semiconductors). In bulk semiconductors this gap is a fixed parameter depending on the semiconductor material. When radiation of sufficient energy is incident upon a semiconductor an electron-hole pair (exciton) is produced. The excitons in a semiconductor can be described by a hydrogen-like Hamiltonian [3, 4]:

$$\hat{H} = \frac{\hbar^2}{2m_h}\nabla_h^2 - \frac{\hbar^2}{2m_e}\nabla_e^2 - \frac{e^2}{\varepsilon|r_e - r_h|} \tag{1.1}$$

The electron-hole possesses a natural physical separation - the Bohr radius:

$$a_B^* = \frac{\hbar^2 \varepsilon}{e^2}\left(\frac{1}{m_e^*} + \frac{1}{m_h^*}\right), \tag{1.2}$$

where m_e^* and m_h^* are the electron and hole effective masses respectively, and ε is the relative dielectric constant of the material. If the diameter d of the semiconductor nanostructure is less than a_B^* then the material is said to be in the strong confinement regime, and when the diameter is larger than a_B^* it is said to be in the weak confinement regime. Hence, as the size of the nanocrystal approaches the limit of the Bohr radius of an exciton, the excitonic states shift to a higher energy as confinement increases. This confinement modifies the electronic and optical properties of the semiconductor which leads to the collapse of continuous energy bands of the bulk semiconductor and leads to discrete set of energy levels shown in Figure 1.1 (a).

Therefore for semiconductor particles with a size smaller than about 10 nm, the last term in the Hamiltonian (equation 1.1) which describes the screened Coulomb interaction between the electron and hole can be neglected and therefore both the electron and hole may be described by a particle-in-a-box (with dimensions l_x ,l_y and l_z) model, where the energy levels have the form [5]:

$$E = \frac{h^2}{8m_e}\left[\left(\frac{n_x}{l_x}\right)^2 + \left(\frac{n_y}{l_y}\right)^2 + \left(\frac{n_z}{l_z}\right)^2\right] \tag{1.3}$$

where the quantum numbers n_x, n_y and n_z can assume integral values 1, 2, 3.

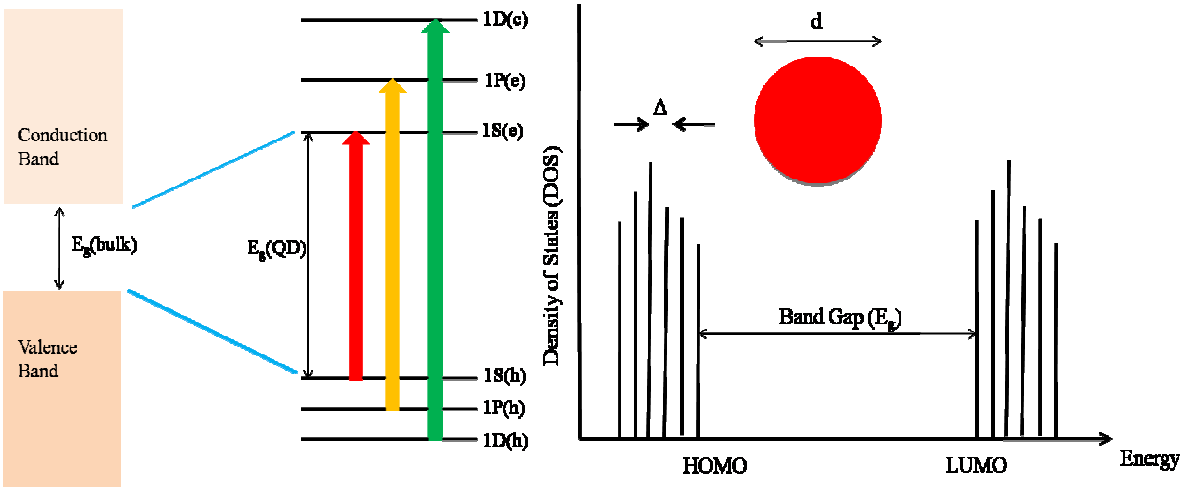

Figure 1.1 (a) Bulk semiconductors have continuous conduction and valence bands which in a semiconductor nanocrystal collapse to form discrete atomic-like states (b) Ideal density of states for a semiconductor QD where the inter-level spacing is indicated as Δ for a dot with diameter d [6,7].

This is the case in a QD where unlike a conventional bulk semiconductor the spatial extent of the electronic wavefunction is comparable to the size of the dot thereby existing at a higher energy relative to the bulk case. Quantum confinement allows the tuning of the bandgap in QDs by altering the size of the QDs, therefore as confinement increases the size of the bandgap increases, leading the interband transitions to blue shift. Therefore

a sufficiently small (~3 nm) QD made using cadmium selenide whose bulk bandgap lies in infrared is able to yield luminescence in the visible.

In a discrete eigen-spectrum such as the one that exists in these semiconductor nanocrystals the analogue of the valence band maximum is known as the highest occupied molecular orbital (HOMO) and that for the conduction band minimum is known as the lowest unoccupied molecular orbital (LUMO). Therefore the HOMO-LUMO gap is the band gap which scales as $E_g(d) \propto \frac{1}{d^{\beta}}$ as seen in Figure 1.1(b) which shows an idealized density of states for a QD of diameter *d*. The value of β varies with different theories but all of these predict it to be in the range of $\beta \in [1,2]$. For the model of a particle in a spherical box (as in Figure 1.1 (b)) β is calculated to be 2. [7]

For a bulk semiconductor, the density of states to a simple approximation is proportional to $E^{1/2}$. However for a QD the confinement of electrons and holes in all three dimensions leads to further quantization of energy levels. The density of states for QDs is given by [5]:

$$D(E) \propto \sum_{E_n} \delta(E - E_n) \tag{1.4}$$

Therefore the density of states instead of producing a continuous distribution have discrete values of $D(E)$ and therefore produce sharp absorption and emission spectra for QDs.

In addition to the size-quantization-effect the sharp discrete energy levels results in an increase of oscillator strength between the energy levels. In the strong confinement regime the oscillator strength of a semiconductor nanocrystal with radius *a* is expected to

increase with $\frac{1}{a^3}$ because of the strong overlap of wavefunctions of the confined electron and hole. For spherical nanoparticles this can be given as [8]:

$$\frac{f}{f_{ex}} = \frac{3}{4}\left(\frac{a_B^*}{a}\right)^3 \tag{1.5}$$

Here f and f_{ex} are the oscillator strengths of the QD and bulk semiconductor respectively.

Quantum dots have large surface-to-volume ratio, which leads to a strong enhancement of surface related phenomena. The surface configuration strongly affects the electronic structure in nanoparticles. For QDs it is seen that a bare surface leads to the creation of surface defects which are detrimental to high luminescence yield. To enhance the quantum efficiency of QDs made of a single semiconductor material, a shell overcoating of a second semiconductor material can be grown over it.

This overcoating gives rise to two types of QD structures- type I and type II. For type I QD structures, a shell made of wider bandgap materials is grown over a small bandgap core. Here the exciton is contained within the core as the electron preferentially populates the LUMO and the hole prefers locating itself at the HOMO. As the carriers are not near the surface, energy transfer mechanisms between the QDs is reduced. In type II the overcoating consists of a material with either a differing or similar bandgap, but grown at an offset relative to the core material's bandgap. This leads to the carriers locating themselves either in the core or shell. Figure 1.2 illustrates this difference with band structure [7, 9-10].

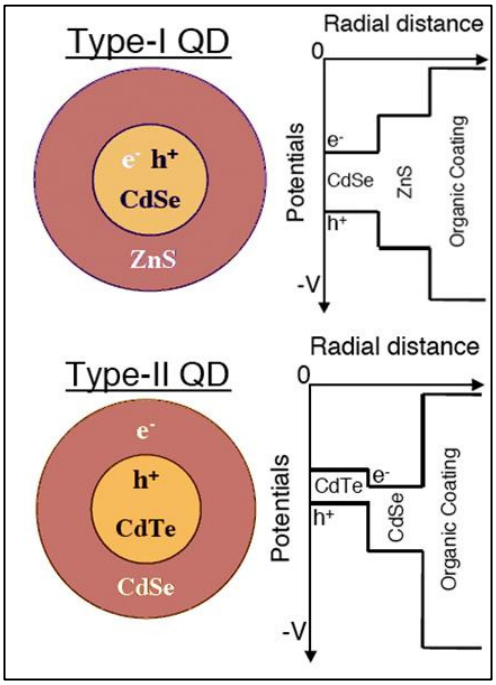

Figure 1.2 Schematic illustration of the band structure (alignment) difference between Type-1 and Type-II core-shell QDs (nanocluster.mit.edu)

1.1.2 FORMATION OF QUANTUM DOTS

Here we discuss the formation of QDs via two main techniques. The first is molecular beam epitaxy (MBE) which is used to form QDs through various methods. The three methods discussed here are [12]: production of QDs using (i) quantum well interface fluctuations (ii) lithographic and (iii) self assembly techniques. The second technique is the formation of QDs through colloidal synthesis. Although QDs formed through MBE techniques are of high quality, this thesis focuses on the optical studies of colloidal QDs due to their compatibility and ease of preparation in the relevant photonic structures discussed in this work.

Methods involving Molecular Beam Epitaxy

Growth using MBE is carried out in an ultrahigh vacuum environment in stainless steel chamber. A schematic of an MBE chamber is shown in Figure. 1.3. It involves evaporation of atoms, which are constituents of the desired semiconductor. The semiconductor constituents are heated in cells called "effusion cells" or "Knudsen cells". The heating of these cells produces a vapor which passes through a small aperture and is accelerated by a pressure differential existing between both sides of the aperture. This creates a beam of atoms directed toward the sample substrate. The required concentration of atoms is attained by controlling the flux density of different beams through temperature control [5].

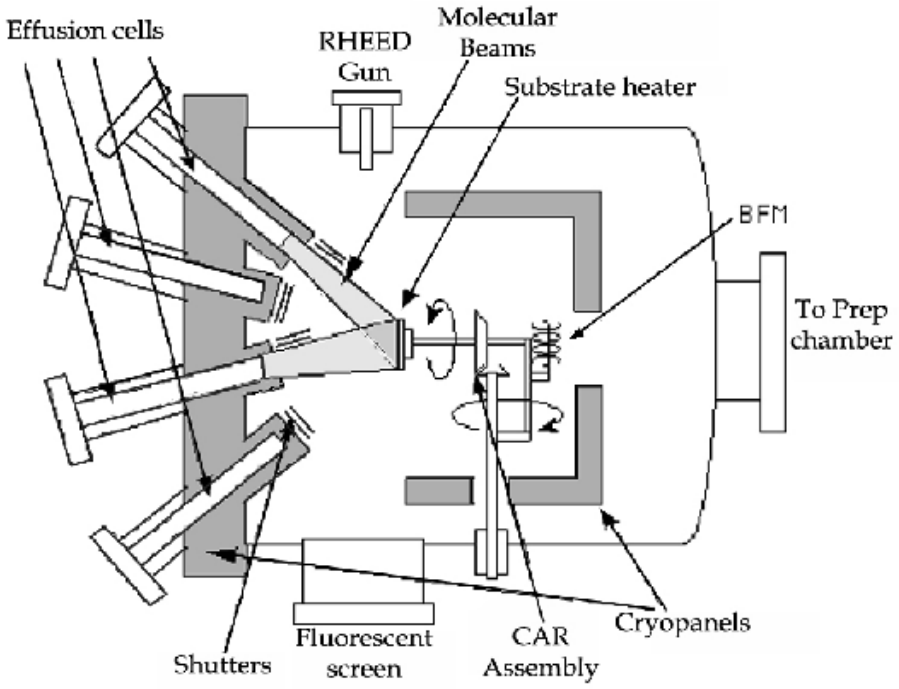

Figure 1.3 Schematic of Molecular Beam Epitaxy System (mxp.physics.umn.edu)

The substrate is also rotated to ensure a uniform deposition on it. Shutters in front of the beam openings are used to control the amount of constituents of the semiconductor alloys. Molecular beam epitaxy is highly attractive due to high quality and low impurity content in the materials grown. In addition the ultrahigh vacuum environment allows many in situ analytical techniques which allow characterization of the growth of the materials and its composition at various levels of spatial resolution.

However the atomic layer precision of MBE also makes growth times longer and therefore less practical for some industrial applications. Furthermore the cost of making MBE systems is not trivial.

(i) QD formed through interface fluctuations

Quantum dots are formed in this manner by interrupting MBE growth of narrow quantum wells (QW). This causes the QW width to fluctuate by one atomic layer (monolayer). The QDs form in the QWs at locations where the material interface accumulates an extra monolayer. The electrons and holes become localized into QDs in regions of the quantum well that are a monolayer thicker than the surrounding region and thereby have smaller confinement energy [11]. The drawback of using this method is that the formations of these dots is somewhat random and render the dots such that they cannot be used in applications that require high degrees of control.

(ii) Lithographically formed quantum dots.

These are created by confining electrons with a voltage applied to metallic leads. A heavily doped, semiconductor heterostructure which contains a high mobility two dimensional electron gas (2DEG) is grown on the substrate. The layer is then capped with the same material as the substrate. Metal electrodes are then patterned on the

heterostructure surface layer through lithographic means. Application of a negative voltage to the metal electrodes electrostatically repels the electrons below creating a shadow of the electrodes in the conducting 2DEG. This leads to the confinement of electrons causing the formation of localized QD. [12]

(ii) Self –Assembled quantum dots

Self assembled QDs form during MBE growth when difference in lattice parameters creates strain. When a semiconductor's lattice structure does not match that of a material and is grown on its substrate, the strain results due to lattice mismatch. During growth a strained film called the "wetting layer" is initially formed. This strain in the wetting layer grows as more monolayers accumulate until it is energetically favorable to form three-dimensional islands on the wetting layer surface. The maximum thickness of the wetting layer is related to the difference in lattice constants between the materials. Beyond this thickness, formation of an array of islands takes place. This method of forming self-assembled dots in semiconductors is known as the Stranski-Krastanov growth method. The shape of these islands can be controlled by altering growth conditions although usually these islands form a truncated pyramidal shape [10, 12].

1.1.3 COLLOIDAL SYNTHESIS OF QUANTUM DOTS

Colloidal QDs are chemically created and suspended in aqueous or organic solutions as shown in Figure 1.4. The nanocrystal size sensitively depends on the formation temperature and solution concentrations. Colloidal QDs are chemically synthesized via

precursor compounds dissolved in solutions. They are made using a three component procedure which consists of precursors, organic surfactants and solvents.

A reaction chamber is prepared with a mixture of compounds responsible for controlling nucleation and growth. Constituents of the desired nanocrystal are introduced into this chamber as precursors. A precursor is a molecule which contains one more of the desired semiconductor species for the nanocrystal.

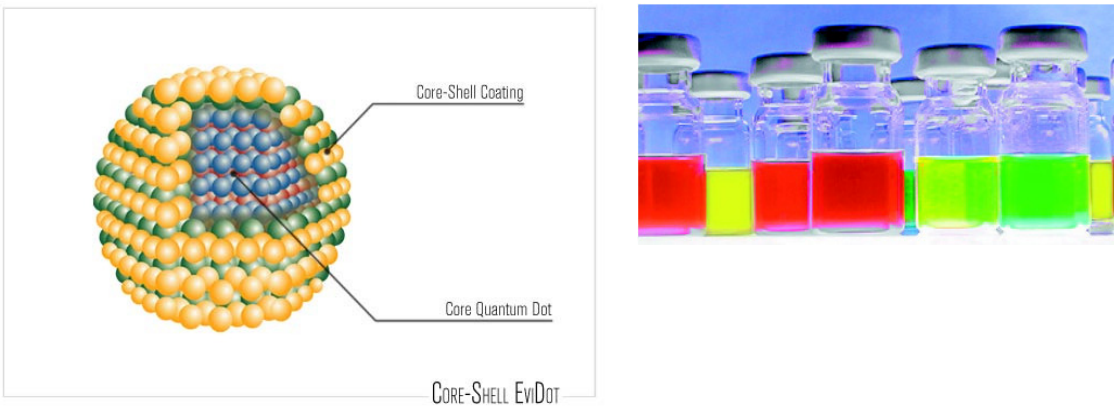

Figure 1.4 (a) Schematic illustration of core-shell QD (b) Various colloidal quantum dot solutions showing range of accessible wavelengths by size tuning. (evidenttech.com)

These precursors decompose to form monomers which eventually cause nucleation and nanocrystal growth. The energy for this decomposition is provided either through temperature control or a chemical reaction between the liquid and the precursors or even a combination of the two. For controlled growth the presence of a surfactant is required. The surfactant is a molecule that under the reaction conditions is adsorbed to the surface of the QD while growing. These surfactants must be chosen so that they are mobile enough to provide access for the addition of monomer units but stable enough to prevent coagulation of the nanocrystals. In addition, if the QD growth is being carried out at high temperatures the surfactant must be able to withstand the temperatures.

Although QDs produced through MBE provide high quality and low impurity samples, this thesis focuses on QDs produced via colloidal synthesis. Colloidal QDs provide various advantageous for the use in photonic structures and devices. They can be dissolved in almost any liquid and provide compatibility with a wide range of substrates including flexible ones. Using colloidal synthesis QDs can be prepared with extreme precision allowing a size dispersion as narrow as 5%. This allows for a greater control of QD emission and absorption as well as tuning of other QD properties efficiently. Also the organic capping prevents coagulation of the nanoparticles and provides stability. The capping also provides surface passivation, which prevents existence of dangling bonds, which may affect the emission efficiency and quantum luminescence yield of the QDs. [5, 13, 14]

1.1.4 Optical Properties of Colloidal quantum dots

In bulk semiconductors wavelength tunability is achieved via changes in the stoichiometry of compounds which leads to further complexities during growth. However colloidal QDs allow a tunable absorption (Figure 1.5) and emission spectrum by control of size.

Quantum dots also produce a very narrow and symmetric emission spectrum as shown in red in Figure 1.6. This is due to the fact that electrons relax to the bottom of the conduction band while the holes scatter to the top of the valence band before recombining. This allows the QDs to emit from the lowest energy state resulting in a narrow FWHM (full width half maximum).

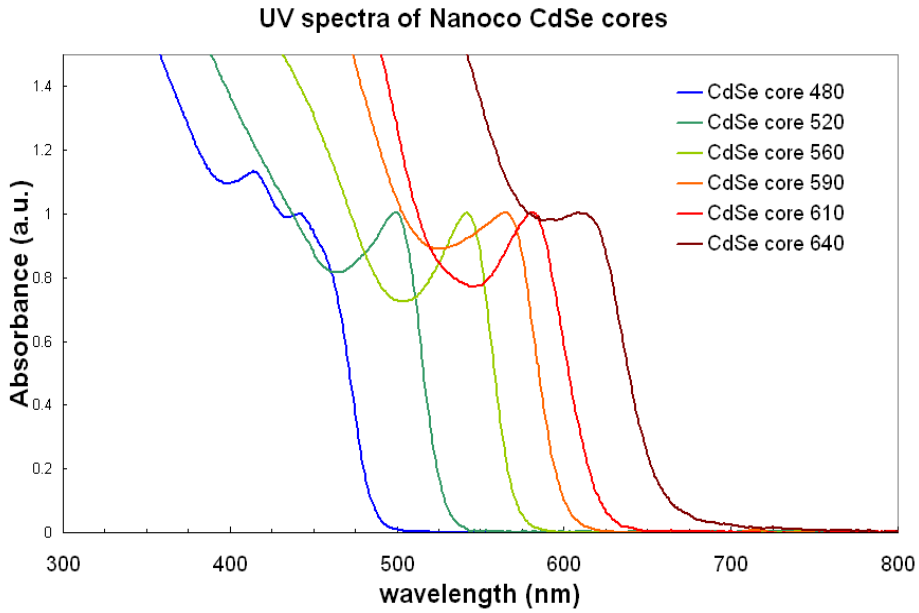

Figure 1.5 Absorbance spectra of colloidal CdSe QDs indicating tunable properties (nanoco technologies.com)

In addition, QDs exhibit very broad absorption spectra at wavelengths shorter than the emission peak. The first excitonic absorption peak occurs at a shorter wavelength than the emission peak due to fast decay to the lowest vibrational level of the first singlet state S_1, and usually to the higher vibrational levels of S_0 and is called the Stoke's shift shown in Figure 1.6. The Stoke's shift is therefore the energy difference between the maximum of the (lowest) excitation band and that of the emission band. The Stoke's shift also arises from solvent effects and/or reaction in the excited states [15].

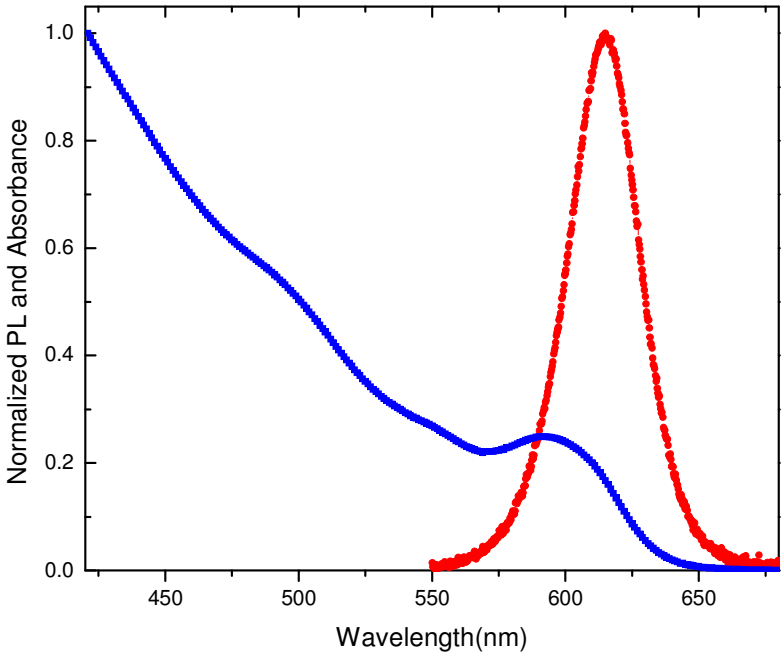

Figure 1.6 Photoluminescence and absorption spectra of colloidal CdSe/ZnS dots in toluene, indicating Stoke's Shift

This thesis focuses on CdSe/ZnS colloidal QDs as shown in Figure 1.4 (a). These dots are typically dispersed in solvents such as hexane and toluene. Figure 1.6 shows a typical photoluminescence and absorption spectra of such dots in toluene.

1.2 METAL NANOPARTICLES

Unlike semiconductor nanocrystals where quantum confinement causes quantization of electron and hole energy states which modify their optical properties, metal nanoparticles produce optoelectronic effects that can be explained using classical electrodynamics. Most applications of metal nanoparticles derive from the local field enhancement due to plasmon resonance induced effect, which leads to various light-induced linear and nonlinear optical phenomena. Metals exhibit significant dispersive properties that can be described via a complex dielectric function, which provides the basis of all phenomena discussed in this section.

1.2.1 ELECTROMAGNETISM IN METAL

We first begin by describing the propagation of light through matter using the macroscopic Maxwell Equations [16, 17]:

$$\begin{aligned} \nabla \times \mathbf{E} &= -\frac{\partial \mathbf{B}}{\partial t}, \\ \nabla \times \mathbf{H} &= \frac{\partial \mathbf{D}}{\partial t} + j, \\ \nabla \cdot \mathbf{D} &= \rho, \\ \nabla \cdot \mathbf{B} &= 0. \end{aligned} \tag{1.6}$$

The field vectors of the electric field **E**, the electric displacement **D**, the magnetic induction **B** and the magnetic field **H** are given related to charge ρ and the current density *j*. To include the material response and describe the light matter interaction, the relative permittivity ε_r and relative permeability μ_r are introduced:

$$\begin{aligned} \boldsymbol{D} &= \varepsilon \boldsymbol{E} = \varepsilon_0 \varepsilon_r \boldsymbol{E} = \varepsilon_0 \boldsymbol{E} + \boldsymbol{P} \\ \boldsymbol{B} &= \mu \boldsymbol{H} = \mu_0 \mu_r \boldsymbol{H} = \mu_0 (\boldsymbol{H} + \boldsymbol{M}) \end{aligned} \tag{1.7}$$

For metals μ_r=1 and $\varepsilon_r = \varepsilon_1 + i\varepsilon_2$. The latter depends on the frequency of the incident electromagnetic field. The refractive index $\tilde{n} = n + ik$ of the material is related to the permittivity and permeability:

$$\begin{aligned} \tilde{n} &= \sqrt{\varepsilon_1 + i\varepsilon_2} \\ \varepsilon_1 &= n^2 - k^2 \\ \varepsilon_2 &= 2nk \end{aligned} \tag{1.8}$$

The imaginary part of the refractive index is related to absorption which is significant in metals. When light travels through matter, it interacts with the material. In classical terms, the electromagnetic light wave polarizes the molecules and atoms. Therefore the electromagnetic wave propagating through the medium is a mix of an electromagnetic wave and a polarization wave [17]:

$$\boldsymbol{P} = \varepsilon_0 (\varepsilon_r(\omega) - 1)\boldsymbol{E} = \varepsilon_0 \chi \boldsymbol{E} \tag{1.9}$$

In materials exhibiting significant dispersion and the existence of a resonance, this combination is called a polariton. The susceptibility $\chi = \varepsilon_r - 1$ gives a measure of polarization of the medium in response to the electric field. Therefore the bound state of a plasmon and an electromagnetic wave is called plasmon-polariton. The polariton propagates along the surface of the metal until it decays either due to absorption or by a radiative transition into a photon.

When the plasmons are excited at the interface of a metal and a dielectric, they are known as surface plasmons. The frequency of excitation of the plasmon depends on the properties of the metal and dielectric and the geometric configuration. Bulk metal plasmons occur at different incident frequencies as compared to metal nanoparticles embedded in a dielectric environment. For structures using bulk metal, optical excitation of the plasmon mode is complicated and requires special coupling geometries.

Two configurations which utilize prism coupling to excite surface plasmons are shown in Figure 1.7. The Kretschmann configuration shown in Figure 1.7 (a) utilizes a prism positioned against a thin metal film to excite surface plasmons and the Otto configuration (Figure 1.7 (b)) shows prism coupling in which the metal film is separated by a dielectric air gap.

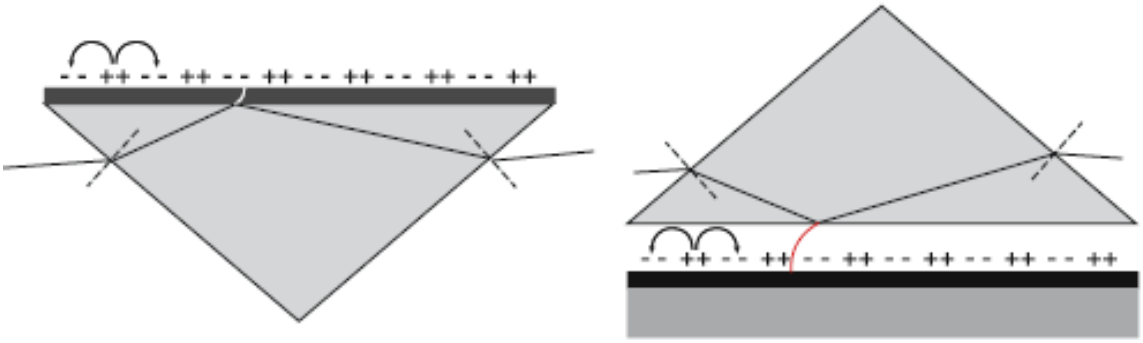

Figure 1.7 Prism coupling of surface plasmon polaritons using (a) Kretschmann and (b) Otto configuration [22].

However, no such geometry is needed to observe the plasmon induced optical properties of metal nanoparticles. When light is incident upon metal nanoparticles, the conduction electrons begin to oscillate due to the oscillating electric field. This causes the electron cloud to be displaced relative to the nucleus. A restoring force comes into place due to the Coulomb attraction between the electrons and the nuclei and the result is a dipole

oscillation (plasma oscillation) of the electron cloud relative to the nuclear frame as shown in Figure 1.8. Therefore the frequency of localized plasmons in metal nanoparticles is different from that of bulk.

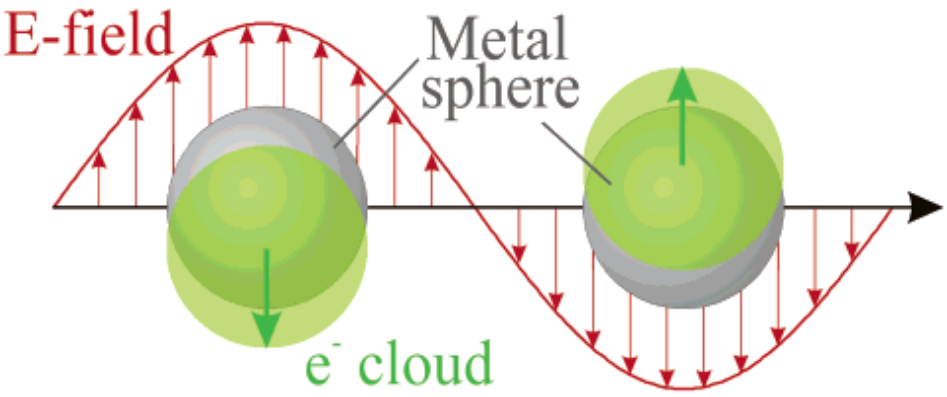

Figure 1.8 Schematics of plasma oscillation due to displacement of electron cloud from nuclei. [26]

With nanoparticles it is possible to directly couple light as the spherical symmetry does not require strict wavevector matching conditions which are needed in surface plasmons. [17]

1.2.2 THEORETICAL BACKGROUND

This section outlines some of the basic theoretical models used to define properties of metal nanoparticles.

Drude Model

In the 1900s Paul Drude developed a model for explanation of electrical conductivity. The Drude model takes a macroscopic view of the charge carriers in metals. The metals are characterized by a cloud of free electrons, that is, they are assumed to be independent

and free and there exists no electron-electron interactions. The model also takes into account frictional damping that may occur due to resistance of motion felt by the moving electrons within the lattice due to the positive stationary ions.

The frequency dependent dielectric function $\varepsilon(\omega)$ of metals can be predicted from the Drude model:

$$\varepsilon(\omega) = \varepsilon_{\infty} - \frac{\omega_p^2}{\omega^2 + i\omega\Gamma_p}$$
$$\omega_p^2 = \frac{ne^2}{\varepsilon_0 m_e} \tag{1.10}$$

Here ω_p is the plasmon frequency of the material, Γ_p is the damping rate, and ε_{∞} is a frequency independent constant that describes the contribution to the permittivity from electron transitions. In the high frequency limit the Drude model is also sometimes referred to as the Lorentz Oscillator Model. [17]

Mie Theory

One of the most popular theories describing metal nanoparticles was introduced by Gustav Mie in 1908 [18]. Mie solved Maxwell's equations for spherical particles in a homogeneous medium and solved for their refractive index in terms of the scattering properties of the metal nanoparticles. The theory predicts the fraction of light that would be absorbed and scattered when light is incident on a metal nanoparticle. The sum of the absorption and scattering is defined as the extinction of light (known as the surface Plasmon band or Plasmon absorbance). The expression for the extinction cross section

for small particles (about 30 nm) with a frequency dependent complex dielectric function $\varepsilon_1 + i\varepsilon_2$ embedded in a medium of dielectric constant ε_m can be expressed as:

$$C_{ext} = \frac{24\pi^2 R^3 \varepsilon_m^{2/3}}{\lambda} \frac{\varepsilon_2}{(\varepsilon_1 + 2\varepsilon_m)^2 + \varepsilon_2^2}, \tag{1.11}$$

where *R* is the radius of the particles. The extinction cross section defined in Eq. (1.11) is therefore defined as the sum of scattering and absorption. The dominating mechanism depends on the size of the particle. For particles in the 50 to 100 nm range, scattering contributes more significantly to the extinction. However as the metal nanoparticles get smaller, absorption becomes the dominating mechanism and the resonance blue-shifts. Therefore as seen from Eq. (1.11), the presence and thereby position of the resonance depends on size of the nanoparticle. The strong color exhibited in metal nanoparticle originates from the existence of the absorption peak at $\varepsilon_1 = -2\varepsilon_m$ [19,20].

1.2.3 Optical Properites of Metal Nanoparticles

One of the most famous objects exhibiting the optical properties of metal nanoparticles is the Lycurgus cup, crafted by the Romans in the 4th century which changes color depending on the light striking it. The cup appears green with reflected light, while in transmission it appears a bright red. Therefore even as early as the 4th century it was known that metal nanoparticles have the property of forming color. However the first notable study of the optical properties determinng color formation in metal nanoparticles was conducted by Michael Faraday [21] in the 1850s. Like QDs, one of the most interesting optical aspects of metal nanoparticles is their dependence on size. In addition

to size, the the optical properties of the metal nanoparticles also depend on their shape, surrounding environment as well as their monodispersity.

Dependence on dielectric environment.

From Mie's expression of the scattering cross section it can be seen that the refractive index of the surrounding environment has a significant role in determing the plasmon resonance of the metal particles. Figure 1.9 shows the scattered light observed by immersing gold nanoparticles (with a radius ~8nm) in solutions with varying refractive index. As seen the scattered light shifts to longer wavelengths when the index increases.

As discussed above, the incident electromagnetic radiation displaces the particle electron cloud and subsequently produces a restoring force which results in an oscillatory motion corresponding to the plasmon frequency.

Figure 1.9 Change in color of gold nanoparticles where refractive index of dielectric surrounding is changed from lower to higher index (Left to right). [17]

With the occurrence of this oscillation, the electrons induce a polarization in the opposite direction within the surrounding medium which reduces the restoring force and shifts the Plasmon resonance to a lower frequency. Therefore by controlling the optical properties of the surrounding environment the Plasmon resonance frequency can be tuned to a specific wavelength. [23,24,26,27]

Dependence of size of metal nanoparticles

While the plasmon resonance can be tuned by varying the dielectric constant of the surrounding medium the shape of the resonance spectra may be altered by the dimensions of the particle. For a particle smaller than the wavelength of the incident radiation, the electromagnetic field is uniformly distributed around the particle such that the conduction electrons move in phase producing only oscillations of the dipole kind. However if the size of the particles are increased, the field become nonuniform thereby broadening the dipole-type resonance and may excite high multipole resonances, which may lead to multiple peaks in the spectra. [24,26]

Shape dependence on metal nanoparticles

The plasmon resonance is also dependent on the shape of nanoparticles as seen in Figure 1.10. Here we see that a triangular shaped metal nanoparticles has a resonance at approximately 670 nm. As the shape of the metal nanoparticle is changed to a sphere, the resonance blue-shifts. The shape of the particle affects the local electric field and thereby alters the position of the plasmon resonance. [25,26]

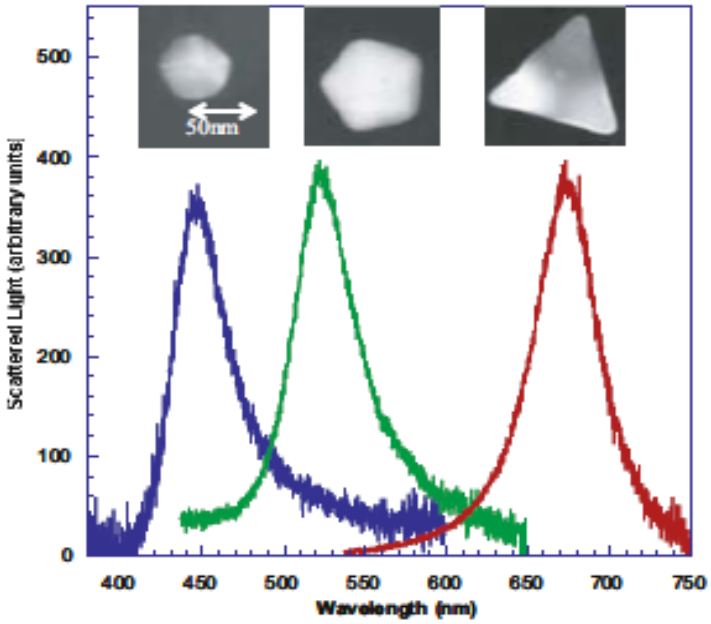

Figure 1.10 Spectral dependence of silver nanoparticles plasmon resonance on the shape nanoparticles. [25]

1.3 NONLINEAR OPTICAL PROPERTIES OF METAL

When the electric field of the incoming radiation is sufficiently intense, the relationship between the induced polarization in a medium and the field amplitude no longer follows a linear relationship. The polarization instead can be expanded into a power series of the real electric field **E** [28, 29]:

$$P = \varepsilon_0[\chi^{(1)}E + \chi^{(2)}E^2 + \chi^{(3)}E^3 + ... + \chi^{(p)}E^p + ...] \tag{1.12}$$

$\chi^{(1)} = \varepsilon - 1$ describes the linear susceptibility and $\chi^{(p)}$ is the p^{th}-order nonlinear susceptibility which is a tensor of rank $p+1$.

In a material exhibiting inversion symmetry (centrosymmetric media) the even-ordered susceptibilities from the electric dipole vanish and the first nonlinear susceptibilty term to

give a non-zero value is the third-order susceptibility. The metals discussed in this thesis exhibit such high third order nonlinear susceptibilties.

The component $P_i^{(3)}(\omega_m) = (i = x, y, z)$ of the third-order nonlinear polarization oscillating at frequency ω_m is expressed as a sum of terms proportional to the product of three Fourier components of the electric field [29]:

$$P_i^{(3)}(\omega_m) = \varepsilon_0 \sum_{npq} \sum_{jkl} \chi_{ijkl}^{(3)}(-\omega_m; \omega_n, \omega_p, \omega_q) E_j(\omega_n) E_k(\omega_p) E_l(\omega_q) \tag{1.13}$$

The frequencies and wavevectors fulfil phase matching conditions and the third order susceptibilty $\chi_{ijkl}^{(3)}$ is a fourth rank tensor. In an isotropic material there exist 21 non-zero elements, of which only three are independent. The most simple and general case consists of a linearly polarized incident plane wave. The third-order polarization vector is then parallel to the electric field and reduces to the sum of two propagating terms, one oscillating at the wave circular frequency, and the other at the circular frequency 3ω. The amplitudes of these two contributsion are :

$$\begin{aligned} \int P^{(3)}(\omega) &= 3\varepsilon_0 \chi^{(3)}(\omega) \left|E\right|^2 E(\omega) \\ \int P^{(3)}(\omega) &= 3\varepsilon_0 \chi^{(3)}(3\omega) E^3(\omega) \end{aligned} \tag{1.14}$$

Here the nonlinear susceptibilities (for the field oscillating along the x-axis) are described by:

$$\begin{aligned} \chi^{(3)}(\omega) &= \chi_{xxxx}^{(3)}(-\omega; \omega, \omega, -\omega) \\ \chi^{(3)}(3\omega) &= \chi_{xxxx}^{(3)}(-3\omega; \omega, \omega, \omega) \end{aligned} \tag{1.15}$$

The first contribution to the polarization induces a modification of the wave propagation in the material, for both its amplitude and phase, but without frequency change. This phenomenon is called the Optical Kerr Effect. The second contribution corresponds to the third harmonic generation (THG). The optical Kerr effect results in the dependence of the complex index of a material on the wave intensity *I* such that: [29, 30]

$$\begin{aligned} n &= n_0 + \gamma I \\ \alpha &= \alpha_0 + \beta I \end{aligned} \tag{1.16}$$

Where n_0 and α_0 are the linear refractive index and absorption coefficient, respectively, while γ is called the "nonlinear refraction coefficient" and β is called the "nonlinear absorption coefficient". By expressing the electric field in terms of electric displacement (neglecting terms proportional to I^2), one can obtain an equation relating the nonlinear coefficients and the third order susceptibility $\chi^{(3)} = \chi_r^{(3)} + i\chi_i^{(3)}$ as:

$$\begin{aligned} \chi_r^{(3)} &= \frac{4}{3}\varepsilon_0 c n_o^2 \gamma \\ \chi_i^{(3)} &= \frac{2}{3k}\varepsilon_0 c n_0^2 \beta \end{aligned}, \tag{1.17}$$

where the linear absorption is considered to be negligible in the wavelength range of interest.

1.4 CHAPTER SUMMARY

The chapter outlines the basic theoretical foundation behind the optical properties of QDs and metal nanoparticles and describes the various parameters that can be used to tune these properties. The colloidal QDs have several potential applications due to their tunable absorption and emission properties. In addition, their ability to be dissolved in different solvents provides an easy route to fabrication of photonic devices. Metal nanoparticles are seen to have striking linear and nonlinear properties. Furthermore, like QDs the optical properties can also be tuned by changing their size, shape and dielectric environment.

1.5 REFERENCES

1. A. Kongkanand, K. Tvrdy, K. Takechi, M. Kuno, and P.V. Kamat, "Quantum dot solar cells. Tuning Photoresponse through size and shape control of CdSe-TiO_2 Architecture," J. Am. Chem. Soc., **130**, 4007-4015 (2008)

2. J. Zhao, J.A. Bardecker, A.M. Munro, M.S. Liu, Y. Niu, I.K. Ding, J. Luo, B. Chen, and A.K.-Y. Jen, " Efficient CdSe/CdS Quantum Dot Light Emitting diodes using a thermal polmerzied hole transport layer," Nano. Lett., **6**, 463-467 (2006)

3. L.E. Brus, "Electron-electron and electron-hole interactions in small semiconductor crystallites: The size dependence of the lowest excited electronic state," J. Chem. Phys., **80**, 4403–4409 (1984)

4. L. Novotny, and B. Hecht, "Principles of Nano-Optics," Cambridge University Press, New York (2006)

5. P.N. Prasad, " Nanophotonics," John Wiley & Sons Inc., Hoboken, New Jersey (2004).

6. V.I. Klimov, " Nanocrystal Quantum Dots: From fundamental photophysics to multicolor lasing," Los Alamos Science., **28** (2003)

7. V.A. Singh, V. Ranjan, and M. Kapoor, "Semiconductor quantum dots: Theory and phenomenology," Bull. Mater. Sci., **3**, 563-569 (1999)

8. Y. Kayanuma, " Quantum-size effects of interacting electrons and holes in semiconductor microcrystals with spherical shape," Phys. Rev. B., **38**, 9797-9805 (1988)

9. A.P. Alivisatos, " Semiconductor Clusters, Nanocrystals, and Quantum dots," Science, New Series., **271**, 5251, 933-937 (1996)

10. Y. Masumoto, and T. Takagahara, "Semiconductor quantum dots: physics, spectroscopy and applications," Springer (2002).

11. D. Gammom, E.S. Snow, B.V. Shanabrook, D. S. Katzer, and D. Park, " Fine Structure Splitting in the Optical Spectra of Single GaAs Dots," Phys. Rev. Lett., **76**, 16 (1996)

12. G. Schmid, " Nanoparticles: from Theory to Application," Wiley-VCH (2010)

13. E.M. Boatman, G.C. Lisensky, and K.J. Nordell, " A Safer, Easier, Faster Synthesis of CdSe Quantum dot Nanocrystals," Jour. Chem. Education., **82**, 169 (2005)

14. H.Q. Nguyen, "Synthesis and Optical properties of CdSe nanocrystals and CdSe/ZnS core shell nanostructures in non-coordinating solvents," Adv. Nat. Sci.: Nanotechnol., **1**, 025004 (2010)

15. D.N Sathyanarayana, " Electronic Absorption Spectroscopy and Related Techniques," Universities Press (India) Limited (2001)

16. J. D. Jackson, "Classical Electrodynamics," Wiley, New York (1999)

17. A. Moores, and F. Goettmann, "The Plasmon band in noble metal nanopartles: an introduction to theory and applications," New J. Chem., **30**, 1121-1132 (2006)

18. G. Mie, "Contributions to the optics of turbid media, particularly colloidal metal suspensions," Ann. Phys. Leipzig., **25**, 377 (1908)

19. D.D. Evanoff, Jr. and G. Chumanov, "Synthesis and Optical Properties of Silver nanoparticles and Arrays," Chem.Phys., ,**6,**1221-1231 (2005)

20. L.M. Liz-Marzan, " Nanometals, formation and color," Materials Today (2004)

21. M. Faraday, Philos. Trans. R. Soc. London., **147**, 145 (1857)

22. S.A. Maier, " Plasmonics: Fundamentals and Applications," Springer Verlag (2007)

23. U. Kreibig, and M. Vollmer, " Optical Properties of Metal Clusters," Springer Series in Material Sciences., **25** (1995)

24. N. Halas, " The optical properties of Nanoshells," Optics and Photonics News., 26-30 (2002)

25. J.J. Mock, M. Barbic, D.R. Smith, D.A. Schultz, and S. Schultz, " Shape effects in Plasmon resonance of individual colloidal silver nanoparticles," J. Chem. Phys., **116**, 6755-6759 (2002)

26. K. L. Kelly, E. Coronado, L.L Zhao, and G. C. Schatz, " The optical properties of metal nanoparticles : The influence of Size, Shape and Dielectric Environment," J. Phys. Chem. B.,**107**, 668-677 (2003)

27. J.J. Mock, D.R. Smith, and S. Schultz, " Local Refractive Index Dependence of Plasmon Resonance Spectra from Individual Nanoparticles," Nanoletters, **3**, 485-491 (2003)

28. J.R. Sambles, G.W. Bradbery, and F. Yang, "Optical excitation of surface plasmons: an introduction," Contemporary Physics, **32**, 173-183 (1991)

29. R.W. Boyd, " Nonlinear Optics," Academic Press, Second Edition (2003)

30. M.G. Papadopoulos, A. J. Sadlej, and J. Leszczynski, "Non-linear optical properties of matter," Springer (2006)

Chapter 2. EXPERIMENTAL DETAILS

In order to study the optical processes in structures discussed in this thesis, various fabrication methods and optical characterization techniques have been employed. In section 2.1 below an outline of the optical techniques used to investigate composites and structures pertaining to this thesis, is presented. In section 2.2 the basic fabrication procedures conducted during this work are also described in detail.

2.1 Optical Techniques

2.1.1 Steady-State and Time Resolved Photoluminescence Spectroscopy

This thesis involves work done using both steady-state and time resolved photoluminescence (PL). Figures for both of these setups related to work done in this thesis are shown in Figure 2.1.

In PL spectroscopy, light is incident on a sample at a wavelength which induces absorption. Upon absorption of the incident energy, the electrons move into excited states. The electron may return to the ground state radiatively. Radiative relaxation is called photoluminescence (shown in Figure 2.2). When energy is emitted in the form of a photon whose wavelength is different from the incident radiation, it is [generally] equal to the difference of the energies in the ground and excited state. When a photon emitted has the same wavelength as the incident light, resonance fluorescence takes place. Relaxation can also happen non-radiatively; most often it occurs through vibrations (or collisions) that lead to thermal processes.

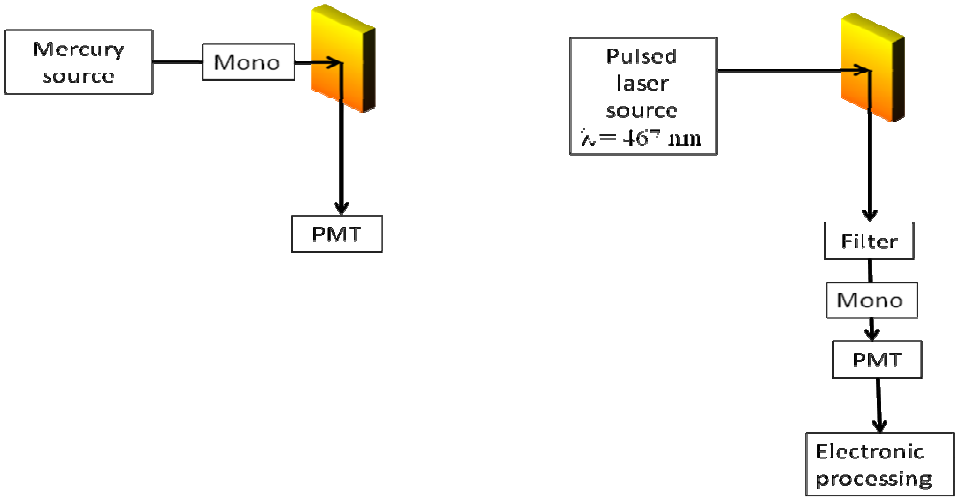

Figure 2.1 Schematics of setup for (a) Steady State PL measurements and (b) Time Resolved PL measurements

Under pulsed excitation, PL intensity transients yield information about lifetimes of excited states. For time-resolved photoluminescence (TRPL) measurements a time-correlated single photon counting (TCSPC) system is implemented. This technique offers a wide dynamic range and allows a very sensitive temporal range recording with picoseconds resolution with extremely high precision. TRPL captures the change in intensity of PL emission over time, after the laser pulse is incident on the sample. TCSPC relies on the principle that the probability distribution for the emission of a single fluorescence photon is equivalent to the actual intensity versus time distribution for all photons emitted. TRPL is to capture the change in intensity over time of the PL emission after a pulse from the laser is incident on the sample. The principle is to detect the arrival of single photons and build a probability density function of photon arrival times between the consecutive excitation pulses. A monochromator is set up filter and control intensity of incoming photons. [1-4]

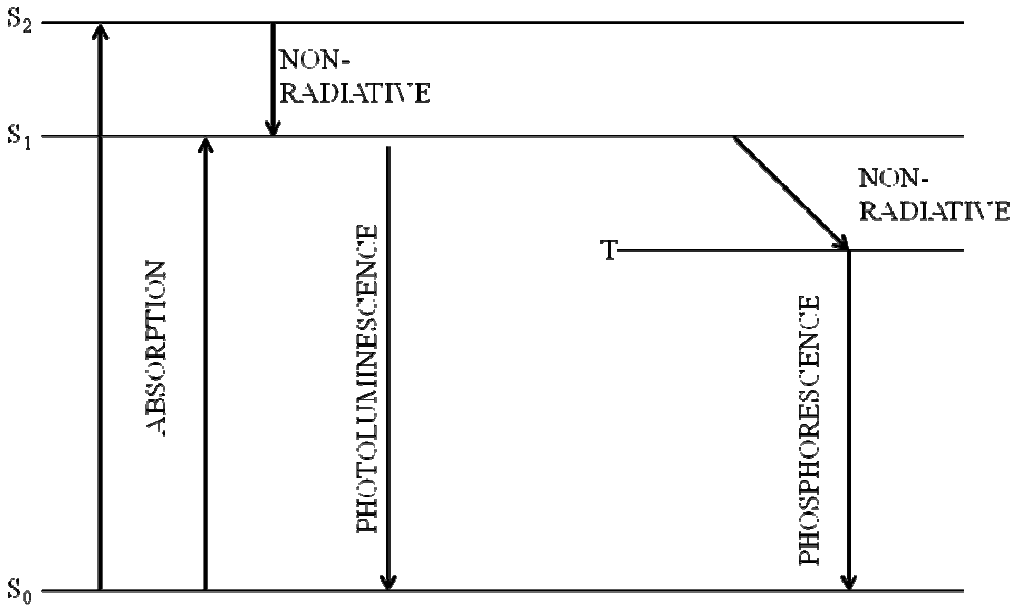

Figure 2.2 Schematic of optical process between ground state and excited states

The time required for a molecule to change singlet states is in the order of picoseconds. The triplet state emits its energy and comes back to the ground state in times spanning from milliseconds to seconds.

PL is a non-destructive technique which provides very sensitive measurements that can be used to characterize various material parameters. In addition, PL allows band gap determination for semiconductor compounds. In addition, PL allows the determination of material quality and is able to identify impurity levels and detect defects which may be the cause of radiative transitions in semiconductors.

2.1.2 ABSORPTION

All absorption measurements are extracted using a CARY 5000 UV-VIS-NIR double-beam spectrophotometer (schematic diagram is shown in Figure. 2.3) which records absorbance of the samples. The CARY 5000 provides a wide wavelength range (175 – 3300nm), has excellent limiting resolution (<0.045 in the UV) and allows for sensitive detection. The absorption of light by materials studied follows the Lambert-Beer's law which states that the amount of light absorbed is directly proportional to the number of molecules of the absorbing species:

$$A = -\log T = \eta l C \tag{2.1}$$

Here A is the absorbance (intensity of light absorbed by molecules at a certain frequency), T is the transmittance, η is the molar absorptivity, l is the light pathlength, and C is the concentration of the absorbing material.

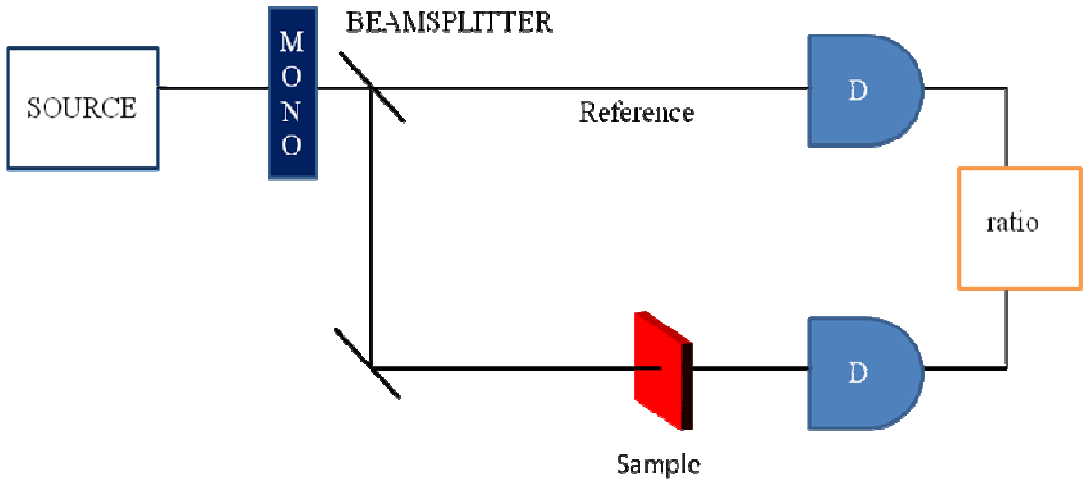

Figure 2.3 Schematic of double beam absorption measurement setup (assay.nih.gov)

The transmittance is defined as the fraction of incident light (at a specific frequency) which passes through the material:

$$T = \frac{I}{I_0}, \tag{2.2}$$

where I_0 the incident light is measured at the Reference arm in Figure 2.3 and I is the light transmitted through the sample. [3, 5]

2.1.3 ELLIPSOMETRY

Ellipsometry is an extremely versatile and powerful optical technique used to investigate the dielectric properties of thin films. Figure 2.4 shows a schematic of an ellipsometer. In an ellipsometry experiment, electromagnetic radiation is emitted by a light source and is linearly polarized before striking the sample. Ellipsometry measures the change in polarization state of light reflected from (or transmitted through) the surface of the sample.

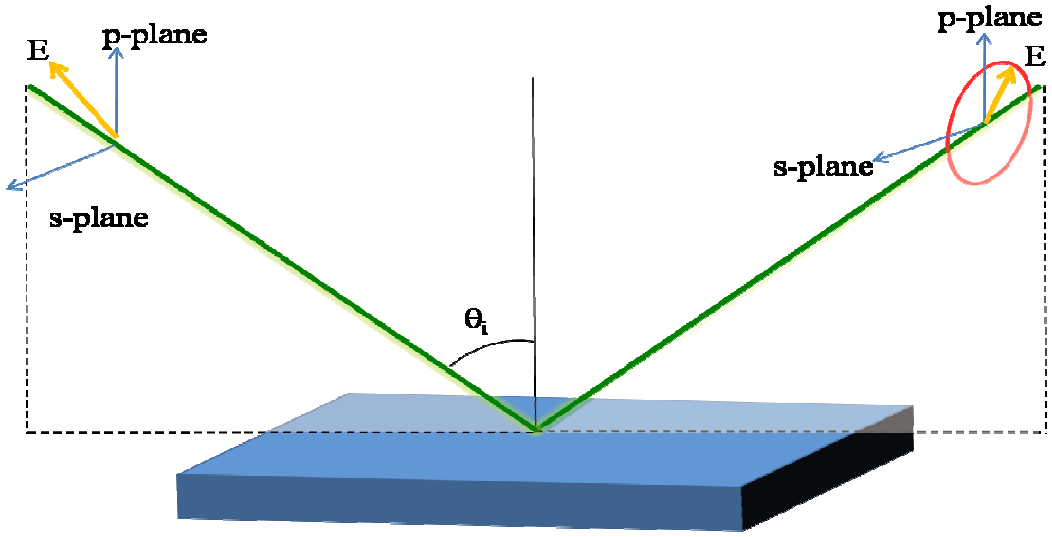

Figure 2.4 Schematic showing geometry of an ellipsometric experiment indicating p- and s-direction [6].

Fundamentally, ellipsometry only refers to the measurement of the polarization state of the light beam. However, ellipsometry measurements are usually performed in order to describe an "optical system" that modifies the polarization state of a beam of light.

An ellipsometer measures a complex reflectance ratio ρ which is related to the ratio of Fresnel reflection coefficients, $\tilde{R}_p$ and $\tilde{R}_s$ for p and s-polarized light respectively. The measured values are expressed as Ψ and Δ which are expressed in terms of Fresnel coefficients as:

$$\rho = \frac{\tilde{R}_p}{\tilde{R}_s} = \tan(\Psi) e^{i\Delta} \tag{2.3}$$

Ellipsometry can be used to characterize both thin films and bulk materials. It is sensitive to film thickness and optical constants (in the UV, visible, and IR wavelength ranges). All measurements in this thesis were carried out using a J.A. Woolam variable angle spectroscopic ellipsometer. The spectral acquisition range and angle of incidence may be optimized for determination of various sample parameters. [6]

2.1.4 Z-SCAN MEASUREMENTS

Materials possessing high third order nonlinear susceptibilities have garnered much interest due to their potential applications in optical switching and surface enhanced Raman spectroscopy. The optical Kerr effect which describes the change in refractive index induced by intense illumination is one of the most common nonlinear phenomena measured. The z-scan technique which was first studied in 1989 by M. Sheik-Bahae et al [7, 8] is a sensitive single beam technique to measure the real and imaginary part of the

nonlinear refractive index. In a z-scan measurement the laser beam with a Gaussian profile is focused by a lens. In this thesis we assume a TEM_{00} Gaussian beam of beam waist radius w_0 travelling in the + z direction and therefore we can write E as [7]:

$$E(z,r,t) = E_0(t)\frac{w_0}{w(z)}\cdot\exp(-\frac{r^2}{w^2(z)}-\frac{ikr^2}{2R(z)})e^{-i\varphi(z,t)} \quad (2.4)$$

,

where $w^2(z) = w_o^2(1+z^2/z_0^2)$ is the beam waist radius at the position z, $R(z) = z(1+z^2/z_0^2)$ is the radius of curvature of the wavefront z, and $z_0 = kw_0^2/2$ is the diffraction length of the beam. $E_0(t)$ describes the electric field at focus and the term $e^{-i\varphi(z,t)}$ consists of the radially uniform phase variations. This creates an intensity variation in the laser beam along the direction of light propagation (z-direction) where the highest intensity occurs within the depth of field (where the beam is most focused; it is taken as position $z = 0$). A schematic diagram of a typical z-scan setup is shown in Figure 2.5.

As the sample moves through the beam focus (at $z = 0$), changes in transmittance due to Nonlinear Absorption (NLA) and Nonlinear Refraction (NLR) are measured by an open aperture and a closed aperture, respectively.

For nonlinear absorption measurements, we focus on non-resonant two photon absorption which is defined as the excitation of a molecule induced by the simultaneous absorption of two photons of the same energy. Two photon absorption is a nonlinear third-order process where the energy absorbed is quadratically proportional to the intensity of incident light. The nonlinear absorption coefficient β is related to the imaginary part of

the cubic third-order nonlinear susceptibility defined in section 1.3. Similarly the nonlinear refractive index coefficient is proportional to the real part of the cubic third order susceptibility. Here the nonlinear refractive index is altered in the presence of a strong optical electric field (section 1.3).

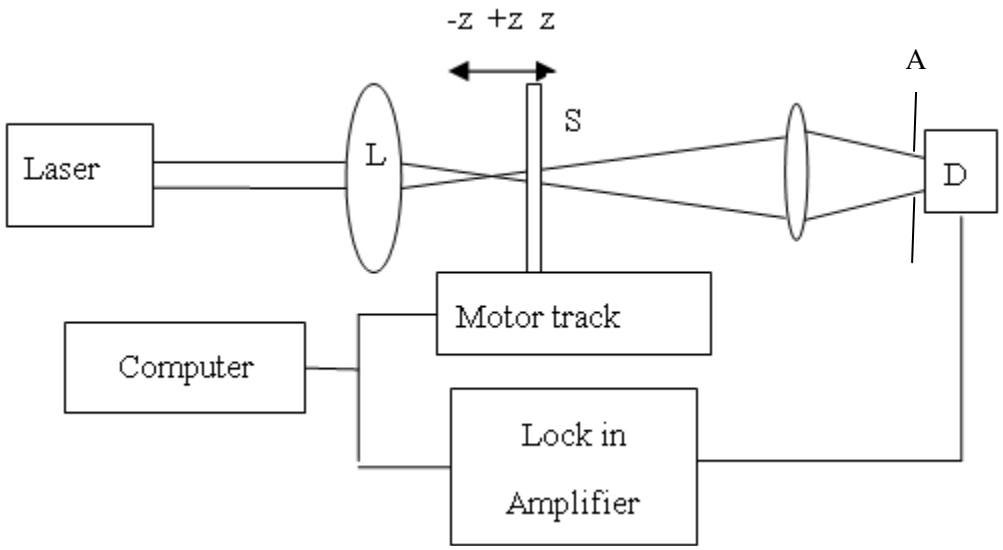

Figure 2.5 Schematic of a single beam z-san experiment setup; configuration consisting of lens(L), sample (S), Aperture (A) and Detector D are shown [10]

In an open aperture z-scan measurement, the aperture is set to allow most of the light to pass through. This corresponds to collecting all the transmitted light and in this configuration the sample is insensitive to any nonlinear beam distortion due to nonlinear refraction. As the beam passes through the sample, it is focused directly onto a detector. The transmittance either increases or decreases (depending on the sample nonlinearity) and the detector receives light either more or less than the incident radiation. This type of scan yields either a peak or dip in the transmittance curve as a function of sample position. Using open aperture z-scan we can measure the nonlinear absorption parameters

for the sample. The nonlinear absorption coefficient β can be obtained from the open aperture normalized transmittance data by fitting it to formula given by [8]:

$$T_{OP}(z) = 1 - \frac{q_0}{2\sqrt{2}(1+x^2)}$$
$$q_0 = \beta I L_{eff}\,;\, L_{eff} = \frac{1-e^{-\alpha L}}{\alpha}\,;\, x = \frac{z}{z_0}\, and\ z_0 = \frac{\pi w_0^2}{\lambda} \tag{2.5}$$

In the closed aperture technique, an aperture is centered on the z-axis to block (approximately 30%) of the beam. Depending on the nonlinearity, the sample in position behaves like a lens and induces either a self-focusing (or self de-focusing) nonlinearity. A positive (negative) change in refractive index induces a self-focusing (self de-focusing) nonlinearity which results in a pre-focal valley (peak) followed by a post-focal peak (valley).

To measure nonlinear refraction in the presence of nonlinear absorption is complicated. The nonlinear transmission obtained from closed aperture contains both refractive and absorptive terms. The change in transmittance between peak and valley in a closed z-scan measurement is defined as [9]:

$$T = 1 + \frac{4x}{(x^2+9)(x^2+1)}\Delta\Phi - \frac{2((x^2+3)}{(x^2+9)(x^2+1)}\Delta\Psi$$
$$where:$$
$$\Delta\Phi = k\gamma I_0 L_{eff}\,,\, \Delta\Psi = \frac{\beta I_0 L_{eff}}{2} \text{ and } x = \frac{z}{z_0} \tag{2.6}$$

Here $\Delta\Phi$ and $\Delta\Psi$ are the nonlinear phase shifts due to NLR and NLA, respectively. Therefore, in the presence of nonlinear absorption, which involves the samples used in

this thesis, the nonlinear transmission is not dominated by a nonlinear refractive effect and therefore cannot be fit to a purely refractive function. Within approximations [6, 7] a simple division of the closed and open aperture curves allows one to approximate what would be obtained with a closed aperture z-scan having the same Δn. Therefore, one can calculate the nonlinear refraction coefficients using the peak-valley value of the divided (closed/open aperture) curves using: [10-11]

$$\begin{aligned} &\Delta T_{p-v} = T_p - T_v \cong 0.406(1-S)^{0.27} \left|\Delta\Phi_0\right| \\ &\textit{where} \\ &\Delta\Phi_0 = \frac{2\pi}{\lambda} n_2 I_0 L_{eff} \end{aligned} \tag{2.7}$$

where α is the linear absorption coefficient, $L_{eff} = \dfrac{1-e^{-\alpha L}}{\alpha}$, and S is the transmittance of the aperture in the absence of the sample. $\Delta\Phi_0$ is the on-axis nonlinear phase shift and I_0 is the irradiance of sample at focus.

2.1.5 FOURIER TRANSFORM INFRARED SPECTROSCOPY(FTIR)

The Fourier Transform Infrared Spectrometer consists of an IR source and detector and a Michelson interferometer. A Michelson interferometer component includes a fixed and moving mirror and a beam splitter as shown in Figure 2.6. The beam impinges on the beamsplitter and is split into two beams which reflect off the fixed and moving mirror and recombine at the beam splitter. The recombined beam then passes through the sample chamber and onto an IR detector. If the moving mirror is at the same optical distance from the beamsplitter as the fixed mirror, positive (maximum) interference takes place in the recombined beam, because the path difference for all wavelengths is zero. However,

if the moving mirror is displaced a distance '*d*,' the two beams cover difference distances and the intensity of the interference in the beam changes. The phase difference depends on the displacement '*d*' of the moving mirror in the form:

$$\phi = \frac{2\pi d}{\lambda} = 2\pi\sigma d$$
$$\sigma = \frac{1}{\lambda} \tag{2.8}$$

Because the path that one beam travels is a fixed length and the other is constantly changing, the signal which exits the interferometer is the result of the two beams. This signal is called an interferogram which has the unique property that every data point (a function of the moving mirror position) which makes up the signal has information about every infrared frequency which comes from the source. The signal is therefore dependent on the displacement of the moving mirror.

When conducting measurements in the FTIR a background spectrum (reference) is taken to account for any reflection of the mirrors or beam splitters in addition to atmospheric absorption. The transmission (or absorption) of the sample in question is then divided by this background spectrum.

When conducting measurements with the FTIR a background spectrum (reference) is taken to account for any reflection of the mirrors or beam splitters in addition to atmospheric absorption. The transmission (or absorption) of the sample in question is then divided by this background spectrum.[12]

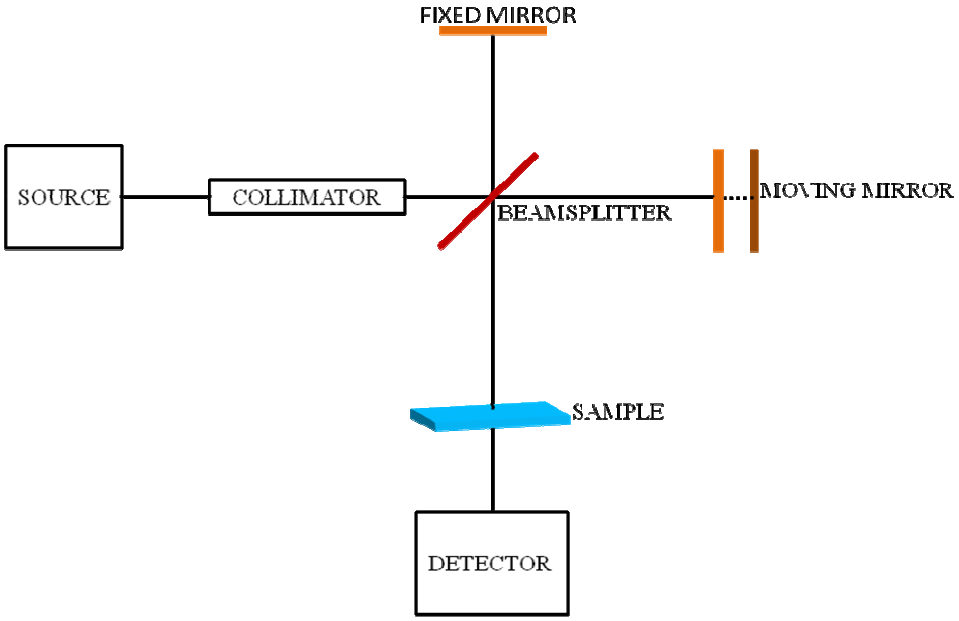

Figure 2.6 Schematic diagram showing Fourier Transform Infrared Spectrometer consisitng of a Michelson Interferometer [12]

2.2 FABRICATION TECHNIQUES

2.2.1 SOFT LITHOGRAPHY

Soft lithography entails the use of an elastomeric stamp using which, structures can be replicated from a master pattern. A PDMS (polydimethylsiloxane) stamp is formed using a 1:10 ratio of resin to base. The mixture is placed in a degasser to remove air bubbles and poured onto a master pattern and heated at 140°C for 20 minutes. The mixture settles itself around the master pattern, and the high temperature solidifies it. The stamp is peeled off and placed on a substrate which has been dropcoated with a photosensitive substance. The liquid flows due to capillary action into the recesses between the stamp and substrate. The sample is UV-exposed and the stamp is peeled off to reveal the

replicated structures composed of the desired photoresist. An overview of the procedure is shown in Figure 2.7. Soft lithography is a low cost method for rapid protoyping. A PDMS stamp can be molded into any shape; therefore the surface need not be flat. In addition, it is an efficient way of reproducing any pattern many times over using the same stamp. However, due to the complex nature of present day circuits which require multiple layers of structures, soft-lithography falls short. Soft lithography methods utilizing PDMS based methods are currently useful to produce features 500 nm or larger; however extension of these methods can also produce sub-100 nm structures. Although structures as small as 500 nm can be fabricated via soft lithography there is a high chance of error due to the low degree of control [13, 14]. The structures produced by this method depend on the quality of the master pattern which over time can deteriorate therefore transferring any imperfections onto the sample.

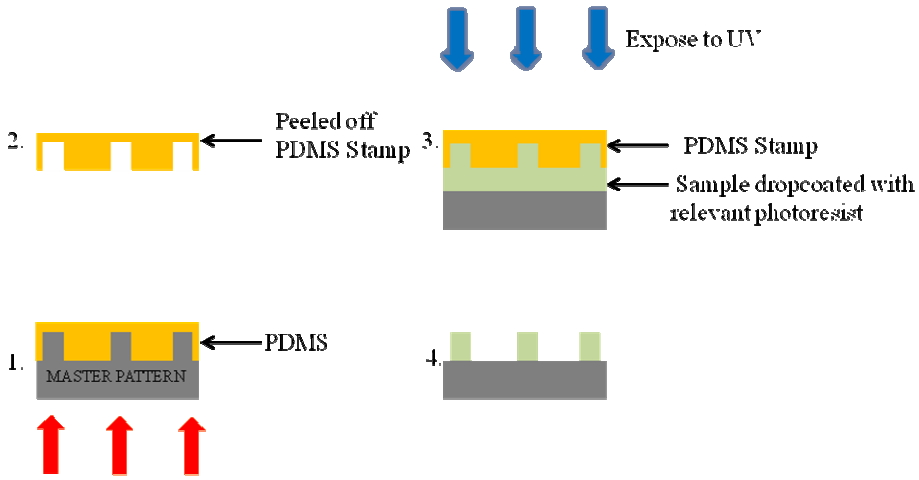

Figure 2.7 Overview of soft lithographic process

2.2.2 SPIN COATING

Spin coating is a straightforward fabrication procedure useful for the creation of thin and uniform films. A substrate is vacuum mounted on a spinner. The material is then drop cast onto the substrate. The thickness of the layer depends on factors such as spinning speed and time along with the viscosity and rate of evaporation of the solution. By adjusting these parameters, the solution can be spread over almost the entire substrate to create a uniform film. With other conditions fixed the thickness is usually inversely proportional to the spin speed.

After the solution is spincoated the sample is put on a hot plate to evaporate the remaining solvent. The temperature of this bake depends on the solvent used.

Spin coating also allows the fabrication of a multilayer structure. A new layer can be spun on top of an existing layer. However a requirement for such a process is that the solvent for the new layer should be chosen such that it does not dissolve the existing layer. With this requirement fulfilled, spin coating is an efficient and effective procedure to produce multilayered structures. Although due to this strict requirement spin coating has not been extensively used to produce one-dimensional photonic structures. Also as each spin coating run is not identical, thickness may vary in tens of nanometers from layer to layer. [15, 16]

The use of spin coating for fabrication of photonic devices is not very common. Spin coating is usually used as an intermediate step in photolithography or for film thickness characterization.

2.2.3 *PHOTOLITHOGRAPHY*

Photolithography is a fabrication technique that requires a patterned photomask with the desired structure. The steps of the procedures are shown in Figure 2.8. The process requires a photoresist to be spincoated on a substrate. The sample is then prebaked to remove any remaining solvent. It is then vacuum mounted on a mask aligner stage. The photomask is placed on top and a contact vacuum is initiated to ensure the proper size of structures.

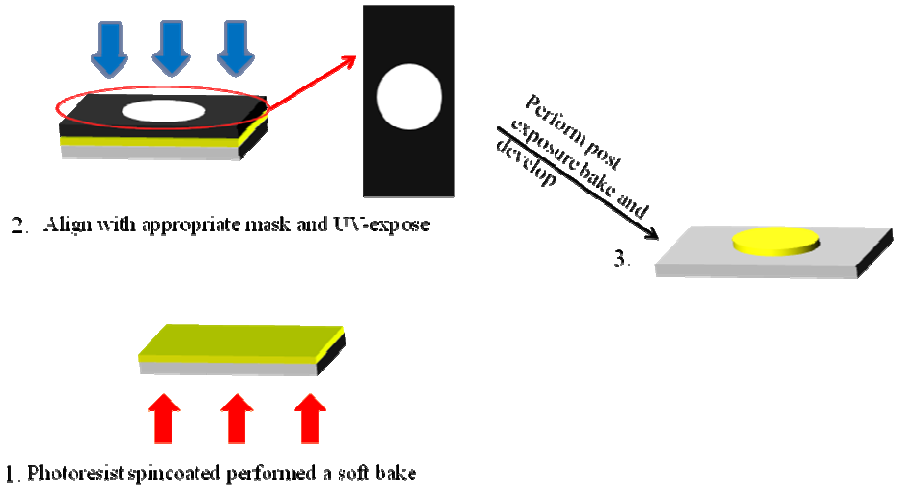

Figure 2.8 Schematic overview of photolithographic process

The sample is then exposed to UV light for the desired exposure time. A post bake is sometimes necessary depending on the photoresist used to strengthen cross linkage bonds. Finally the sample is developed in the appropriate photoresist compatible developer.

Photolithography is an ideal method to fabricate circuits on a mass scale and the fabrication of a multilayer structure can be produced with little difficulty. However its

resolution is limited and there is a higher chance of contamination if the process is not carried out in a clean room environment. [15-16]

2.2.4 ELECTRON BEAM LITHOGRAPHY

Electron beam (e-beam) lithography consists of focused electron beam impinging onto a substrate which is covered with an e-beam suitable photoresist. The work done in this thesis focuses on electron beam lithography based on a scanning electron microscope which consists of a direct write system. The desired pattern is prepared in a CAD-based software.

The sample consisting of the appropriate photoresist is placed in a chamber and the beam is generated via a four stage e-beam focusing process before hitting the surface. Figure 2.9 shows a schematic of the electron beam writing and SEM system used on samples used in this thesis. A deflection system controls the beam with high precision over a set writing surface.

The electron beam is accelerated through a voltage set electrode and is turned on and off by a blanking mechanism as the stage moves. The features obtained depend on several factors, such as type and thickness of resist, beam current, resist thickness in addition to development processes.

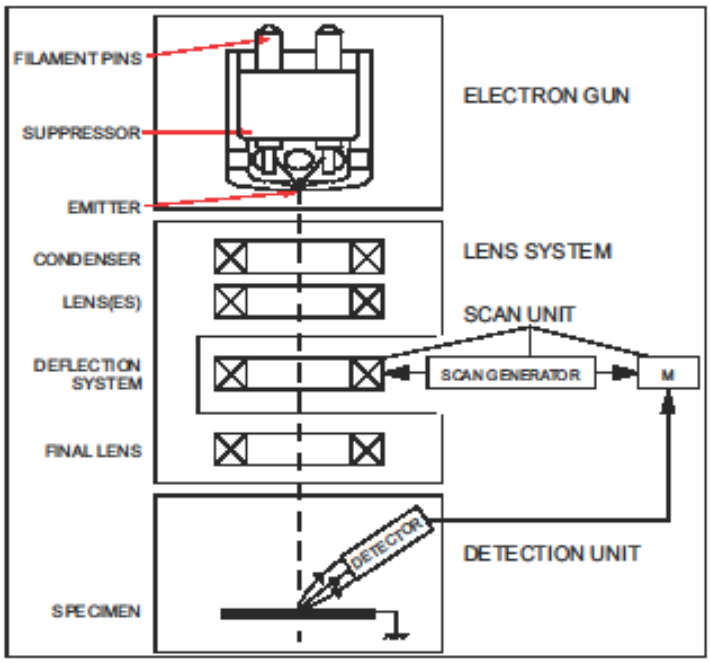

Figure 2.9 Schematic showing the Quanta F200 SEM system used in this thesis [18]

Although electron beam writing provides high sensitivity, resolution and precision, its limitations are finite. Extremely small features lead to a proximity effect whereby structures are enlarged. In addition, attention must be paid to substrate that may lead to excessive charging on the surface.

The equipment itself is expensive and depending on dosage area required, the creation of devices is time consuming. In addition, it is very sensitive to the factors discussed above and optimization of required parameters is tedious. However it offers extremely high resolution and can produce structures up to tens of nanometers, which are hard to reach using conventional lithographic techniques. [15-18]

2.3 REFERENCES

1. FluoroHub User Guide, Single photon counting controller, Courtesy of HORIBAJOBIN YVON
2. David L. Andrews, and Andrey A. Demidov, " An Introduction to Laser Spectroscopy," Second Edition, Springer (2002)
3. Ralf Menzel, " Photonics: Linear and Nonlinear Interactions of Laser Light and Matter," Springer- Verlag (2001)
4. L. Novotny, and B. Hecht, " Principles of Nano-Optics," Cambridge University Press (2006)
5. D.N. Sathyanarayana, " Electronic Absorption Spectroscopy and Related Techniques," Universities Press (India) Limited (2001)
6. Guide to using WVASE 32, Courtesy of J.A. Woollam Co., Inc
7. M. Sheikh-Bahae, A.A. Said, and E.W. Van Stryland, " High Sensitivity, Single Beam n_2 Measurements," Opt. Lett., **14**, 955-957 (1989)
8. M. Sheik-Bahae, A.A. Said, T.H. Wei, D.J. Hagan, and E.W. Van Stryland, " Sensitive Measurements of Optical Nonlinearities Using a Single Beam," Journal of Quantum Electronics., **26**, 760-769 (1990)
9. H. Shen, B.L. Cheng, G.W. Lu, D.Y. Guan, Z.H. Chen, and G.Z. Yang, " Picosecond nonlinear optical responses of Au/PVP composite films," J. Phys. D: Appl. Phys., **39**, 233-236 (2006)
10. E. Shahriari, and W.M Mat Yunus, " Single Beam Z-Scan Measurements of Nonlinear Refraction and Nonlinear Absorption coefficients in Silver Nano-Fluid," Amer. J. of Engineering and Applied Sciences., **3**, 98-101 (2010)
11. C. Fuentes-Hernandez, L.A. Padilha, D. Owens, S.Y. Tseng, S. Webster, J.Y. Cho, D. Hagan, E.W. van Stryland, S.R. Marder, and B. Kippelen, " Linear and nonlinear optical properties of highly transmissive one-dimensional metal-organic photonic band gap structures," Proc. Of SPIE., **7049**, 704900 (2008)
12. P.R. Griffiths, and J.A. De Haseth, " Fourier Transform Infrared Spectrometry," Wiley-Interscience (2007)

13. A. Kumer, and G.M. Whiteside, " Features of gold having micrometer to centimeter dimensions can be formed through a combination of stamping with elastomeric stamp and an alkanethio 'ink' followed by chemical etching," Appl. Phys. Lett., **63**, 2002-4 (1993).

14. Y.N. Xia, and G.M. Whitesides, Soft lithography, Angewandte Chemie-International Edition, **37**, 551-575 (1998).

15. S. Franssila, " Introduction to Microfabrication," John Wiley and Son (2010)

16. S.Nonogaki, T. Ueno and T. Ito, "Microlithography fundamentals in semiconductor devices and fabrication," CRC Press (1998)

17. H.J. Levinson, " Principles of Lithography," SPIE Press (2005)

18. User Guide of Quanta 200F (2007)

Chapter 3. OPTICAL STUDIES OF PHOTONIC STRUCTURES EMBEDDED WITH COLLOIDAL QUANTUM DOT COMPOSITES

Colloidal QD composites are attractive candidates for realizing photonic devices (as discussed in chapter 1) due to their excellent spectral properties. Colloidal quantum dots unlike their self assembled counterparts have allowed structures to be realized via spin coating. Their ability to be dissolved in any liquid has increased their capability to be integrated in a vast range of applications. Besides allowing structures to be fabricated via spin coating, colloidal quantum dots allow for excellent compatibility with a silicon platform, and their tunable absorption and emissive properties have allowed for a wider spectral coverage ranging from UV to infrared. This has led to their usage in a wide range of applications in bio-sensing, telecommunication, solar cells [1], color displays [2] and quantum cryptography.

Although colloidal quantum dots have become very attractive nanoscale fluorescent emitters, they have failed to achieve a widespread application in the fabrication of photonic devices, due the difficulty in pattering them. This issue arises due to the problems in incorporating quantum dots in various host matrices without significantly altering the optical properties.

This chapter therefore focuses on investigations in meeting this challenge and studying the effect of various stages of fabrication on the optical properties of quantum dots. These composites are made by introducing quantum dots in various host matrices-specifically SU8, Poly methyl methacrylate (PMMA), UV curable resin (proprietary from evident technologies) and toluene. The optical studies carried out on these quantum dot composites lead us to understand and identify the various mechanisms that govern their behavior within these matrices. To fully realize the mechanisms by which the systems

are influencing the optical properties of the colloidal QDs, steady state and time resolved luminescence measurements are carried out. It is shown that optical properties of quantum dots vary significantly with different host matrices as well as different deposition techniques. It is shown that SU8 inhibits the intensity of the quantum dots as well as induces a high rate of quenching. To further analyze the optical properties of colloidal quantum dots, absorption and Fourier Transform Infrared Spectroscopy (FTIR) measurements are carried out.

Finally a microdisk embedded with quantum dots is fabricated via soft lithography and luminescence from it is observed.

3.1 Optical Studes of Colloidal Quantum Dot Composites

3.1.1 Steady-State and Time-Resolved Photoluminescence

Steady state photoluminescence measurements are taken using the setup described in Chapter 2. Cadmium Selenide (CdSe) colloidal quantum dots with an emission peak at 621 nm (in toluene and hexane) are embedded in three host matrices-SU8 a negative polymer based photoresist, PMMA a polymer based positive photoresist and UV curable resin. The quantum dots within toluene are also studied as a reference. 0.3 ml of the colloidal quantum dots are mixed with 6 ml of the matrices. Figure 3.1 shows results of steady state measurements of the CdSe quantum dots (in toluene) in different hosts. In Figure 3.1 it can be seen that although the emission peak of the quantum dot does not shift significantly and the FWHM remains approximately 40 nm for all spectra, there is a significant decrease in PL intensity of the colloidal quantum dots in all host matrices, and especially SU8.

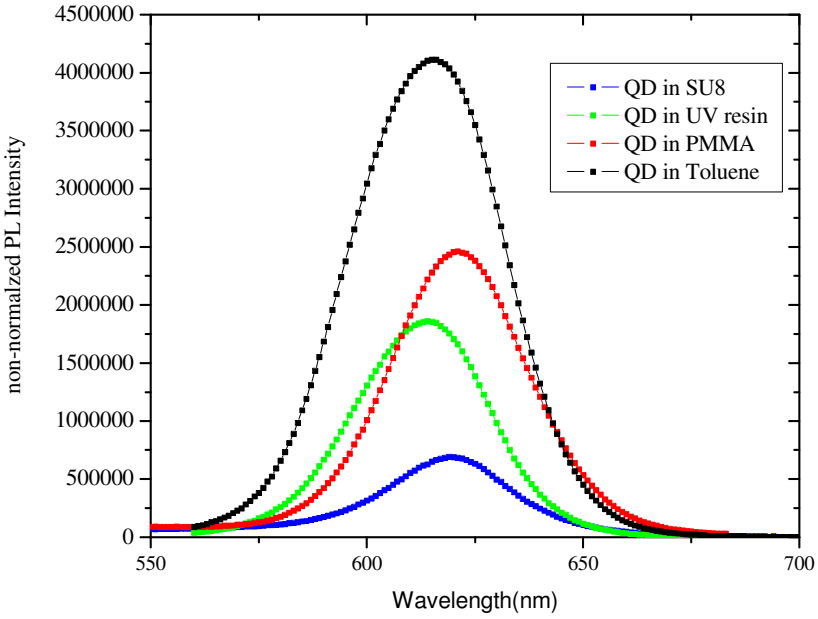

Figure 3.1 Steady State Photoluminescence measurements showing the highest intensity drop with SU8

Time-resolved photoluminescence are also performed using the setup described in chapter 2. Fluorescence decay is a consequence of the limited lifetime of excited states that can occur through both radiative and non-radiative channels. The decay time corresponds to the lifetime of the emitting state and therefore can be determined by the time resolved observations of the excited state. We perform time resolved luminescence experiments, shown in Figure 3.2 on the four colloidal quantum dot composites prepared as described above. It is observed that the fastest decay happens in the SU8 matrix. This faster decay accompanied by a significantly lower PL intensity is attributed to a non-radiative decay of the dots.

Since the final photonic devices will be prepared using lithographic methods the effect of the photoresists on the colloidal quantum dots are further investigated. Two solutions of

the colloidal quantum dots in SU8 and PMMA are prepared which contained a quantum dot fractional volume of 0.03

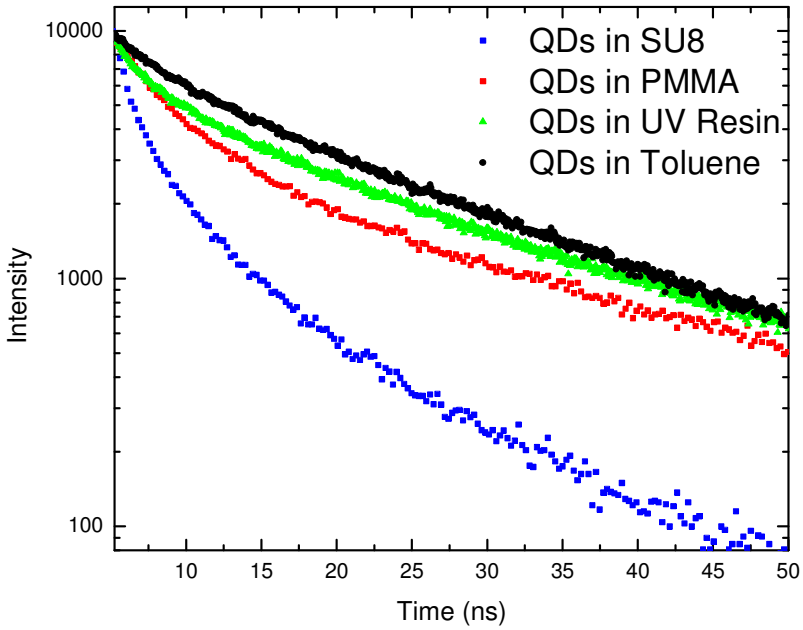

Figure 3.2 Time Resolved PL measurements showing fastest decay in the polymer based photoresists with highest decay occuring in SU8

Three samples of each solution are prepared with different casting techniques. The first set of samples, are spincoated at 30 seconds for 3000 rpm. For SU8 the samples first undergo a soft bake at 90°C for two minutes and are exposed to UV light for 22 seconds. A post exposure bake is then carried out at 90°C for two minutes and the sample is finally developed. The same procedures are carried out for a dropcoated sample of colloidal quantum dots in SU8. The spin coated and dropcoated samples are studied via TRPL experiments and compared to similar casting procedures for quantum dots embedded in PMMA. Figures 3.3 (a) and (b) show the PL lifetime of the quantum dots in SU8 and for PMMA for different deposition techniques. It can be seen that the PL lifetime for the dropcoated sample shows the fastest decay. The exact reasons for this effect are still

being investigated. One of the hypotheses is that dropcoating results in a close packing of the quantum dots which may lead to efficient interdot [resonant?] energy transfer.

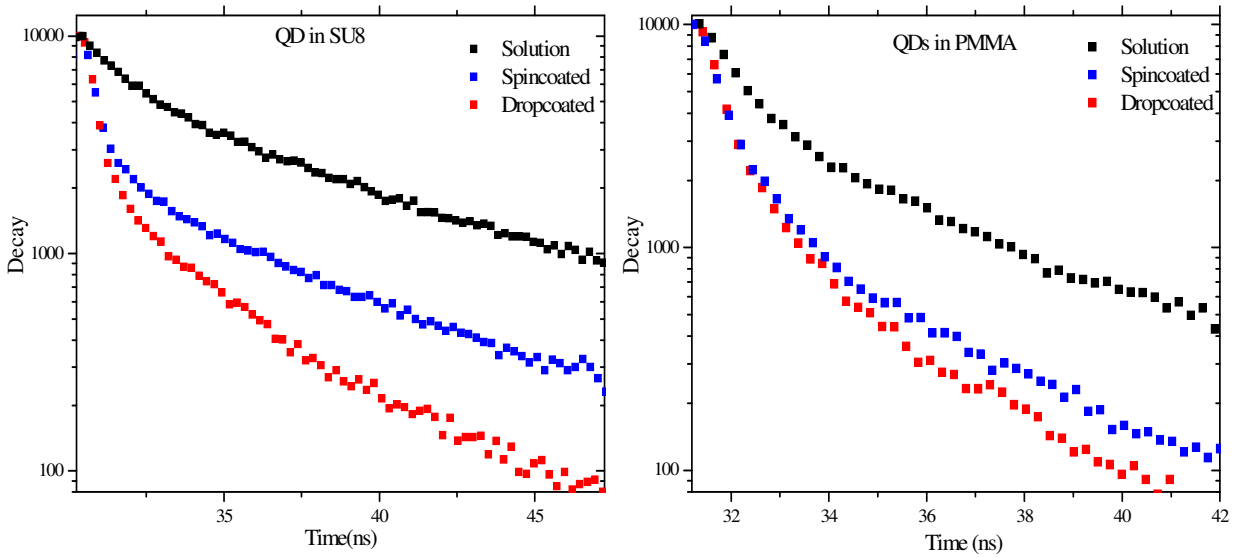

Figure 3.3 Time Resolved PL dependence on deposition techniques of QDs in (a) SU8 and (b) PMMA. Pl lifetime of dropcoated samples of QDs in both host matrices show fastest decay

3.1.2 Absorption and Infrared Spectroscopy

The study of intraband transitions in QDs allows us to identify the intersubbands in QDs. Transitions within these levels can be used to produce mid-infrared detectors and emitters. Many biological as well as gas molecules possess strong optical resonances therefore the fabrication of devices that function in the IR enable biological as well as trace gas sensing. Soluble infrared fluorophores which are efficient may find applications for imaging and labeling in the IR spectral range where biological based materials are transparent. Although much work has been done to study the size-dependence on the

optical properties of quantum dots, there has been an increasing interest in studying intraband processes that take place in quantum dots. [3-5]

This section focuses on identifying and studying the optical transitions of colloidal quantum dots in two solvents- toluene and hexane. The aim is to further understand carrier dynamics that take place within the dots. The band diagram of CdSe QDs is shown in Figure 3.4. The three arrows indicate transitions due to absorption which correspond to excitonic peaks in the absorption spectra.

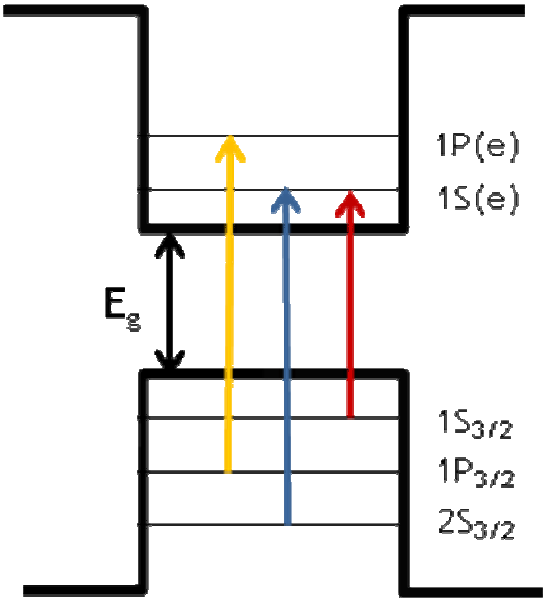

Figure 3.4 Band diagram of CdSe quantum dots

The linear absorption measurements are carried out using a CARY 5000 UV-VIS-NIR spectrophotometer whose setup is discussed in chapter 2. Figure 3.5 shows the absorption spectrum of colloidal quantum dots in toluene. The first three excitonic peaks occur at 2.06 eV, 2.49 eV and 2.92 eV respectively. Through simple calculations one obtains the 1S(e)-1P(e) transition to be 0.43 eV.

Infrared spectroscopy is carried out using a Fourier Transform Infrared Spectrometer which utilizes a KBr beamsplitter (details discussed in chapter 2). This transition is identified in the IR spectra shown in Figure 3.5 (b). The plots in Figure 3.5 (b) also show the results of optical pumping our sample with an Argon laser, leading to a greater number of carriers in 1 S(e) and therefore a larger dip in the transmission spectra. However by observing the spectrum shown in Figure 3.5 (b) there does not seem to be significant difference in transmission spectra in the presence and absence of pumping.

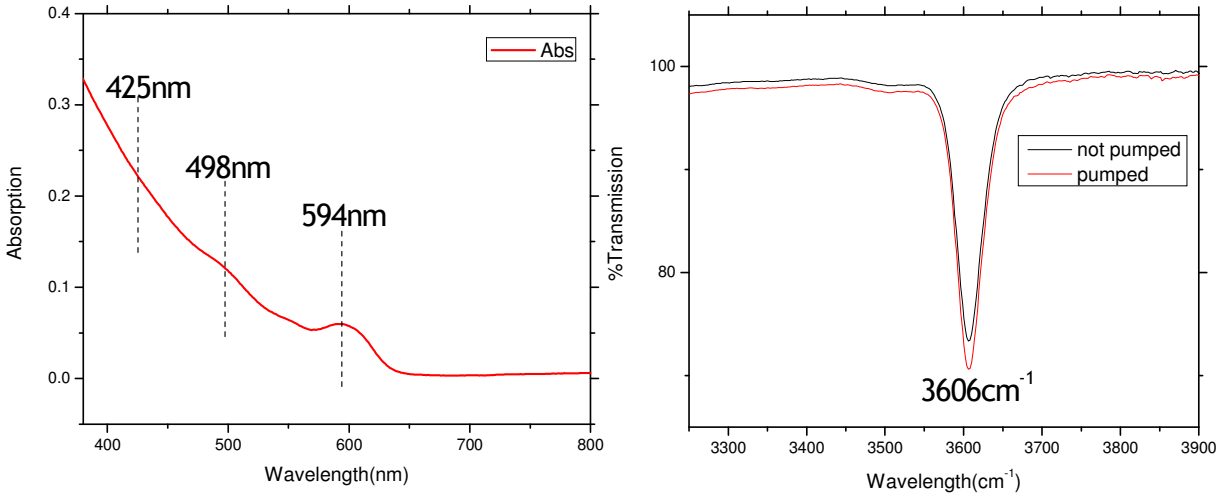

Figure 3.5 Absorption spectra indicating first, second and third excitonic peaks of CdSE quantum dots in toluene (b) FTIR spectra of CdSe quantum dots in toluene showing absorption transition at 0.43eV. Optical pumping indicates greater density of excited states

Similar experiments are carried out with CdSe quantum dots in toluene as shown in Figure 3.6 (a) and (b). The first three excitonic peaks are at 2.08 eV, 2.24 eV and 2.44 eV. The 1S(e)-1P(e) transition is calculated to be 0.2eV which is comparable to the IR spectra which shows an energy of 0.195 eV in Figure 3.6 (b). These studies are therefore done to analyze the band structure in the colloidal quantum dots of interest.

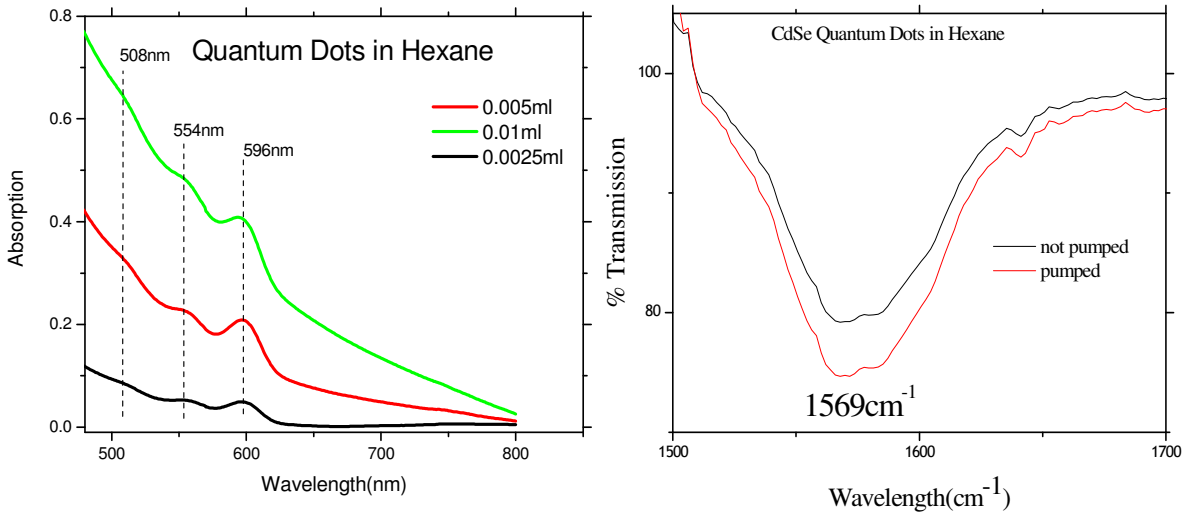

Figure 3.6 Absorption spectrum indicating first, second, third exciton peaks of colloidal quantum dots in hexane. (b) FTIR spectra indicating the 1S(e)-1P(e) intraband transition

3.2 RING/DISK RESONATORS EMBEDDED WITH COLLOIDAL QUANTUM DOTS

This section reports on work done to incorporate colloidal quantum dots composites into a microdisk/ ring resonators. Light circulation within a small dielectric volume enables optical storage power at specific frequencies and is important in a wide range of fields such as biosensing, cavity quantum electrodynamics and nonlinear optics. These resonators have high Q values and small mode volumes which allow the possibility of maximum light-matter interaction. However, optical trajectories occurring at their surface are dependent strongly upon surface roughness and therefore require a highly controlled fabrication environment. Therefore introducing an active medium within these resonators efficiently remains challenging. This is due to difficulty in optimizing fabrication procedures that are compatible with the quantum dots. Embedding photon emitters in such resonators alters their emission properties due to the ability of these structures to confine and enhance the electromagnetic fields. Recently much work has been done to

embed colloidal QDs in microspheres, two and three-dimensional photonic crystals and microdisk structures [6-12]. However most of these demonstrations were done using expensive fabrication techniques. In addition, colloidal quantum dots must be introduced so as to avoid clustering and aggregation. Using the optical studies carried out on the colloidal quantum dot composites (shown in the previous sections) this section focuses on the efficient introduction of colloidal quantum dots into a microdisk pillar using soft lithography - a simple fabrication technique (section 2.2.1). Work done in optimizing fabrication processes is also reported. The first part of this section introduces the theoretical framework that governs behavior of light within these structures. Optimization of fabrication methods discussed in chapter 2 is introduced. Finally, luminescence observed from a colloidal quantum dot embedded microdisk is shown..

3.2.1 THEORY OF RING/DISK RESONATORS

This section outlines theory of a single ring resonator with radius r, coupled to a waveguide. The theory for this basic configuration can be extended to explain light coupling in other geometries (as discussed later in this thesis). As seen in Figure 3.7 the model consists of a ring resonator and a waveguide. The coupling is assumed to be lossless and any other kinds of losses which occur along propagation of light in the ring resonator filter are incorporated in the attenuation constant.

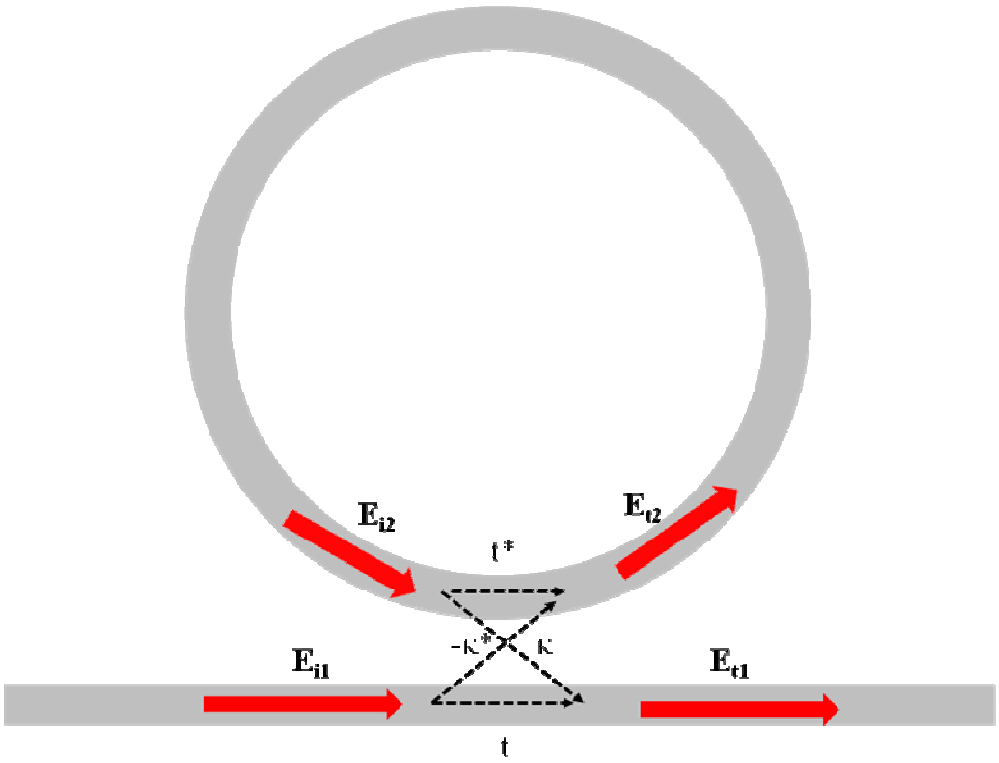

Figure 3.7 Schematic of a ring resonator coupled to a waveguide configuration [13, 14]

The interaction between the resonator and waveguide can be expressed via a matrix relation [13-15]:

$$\begin{pmatrix} E_{t1} \\ E_{t2} \end{pmatrix} = \begin{pmatrix} t & \kappa \\ -\kappa^* & t^* \end{pmatrix} \begin{pmatrix} E_{i1} \\ E_{i2} \end{pmatrix} \tag{3.1}$$

Here the external complex mode amplitudes E_{i1}, E_{t1} and the internal ring amplitudes E_{i2}, E_{t2} are normalized (therefore the square of these will be the respective travelling wave powers). The coupling parameters t and κ depend on the specific coupling used. The coupling is assumed lossless and therefore:

$$\left|\kappa^2\right| + \left|t^2\right| = 1 \tag{3.2}$$

The incident power E_{i1} is taken to be 1 and therefore one circulation around the ring can be taken to be:

$$E_{i2} = \alpha \cdot e^{i\theta} E_{t2} \tag{3.3}$$

here α and θ are real numbers corresponding to the loss (or gain) and the phase shift per round-trip within the ring. ($\theta = \frac{\omega L}{c}$ where $L = 2\pi r$, $c = \frac{c_0}{n_{eff}}$ and $\omega = kc_0$, where k is the vacuum wavenumber). The propagation constant can now be introduced:

$$\beta = k \cdot n_{eff} = \frac{2\pi \cdot n_{eff}}{\lambda} \tag{3.4}$$

Using equations 3.1 and 3.3 we obtain

$$\begin{aligned} E_{t1} &= \frac{-\alpha + t \cdot e^{-i\theta}}{-\alpha t^* + e^{-i\theta}} \\ E_{i2} &= \frac{-\alpha \kappa^*}{-\alpha t^* + e^{-i\theta}} \\ E_{t2} &= \frac{-\kappa^*}{1 - \alpha t^* e^{-i\theta}} \end{aligned} \tag{3.5}$$

Here the transmission power in the output waveguide can be calculated as:

$$P_{t1} = \left|E_{t1}\right|^2 = \frac{\alpha^2 + \left|t\right|^2 - 2\alpha\left|t\right|\cos(\theta + \phi_t)}{1 + \alpha^2\left|t\right|^2 - 2\alpha\left|t\right|\cos(\theta + \phi_t)} \tag{3.6}$$

$t = \left|t\right| e^{i\phi_t}$ where ϕ_t is the phase shift introduced due to coupling

The power P_{i2} circulating in the ring is given then by:

$$P_{i2} = \left|E_{i2}\right|^2 = \frac{\alpha^2(1-\left|t\right|^2)}{1+\alpha^2\left|t\right|^2 - 2\alpha\left|t\right|\cos(\theta+\phi_t)} \tag{3.7}$$

Upon resonance where $(\theta+\phi_t) = 2\pi m$ [m is an integer]

$$\begin{aligned} \mathrm{P}_{t1} &= \left|E_{t1}\right|^2 = \frac{(\alpha-\left|t\right|)^2}{(1-\alpha\left|t\right|)^2} \, and \\ P_{i2} &= \left|E_{i2}\right|^2 = \frac{\alpha^2(1-\left|t\right|)^2}{(1-\alpha\left|t\right|)^2} \end{aligned} \tag{3.8}$$

Therefore the transmission factor is represented by $\frac{P_{t1}}{P_{i1}}$ where we assumed the incident power to be unity. This gives [13]:

$$\frac{P_{t1}}{P_{i1}} = \frac{(\alpha-\left|t\right|)^2}{(1-\alpha\left|t\right|)^2}, \tag{3.9}$$

where it is seen that at, $\alpha = t$ (critical coupling) the transmitted power goes to zero. Small changes in α for a given t (and vice versa) can control the transmitted power between zero and unity. Therefore if the cavity field is out of phase with the input signal destructive interference occurs. However, if the cavity is in phase with light coupling through the waveguide, constructive interference takes place.

This leads to field build up in the cavity shown in Figure 3.8 and therefore to well defined resonances (whispering gallery modes) shown in Figure 3.9. Whispering gallery modes are formed due to the total internal reflection of light at the dielectric interface along the

circumference of these cavities. As seen in Figure 3.9 coupling of about 90% is achieved due to loss being accounted for at the coupler. Due to the well defined nature of these resonances one can assume that the maximum interaction between waveguide and resonator takes place at the area of closest approach. With a perfectly circular resonator the light has limited opportunity to couple with the resonator however with racetrack resonators the coupling length can be controlled more and allows a longer period of light interaction.

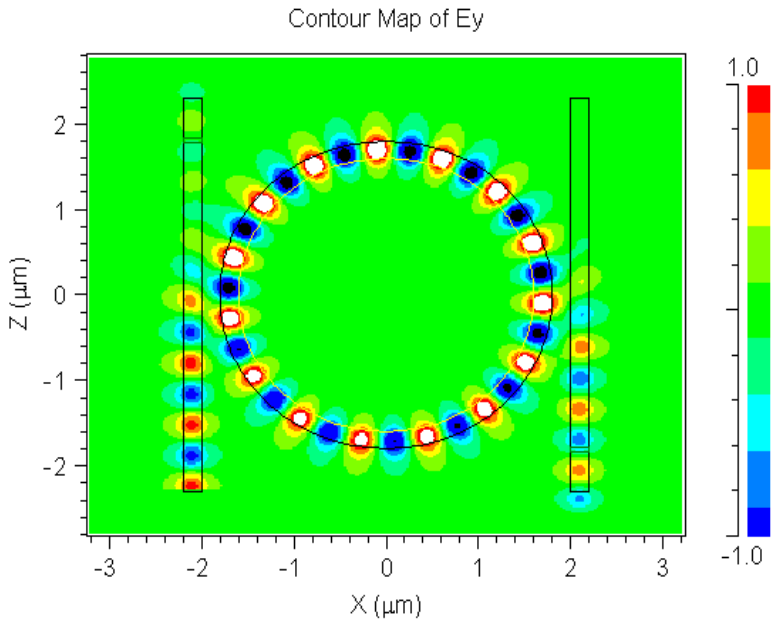

Figure 3.8 Simulation showing coupling between ring resonator and waveguides indicating enhancement in cavity field.

Therefore these equations described above can be extended to simulate other ring resonator configurations. For the basic configuration the coupling gap size is deduced by the coupling length available.

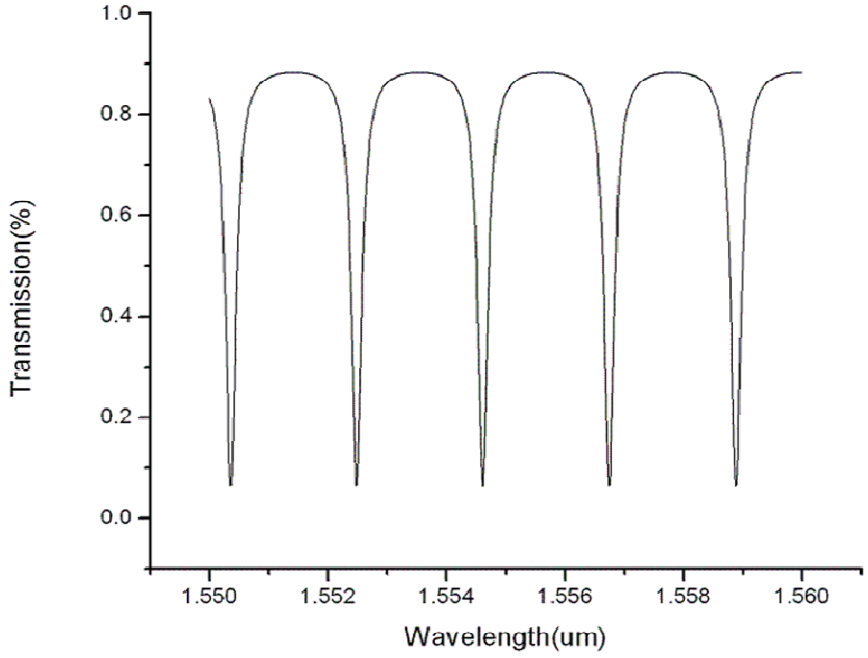

Figure 3.9 Transmission spectrum of ring resonator (coupled with a waveguide) showing whispering galley resonances

Therefore in this thesis we describe fabrication procedures using a laterally and vertically coupled racetrack-shaped ring resonator as shown in Figures 3.10 (a) and (b). In such geometry the length available for coupling is greater and therefore the coupling gap can be enlarged allowing for greater fabrication tolerance [15]. However, with such resonators it is important to consider the variation in phase difference occurring in the coupling regions between t and κ. The phase difference is dependent on the coupling length and significantly affects the output (in magnitude and resonance conditions)

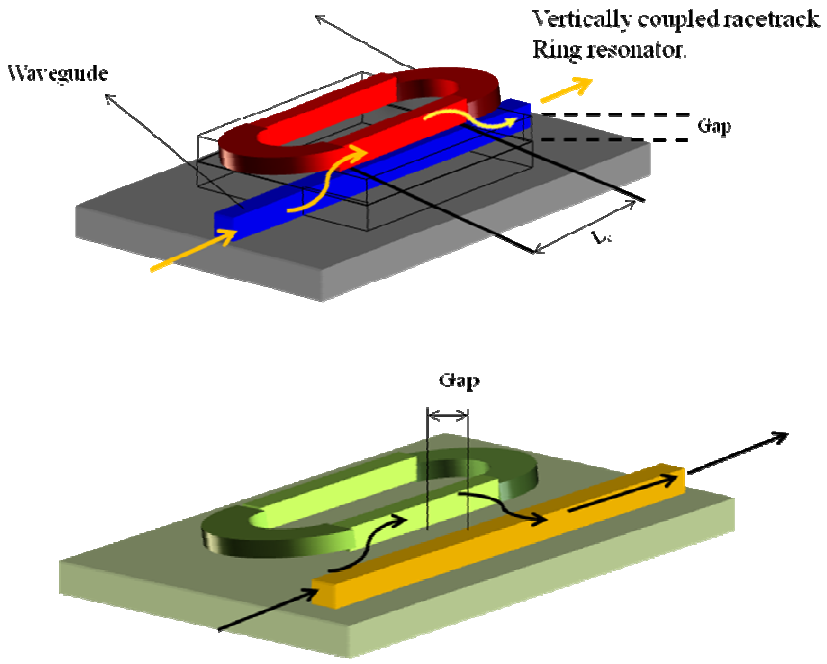

Figure 3.10 Two waveguide-resonator geometries are shown (a) verical coupling where resonator and waveguide are on two different layers and (b) Lateral coupling where resonator and waveguide are in the same plane and are evanescnently coupled

All optical resonators can be described by certain parameters which determine their figures of merit (FOM). For such resonators as described above the free spectral range (FSR) which is the distance between resonance peaks and is defined as [16]:

$$FSR = \Delta\lambda = \frac{\lambda^2}{n_g L}$$
$$n_g = n_{eff} - \lambda \frac{\partial n_{eff}}{\partial \lambda} \text{ is the group refractive index} \qquad (3.10)$$

Another important parameter describing such resonators is called the finesse 'F' of the resonator and is it the ratio of mode separation to the spectral width ($F = \frac{FSR}{FWHM} = \frac{\Delta\lambda}{2\delta\lambda}$)

The quality factor Q is also used to define such resonators and is the stored energy per cycle divided by the power lost in coupling. Since these resonators can possess high field intensities than the input waveguides they tend to possess very high quality factors. [17]

As shown above, these resonators act as optical filters and can confine light at specific frequencies for an extended period of time. Integrating these structures with an active medium such as quantum dots, can lead to exploration and investigations of light matter interactions (in small volumes) and nonlinear optical phenomena. In addition, by introducing a gain element in such resonators one can manipulate the loss [6-12, 18-22]. In the following sections we present preliminary work done in producing microdisks, vertically and laterally coupled resonators and integrating them with colloidal quantum dots.

3.2.2 OPTICAL STUDIES ON RESONATORS EMBEDDED WITH QUANTUM DOTS

Three lithographic techniques (discussed in chapter 2) were used to fabricate the following resonators. For all these techniques SU8 (MicroChem Corp) was used as a photoresist. SU-8 is a high contrast, negative, epoxy-based, UV-radiation sensitive photoresist which offers suitable chemical, mechanical and optical properties. It has a refractive index of approximately 1.6 and therefore offers a sufficient refractive index contrast for light confinement in these structures. [22]

Before fabrication of the vertically coupled ring resonator, simulations are performed to optimize the geometric parameters of the resonator. Figure 3.11 (a) show the field confinement between the waveguide and the active racetrack ring resonator. For the vertically coupled resonator the coupling length measured 250microns, the radius of

curvature was set to 100 microns and the coupling gap measured 2-3microns to achieve > 95% coupling. A cross section schematic is shown in Figure 3.11 (b). To optimize coupling a cladding layer is utilized (shown in yellow). OG-125 is a polymer photoresist with an index of 1.45 which is spin coated onto the substrate and cured with UV light.

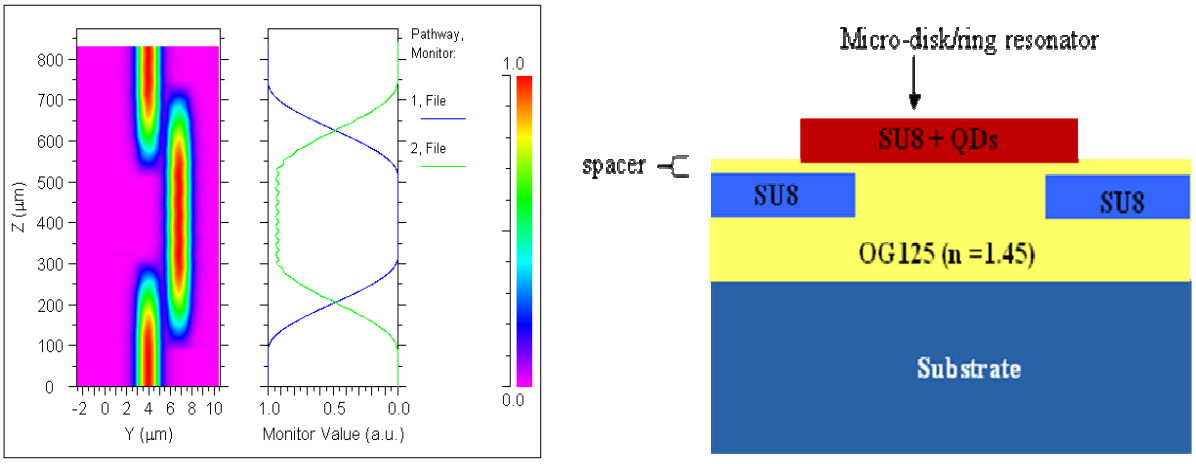

Figure 3.11 (a) Simulations showing coupling between passive waveguide and active resonator (b) cross section of the device indicating layer compositons

The spacing separating the waveguides is optimized at 250 microns to ensure that light couples only to the resonator and not from one waveguide to the other. Finally a thin layer of OG-125 is spun between the passive waveguide and active resonator. This low index cladding layer ensures efficient coupling from SU-8 with an index of 1.6 into the active resonator with a higher index.

A solution of 2 ml of SU-8 with 0.2 ml of CdSe/ZnS quantum dots in hexane is prepared. Colloidal quantum dots in hexane are utilized as toluene is incompatible with SU-8. To prepare the solution the colloidal dots are added very slowly with constant stirring to avoid clustering of the quantum dots. In addition, to create a monodisperse layer, the

quantum dot composite solution is filtered to avoid aggregation of the dots. A silicon substrate is cleaned thoroughly using acetone, methanol and isopropanol and dried using nitrogen. A layer of OG-125 is spin coated for 5 seconds at 500 rpm and then ramped to 3000 rpm for 30 seconds. It is then heated for 4 minutes at 80 $^{\circ}$C and exposed for 10 minutes. Finally, a post bake for 3 minutes at 95 $^{\circ}$C is performed. SU-8 2005 is then spin coated for 30 seconds at 3000 rpm followed by a soft bake for one minute done at 90 $^{\circ}$C. A photomask with a waveguide pattern is used to expose the SU8 coated sample for 11.1 seconds. The next layer of OG-125 was prepared by mixing it in 1:2 ratio with SU-8 developer (in order to get a thinner layer) and was spin coated and processed above. Now the SU-8 (with quantum dots) is spin coated for 30 seconds at 3500 rpm followed by a soft bake at 95 $^{\circ}$C and exposed for 20 seconds with the photomask. At this step, alignment marks on the mask were used to align the bottom and top layers. Once exposed, a post exposure bake was done for 2 minutes at 95 $^{\circ}$C and developed. Two vertically coupled resonators were fabricated. Figure 3.12 (a) shows the resonator without colloidal quantum dots and (b) with colloidal quantum dots [23].

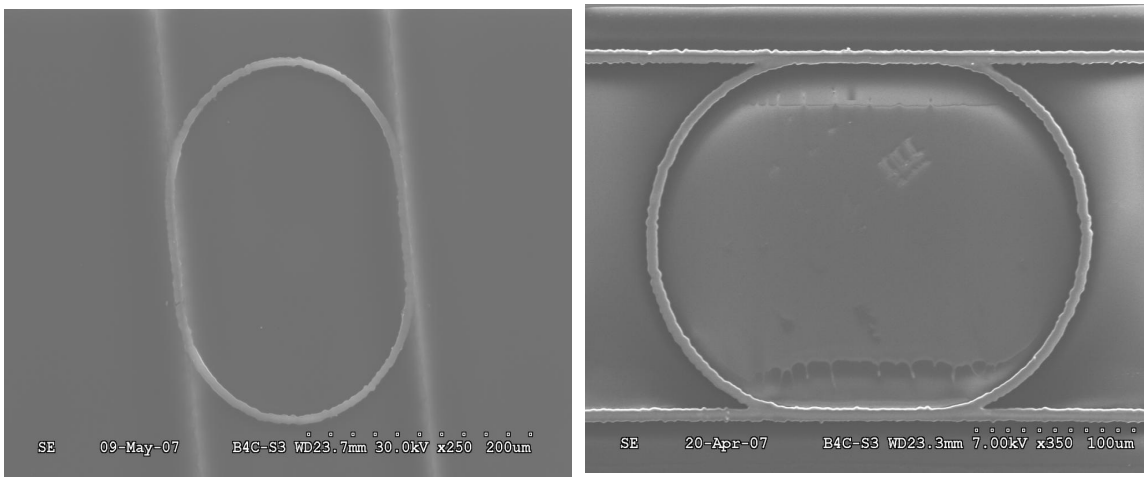

Figure 3.12 SEM image of a vertically coupled ring resonator fabricated via photolithography in the absence (a) and presence (b) of quantum dots

Figure 3.12 (a) indicates an alignment error while Figure 3.12 (b) shows that the OG 125 did not provide a stable cladding layer causing the resonator to sink to the waveguide level. These issues are currently being addressed using a SiO_2 cladding layer instead of OG125.

The technique of soft lithography was carried out using a master mask on silicon consisting of a 20 micron microdisk pillars. A solution consisting of 0.05 ml of colloidal CdSe/ZnS quantum dots in hexane with 10 ml of SU-8 was prepared. To avoid clustering the solution was further filtered. A PDMS (polydimethylsiloxane) stamp is prepared using a 1:10 ratio of resin to base and poured over the master mask. The liquid flows into the recesses between the stamp and substrate. The sample is then heated at 140 $^{\circ}$C for 20 minutes, due to which the stamp solidifies and can be peeled effortlessly. Finally a cleaned silicon wafer is dropcoated with the SU-8 with QD solution and the PDMS stamp is carefully placed on it.

This sample is then exposed to UV light for 10.5 seconds and a post exposure bake for 10 minutes at 95 $^{\circ}$C is carried out. The stamp is then peeled off carefully. Figures 3.13 (a) and (b) show SEM images of the microdisk pillar, where the edges are reasonably good.

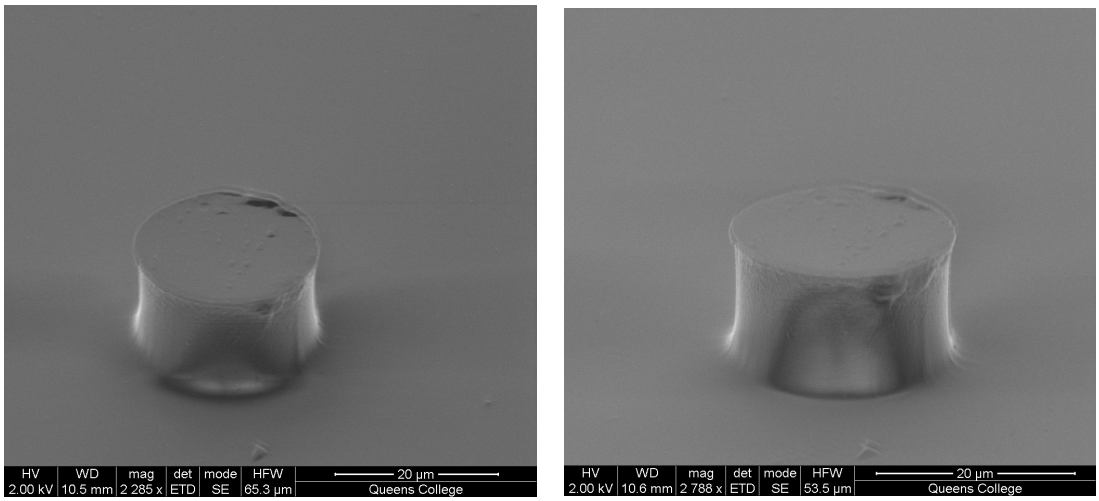

Figure 3.13 SEM images of a microdisk pillar embedded with colloidal quantum dots fabricated via soft lithography

To optically characterize the quantum dot embedded disk, the system is optically pumped using an Argon laser and light is collected via a tapered fiber. Figure 3.14 (a) shows the optical pumping process. Here we show the microdisk being pumped and a tapered fiber positioned to collect the light. However due to the weak signal from the disk, we were unable to observe a resonance spectra. In Figure 3.14 (b), however we do observe luminescence from the dots embedded in the disk.

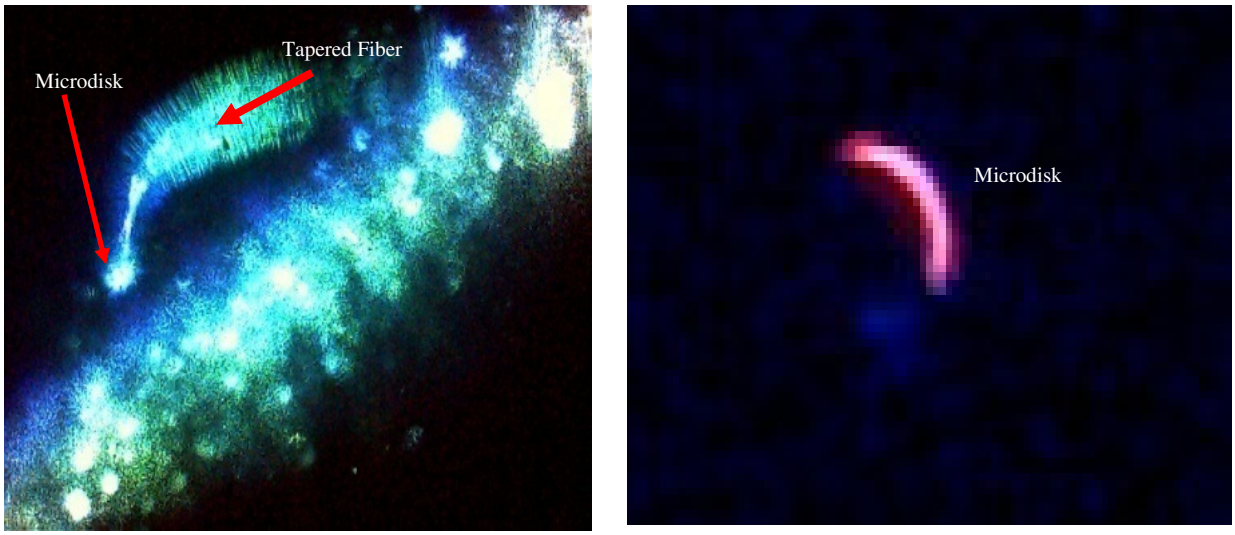

Figure 3.14 (a) shows microdisk being optically pumped resulting in (b) luminescence from the disk

3.3 CHAPTER SUMMARY

The optical properties of the colloidal quantum dots is studied and their interband transitions are identified. The investigation of the optical properties of the host matrices embedded with quantum dots provided the platform for preliminary fabrication techniques, which are compatible to the photonic structures in question. In addition, understanding the properties of these colloidal quantum dots in various host matrices, will allow for their efficient integration into the photonic devices. Furthermore preliminary lithographic fabrication techniques well suited to the colloidal quantum dots were also outlined and a quantum dot embedded microdisk was successfully fabricated. However, much work in the efficient introduction of the colloidal quantum dots into such structures remain. Fabrication techniques need to be optimized to provide better device edge quality. These issues are currently being addressed by pursuing electron-beam lithography to resolve side wall roughness and alignment issues. Also the mechanisms governing the quenching of the quantum dots must be investigated.

3.4 REFERENCES

1. A. Kongkanand, K. Tvrdy, K. Takechi, M. Kuno, and P.V. Kamat, "Quantum dot solar cells. Tuning Photoresponse through size and shape control of CdSe-TiO_2 Architecture," J. Am. Chem. Soc., **130**, 4007-4015 (2008)

2. J. Zhao, J.A. Bardecker, A.M. Munro, M.S. Liu, Y. Niu, I.K. Ding, J. Luo, B. Chen, and A.K.-Y. Jen., " Efficient CdSe/CdS Quantum Dot Light Emitting diodes using a thermal polmerzied hole transport layer," Nano. Lett., **6**, 463-467 (2006)

3. P. Guyot-Sionnest, and M.A. Hines, " Intraband transitions in semiconductor nanocrystals," Appl. Phys. Lett., **72**, 6, (2008)

4. B.L. Wehrenberg, C. Wang, and P. Guyot-Sionnest, " Interband and intraband Optical studies of PbSe Colloidal Quantum Dots," J. Phys.Chem. B., **106**, 10634-10640 (2002)

5. M. Shim, S.V. Shilov, M.S. Braiman, and P Guyot-Sionnest, " Long-Lived Delocalized Electron States in Quantum Dots : A Step-Scan Fourier Transform Infrared Study," J. Phys. Chem. B., **104**, 1494-1496 (2000)

6. P. Snee, Y. Chan, D. Nocera, and M. Bawendi, " Whispering-Gallery-Mode lasing from a semiconductor nanocrystal laser," Appl. Phys. Let., **80**, 4614-4616 (2002).

7. A.V. Malko, A.A. Mikhailovsky, M.A. Petruska, J. A. Hollingsworth, H. Htoon, M.G. Bawendi, and V. I. Klimov, " From amplified spontaneous emission to microring lasing using nanocrystal quantum dot solids," Appl. Phys. Lett., **81**, 1303-1305 (2002).

8. C. Finlayson, D. Ginger, and N. Greenham, " Optical microcavities using highly luminescence films of semiconductor nanocrystals," Appl. Phys. Lett., **77**, 2500-2502 (2000)

9. P. Lodahl, A. Floris van Driel, I.S. Nikolaev, A. Irman, K. Overgaag, D. Vanmaekelbergh, and W. L. Vos, " Controlling the dynamics of spontaneous emission from quantum dots by photonic crystals," Nature., **430**, 654-657 (2004)

10. C. Poitras, M. Lipson, H. Du, M. Hahn, and T. Krauss, " Photoluminescence enhancement of colloidal quantum dots in a monolithic microcavity," Appl. Phys. Lett., **82**, 4032-4034 (2003)

11. M. Kahl, T. Thomay, V. Kohnle, K. Beha, J. Merlein, M. Hagner, A. Halm, J. Ziegler, T. nann, Y. Fedutik, U. Woggon, M. Artemyev, F. P. Willard, A. Leitenstorfer, and R. Braschitsch, " Colloidal quantum dots in all-dielectric high-Q pillar microcavities," Nano. Lett., **7**, 2897-2900 (2007)

12. K. Srinivasan, M. Borselli, O. Painter, A. Stintz, and S.Krishna., " Cavity Q, mode volume, and lasing threshold in small diameter AlGaAs microdisk with embedded quantum dots," Optics Express, **14**, 1094 (2006)

13. A. Yariv, " Critical Coupling and Its Control in Optical Waveguide-Ring Resonator systems," IEEE Photonics Technology Letters., **14**, 483-485 (2002).

14. A. Yariv, "Univeral relations for coupling of optical power between microresonators and dielectric waveguides," Electronics Letters., **36**, 4 (2000)

15. M.K. Chin, and S.T. Ho, " Design and Modelling of Waveguide Coupled Single Mode microring Resonators," Journal of Lightwave Technology., **16**, 8 (1998).

16. S.O. Kasap, " Optoelectronics and Photonics, Principles and Practices," Prentice Hall Inc., (2001)

17. K. Srinivasan, A. Stintz, S. Krishna, and O. Painter, " Photoluminescence Measurements of quantum-dot containing semiconductor microdisk resonators using optical fiber taper waveguides," Phys. Rev. B., **72**, 205318 (2005).

18. K. Srinivasan, and O. Painter, " Mode coupling and cavity-quantum dot interactions in a fiber-coupled microdisk cavity," Phys. Rev. A., **75**, 023814 (2007).

19. M. Pelton, C. Santori, J. Vuckovic, B. Zhang, G.S. Soloman, J. Plant, and Y. Yamamoto, " Efficient source of single photons: A single quantum dot in a micropost microcavity," Phys. Rev. Lett., **89**, 23 (2002).

20. P. T. Snee, Y. Chan. D.G. Nocera, and M.G. Bawendi, " Whispering-Gallery-Mode Lasing from a semiconductor nanocrystal/microsphere resonator composite," Adv. Mater., **17**, 11

21. J. Furst, H. Pascher, T. Schwarzl, M. Boberl, W. Heiss, G. Springhol, and G. Bauer, "Midinfrared IV-VI vertical-cavity surface-emitting lasers with zero-, two-,and three-dimensional systems in the active region," Appl. Phys. Lett., **81**, 2. (2002)

22. A. Mata, A.J. Fleischman, and S. Roy, "Fabrication of multi-layer SU-8 microstaructures," J. Micromech. Microeng., **16**, 276-284 (2006)

23. L. Pang, K. Tetz, Y. Shen, C.H. Chen, and Y. Fainman, " Photosensitive quantum dot composites and their applications in optical structures," J. Vac. Sci. Technol. B., **23** (2005).

Chapter 4. OPTICAL STUDIES OF ONE-DIMENSIONAL SILVER-NANOCOMPOSITE-DIELECTRIC PHOTONIC CRYSTAL

The aim of this chapter is to give a detailed technical and analytical insight on work done with silver nanocomposite. The focus here is the study of the linear and nonlinear optical properties of a one-dimensional metal nanocomposite-dielectric structure. However, before fabrication of the photonic crystal much work is done to characterize single metal nanocomposite films. To fully characterize these single nanocomposite films, dependence of factors such as concentration, fill-factor and temperature of synthesis on linear properties are investigated. In addition, we also investigate the dependence of concentration on the nonlinear optical properties of the nanocomposite films. Once these films were optimized for their optical properties, they are introduced into a one-dimensional photonic crystal. Linear and nonlinear optical characterization of the one-dimensional structure is carried out. Reflectivity measurements are carried out to investigate the interaction between the Bloch modes of the photonic crystal and plasmon absorption of the metal composite, which result in the formation of a broad reflection band. Nonlinear z-scan measurements carried out on the one-dimensional structure shows enhancement of nonlinear optical coefficients as compared to the single nanocomposite layer.

In the beginning of this chapter the standard methods and details of sample preparation are discussed. However specific concentrations of samples used for optical studies are dealt with, according to each section. Following this, we focus on optical studies on the single nanocomposite film. In this section both linear and nonlinear optical properties of the single nanocomposite films are discussed.

The final section of the chapter concentrates on the fabrication, and optical characterization of a one dimensional metal nanocomposite dielectric photonic crystal.

4.1 SILVER COMPOSITE

In this work a composite is defined as any material which is formed from two or more different constituents. Each constituent present is large enough so that it may be described by its bulk optical properties. At the same time the typical constituent (particle) dimensions and spacing are much smaller than the optical wavelength so that the composite may be described by effective optical parameters (which may be expressed as functions of the bulk constituents' optical parameters). Gold, Silver and Copper are known to display their plasmon resonance in the visible part of the spectral range. Silver exhibits the highest efficiency of plasmon excitation and hence provides a very useful system to investigate and implement strong light-matter interaction at the nanoscale. A single silver nanoparticle interacts with light more efficiently than a particle with comparable dimension composed of any known organic or inorganic chromophore. This is due to the extinction cross-section for silver being larger than the particle's geometric cross-section. Moreover silver is the only material whose plasmon resonance can be tuned to all wavelengths in the visible spectrum by varying its size, shape and dielectric environment. [1]

The incorporation of silver nanoparticles into a polymer matrix allows for exploiting its unique optical properties to be used in device applications. The resulting nanocomposite could exhibit novel optical properties as the plasmon resonance is strongly affected by

the surrounding dielectric environment (as discussed in chapter 1). The silver-PVA (Polyvinyl alcohol) nanocomposite developed for this work, provided ease of preparation and involved environmentally stable precursors. As the polymer acts as a reducing agent as well as a stabilizer for the silver nanoparticles it helps to prevent aggregation. The silver nanoparticles embedded in dielectric hosts are attractive for development of all-optical switching devices due to dielectric confinement effects such as nonlinear absorption and third order optical nonlinearities.

4.2 SAMPLE PREPARATION

Silver nanoparticles embedded in a thin film of poly (vinyl alcohol) (PVA) were synthesized by reduction of silver nitrate using PVA [2]. Silver nitrate is dissolved in 0.5 ml of water. This is added to a solution of PVA (which is prepared by mixing PVA with 5.2 ml of water). This solution is then spin-coated on a substrate and heated. The thicknesses of the films are controlled via the time and speed of spin coating. In addition, the optical absorption can be controlled via concentration and heating time of the sample. The film appears yellowish in color. The PVA acts as a reducing agent as well as a stabilizer for the silver nanoparticles. All samples discussed in this section are prepared using the above procedure. However the amount of silver nitrate and heating time are varied depending on studies carried and will be discussed when relevant throughout the chapter.

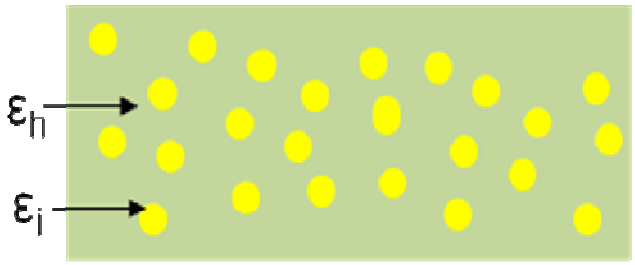

Figure 4.1 Schematic of Maxwell Garnett Geometry

4.3 MAXWELL GARNET THEORY

One of the most popular composite geometry considered consists of particles randomly dispersed in a host material as shown in Figure 4.1. This composite was considered by Maxwell Garnet [3] who in his famous paper of 1904 explained the linear optical properties of metal-doped glasses. In this model he assumed the particles to be spherical and uniformly distributed in size. In addition, the particle radius is assumed to be much smaller than the spacing between the inclusions (which are smaller than the optical wavelength).

A metal sphere in the presence of an oscillating electric field emits radiation like an electric dipole. In his paper, Maxwell Garnett replaced the spheres in the model by the equivalent point dipoles. The polarization density is then given by the sum of the polarization density of the host as [4, 5]:

$$P_{MG} = \chi_h E + N\alpha_i E_{loc} \tag{4.1}$$

where χ_h is the susceptibility of the host, α_i is the polarizability of a single nanoparticle, N is the number of nanoparticles per unit volume and $\mathbf{E}_{loc}$ is the Lorentz local field: this is the field experienced by the nanoparticles (macroscopic field minus the field of the

nanoparticles itself). The field in any point **r** in the medium is equal to the field generated by the dipoles contained in a sphere centered around the point itself plus the field generated by all other sources. As the diameter of the sphere becomes smaller the field (by all other sources) becomes closer to the local field because the field produced by the dipoles contained in the sphere becomes closer and closer to the field of the single dipole placed at **r**. The field generated by a spherical distribution of dipoles inside the sphere where the dipoles are contained is:

$$E_{sphere} = -\frac{4\pi}{3\varepsilon_h} P_{np} \tag{4.2}$$

where P_{np} in the Maxwell Garnett effective theory is the dipole density due to the nanoparticles:

$$P_{np} = N\alpha_i E_{loc} = N\alpha_i (E + \frac{4\pi}{3}\frac{1}{\varepsilon_h} P_{np}) \tag{4.3}$$

here $\alpha_i = R^3 \varepsilon_h \frac{\varepsilon_i - \varepsilon_h}{\varepsilon_i + 2\varepsilon_h}$. Using equation 1.1 and this expression we obtain the polarization density of the nanoparticles as a function of the macroscopic field E:

$$P_{np} = \frac{N\alpha_i}{1 - \frac{4\pi}{3}\frac{N\alpha_i}{\varepsilon_h}} E = \frac{3f}{4\pi}\varepsilon_h \frac{\frac{\varepsilon_i - \varepsilon_h}{\varepsilon_i + 2\varepsilon_h}}{1 - f\frac{\varepsilon_i - \varepsilon_h}{\varepsilon_i + 2\varepsilon_h}} E \tag{4.4}$$

where

$$f = N\frac{4\pi}{3}R^3$$

Summing the polarization density of the host to that of the nanoparticles, we obtain the effective susceptibility of the composite material [5]:

$$\chi_{MG} = \chi_h + \chi_{np} = \chi_h + \frac{3f}{4\pi}\varepsilon_h \frac{\frac{\varepsilon_i - \varepsilon_h}{\varepsilon_i + 2\varepsilon_h}}{1 - f\frac{\varepsilon_i - \varepsilon_h}{\varepsilon_i + 2\varepsilon_h}} \tag{4.5}$$

Converting susceptibilities to dielectric constants we obtain:

$$\frac{\varepsilon_{MG} - \varepsilon_h}{\varepsilon_{MG} + 2\varepsilon_h} = f\frac{\varepsilon_i - \varepsilon_h}{\varepsilon_i + 2\varepsilon_h} \tag{4.6}$$

In the above expression, the denominator can go to zero for the case of metals since the real part of the dielectric constant is negative. This is the basis of the plasmon resonance in the metal nanoparticles embedded films. [4, 5]

4.4 Linear Optical Characterization Of Single Metal Nanocomposite Films

4.4.1 Absorption

To quantify the absorbance variation with respect to silver concentrations, three concentrations of silver-PVA solution were prepared, 76 mg, 47.6 mg and 24.7 mg of silver nitrate were added to fixed concentration of PVA of 46 g/l in water. These solutions were spincoated on a clean glass substrate for 30 seconds at 3000 rpm and then heated for 60 minutes. Figure 4.2(a) shows the concentration dependence on the absorbance. As expected by increasing the concentration of silver nanoparticles we can increase the absorbance.

To demonstrate the effect of temperature of synthesis on absorbance, fixed concentrations of the silver precursor solution is used (76mg in 0.5ml of silver nitrate in 240 mg of PVA in 5.2ml of water) and spincoated for 30 seconds at 3000 rpm. Here the temperature is kept at 95^0C and the heating times are varied from 30 minutes to 60 minutes in 15 minute increment. As shown in Figure 4.2(b) the absorption increases with heating times.

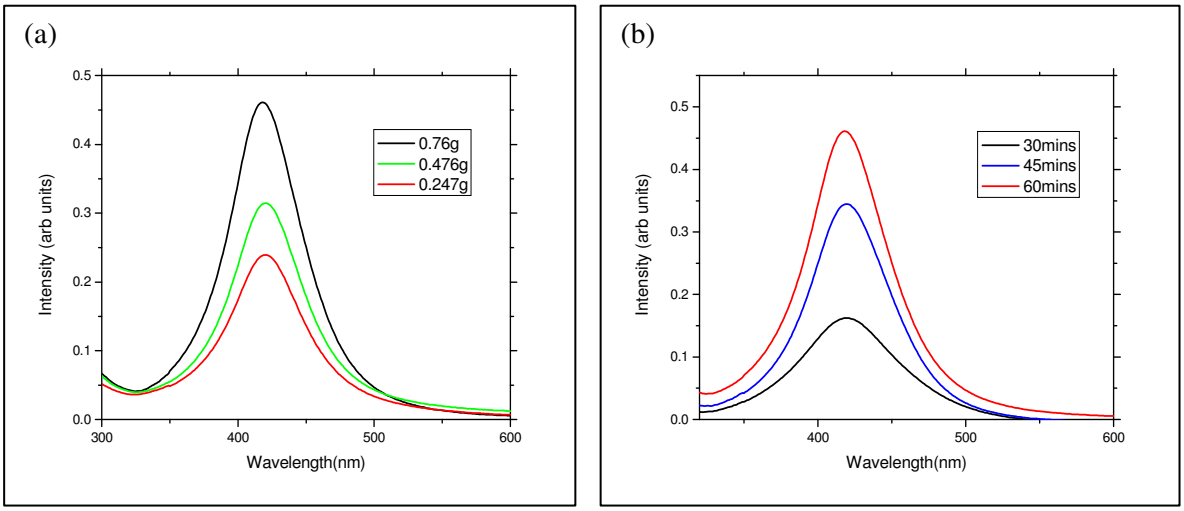

Figure 4.2 Absorption Spectrum showing variation of absorpion with (a) concentration of silver nanoparticles and (b) heating times

The peak of absorption occurs at the plasmon resonance of the silver nanoparticles ~ 420nm. Other studies done on the effect of heating time on intensity, peak maximum, line width of the plasmon absorption for different weight ratios is given in Ref [2]. Here it is shown that the nanoparticles production increases with time and reaches saturation after an hour. In addition a small blue shift of peaks with heating time is also observed indicating a decrease in particle size. Furthermore a reduction in the plasmon absorption line width is attributed to the increasing mondispersity of the size. However concentration plays a significant role in the production, size and saturation point of the

silver-PVA composite [2]. With smaller concentrations of silver to PVA, saturation was not reached at lower temperatures and variation in size distribution was prominent. With higher concentration, temperature and longer heating times, the size distribution and ordering of the particles was significantly improved.

Figure 4.3 demonstrates a comparison of the linewidth of the single nanocomposite film shown in Figure 4.2 (b). Here in addition to the decrease of linewidth with heating time, a small but steady blue-shift is observed.

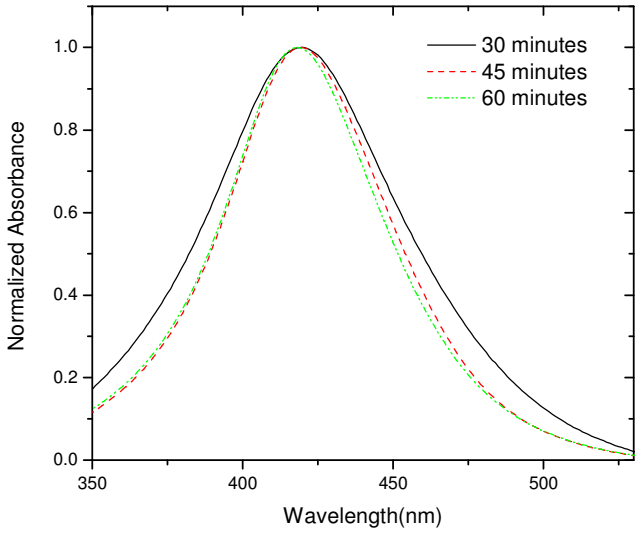

Figure 4.3 Shows linewidth comparison of single nanocomposite film for varying heating times. The decrease in linewidth and a blue-shift is seen with increase of heating time.

This blue-shift is attributed to a decrease in particle size with heating and the decrease in linewidth corresponds to the decrease in size dispersion.

Here the parameters from Ref [2] are used to optimize the concentration, heating time and temperature of the silver-PVA nanocomposite films to study the refractive index property of the composite films. Since the absorption is directly related to the extinction

coefficient of the material, one can tune the dielectric property of the medium by adjusting parameters such as concentration, temperature and heating time to obtain the desired absorption spectra.

4.4.2 ELLIPSOMETRY

Ellipsometry has proven to be an extremely versatile and powerful optical technique used to investigate the dielectric properties of thin films. The theory of ellipsometry is discussed in chapter 2. Ellipsometric measurements on samples covered in this thesis were carried out in reflection mode and are prepared as described in section 4.2.

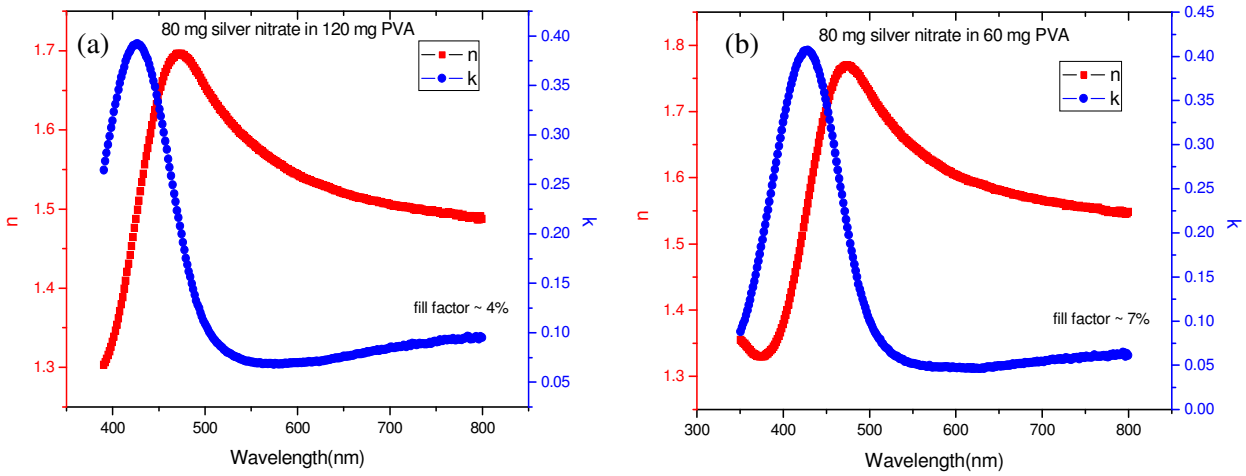

Figure 4.4 Effective index of two silver composite films with fill-factor (a) 4% and (b) 7% calculated using ellipsometry

Due to very low concentration of silver nanoparticles, high fill-factors were not achieved with the concentrations described above. Hence, silver nitrate was increased to 80 mg (dissolved in 0.5ml of water) and was added to 60 mg and 120 mg of PVA (dissolved in 5.2 ml of water).

These were spin coated on a silicon substrate (to ensure efficient reflectivity during ellipsometry) for 20 seconds at 3000 rpm and heated at 95°C for 90 minutes. The films are yellowish in color and fairly uniform. The color intensity increases with heating time and concentration (discussed in section 4.3). The reflectivity attained from these films was fitted to a model described by the Maxwell-Garnett effective medium theory. The model assumes a mixture of two distinct materials which possess the optical properties of the bulk counterpart. The theory requires a low fill factor so as to avoid inter-particle interaction. Figure 4.4 (a) and (b) shows the complex dielectric function of these two films. Once again as expected, increase of silver nitrate concentration increases the effective n and k of the composite. Using this method the highest fill factor achieved for a silver composite film was 7%. This film will be used for all further experiments discussed in this chapter. [6]

4.5 NONLINEAR OPTICAL CHARACTERIZATION

One of the most significant properties of metal nanoparticles is the nonlinear optical (NLO) response with distinguishes them from the bulk material. This is due not only to their atomic scale structures but also their interface and surface structures. Materials with large third-order optical nonlinearity and fast response time are essential for future optical device applications. High nonlinear optical response of these nonlinear materials makes them good candidates for applications such as all-optical switching, digital signal restoration and optical limiter applications.

4.5.1 NONLINEAR MEASUREMENTS ON SINGLE NANOCOMPOSITE FILM

In this section we discuss our results of nonlinear optical studies via z-scan measurements of our single nanocomposite film. Z-scan measurements are taken using the setup described in chapter 2. The Z-scan set up consists of an optical parametric amplifier source with a 120 fs pulse width and a repetition rate of 1 KHz. The excitation wavelength used in this experiment was 840 nm which is twice the Plasmon resonance frequency of the silver nanoparticles (~420 nm) so as to induce two photon absorption (TPA). The average power used for the single nanocomposite films is 1mW. Using this power, the repetition rate f and the pulse width τ_p, the beam waist radius w_0 and the Rayleigh length z_0, the power delivered, I_{pulse}, is calculated as follows:

$$\begin{aligned} P_{average} &= E_{pulse} f \\ P_{peak} &= \frac{E_{pulse}}{\tau_p} \\ I_{pulse} &= \frac{P_{peak}}{z_0 \lambda} \; where \quad z_0 \lambda = \pi w_o^2 \end{aligned} \tag{4.7}$$

For the single composite film sample, I_{pulse}=27 GW and the aperture transmission for open aperture measurements was fixed at S=95.8%.

Open Aperture z-scan measurements were carried out for two concentrations of silver composite films discussed in section 4.4.2. The silver films were prepared as discussed in section 4.2 and spincoated for 20 seconds at 2000 rpm and heated for 90 minutes at 95°C to give a film thickness of 120 nm. The nonlinear transmission is shown in Figure 4.5. Here the nonlinear transmission is fitted to the function:

$$T_{OP}(z) = 1 - \frac{q_0}{2\sqrt{2}(1+x^2)}$$
$$where\ q_0 = \beta I L_{eff};\ L_{eff} = \frac{1-e^{-\alpha L}}{\alpha};\ x = \frac{z}{z_0}\ and\ z_0 = \frac{\pi w_0^2}{\lambda} \tag{4.8}$$

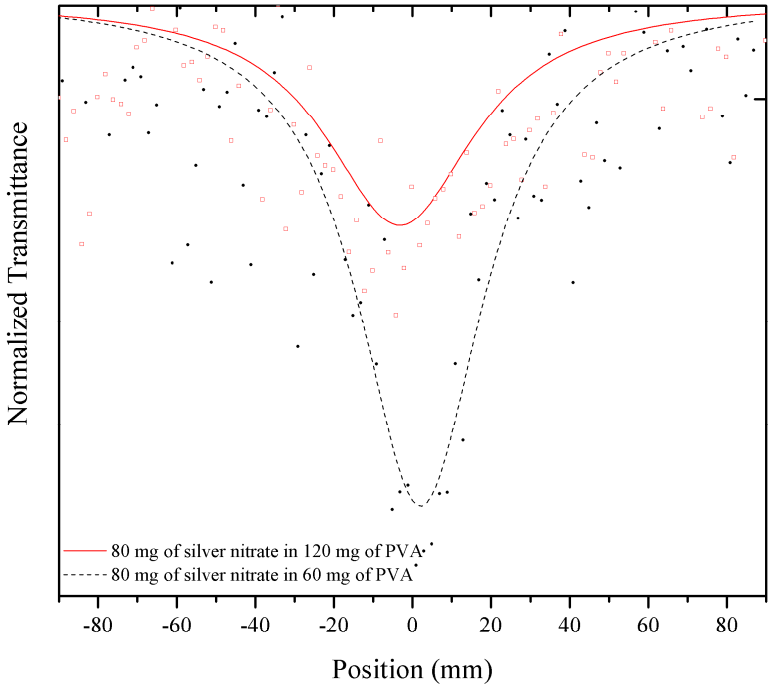

Figure 4.5 Open Aperture z-scan experiment shows enhancement of nonlinear optical properties for higher concentration of silver nanocomposite film

It can be seen that as concentration of the silver nanoparticles in the host medium is increased, there is an enhancement in the nonlinear absorption.

To prove that the absorption observed was due to the silver nanoparticles, a control sample of PVA in the absence of silver nanoparticles was also measured. Figure 4.6 clearly shows the dip in nonlinear transmission, only for the sample containing the silver nanoparticles. The concentration of PVA was kept fixed for both the curves and the

addition of the silver composite was the only varying factor. The silver nanocomposite film in Figure 4.6 was prepared by spincoating the precursor solution for 20 second at 500 rpm to attain a film thickness of approximately 1 micron.

For this film the parameters are fitted to be $z_0 = 3.604cm, q_0 = 0.32687$ and $\alpha = 0.0129$ which is the linear absorption coefficient calculated by absorbance measurements (at 840 nm).

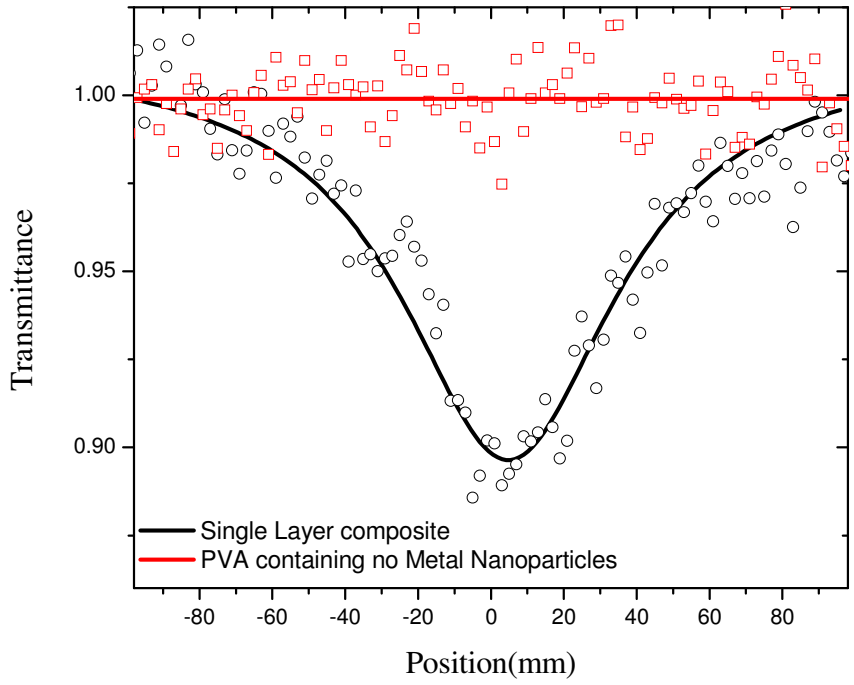

Figure 4.6 Open Aperture experiment of two films with the presence (black) and absence (red) of silver nanoparticles. It can be seen that the silver nanoparticles lead to a dip in nonlinear transmission

The effective length L_{eff} is calculated to be 1000nm. Hence using the equations above the nonlinear absorption coefficient is calculated as $\beta = 1.01 \times 10^{-7} cm/W$.

Closed aperture z-scan experiments were performed by adjusting the aperture to allow 31% linear transmittance. The closed aperture data for the single composite film is shown in Figure 4.7.

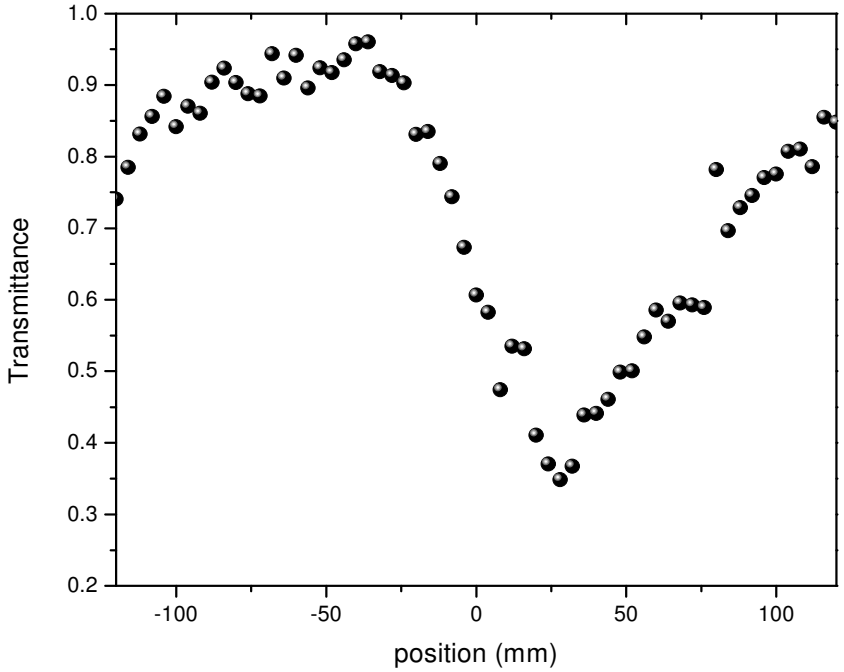

Figure 4.7 Closed Aperture data of the single nanocomposite film of thickness (~1000nm). It is seen that the data does not show the usual symmetry (about focus) instead there is a strong suppression of the transmission peak due to the high NLA

It can be seen that due to the strong nonlinear absorption there is a strong suppression of the transmission peak. This data contains both the nonlinear absorption and nonlinear refractive components as discussed in section 1.3. To fit this function to a purely refractive form, the closed aperture data is divided by the open aperture data (shown in Figure 4.8). This allows fitting the normalized closed/open aperture data to a purely refractive function:

$$T_{CA/OA}(z) = 1 + \frac{4x}{(9+x^2)(1+x^2)}\Delta\Phi \quad where\ \Delta\Phi = \mathrm{kn}_2 I_0 \mathrm{L}_{\mathrm{eff}}\ and\ x = \frac{z}{z_0} \tag{4.9}$$

Using the closed aperture data, we can calculate the nonlinear refractive index by deducing the peak-valley distance (as explained in chapter 2)

$$\Delta T_{p-v}(z) \cong 0.406(1-S)^{0.25}\left|\Delta\Phi\right| \tag{4.10}$$

Using these values the nonlinear refractive index of the single composite is calculated to be: $n_{(2-single)} = 7.5 \times 10^{-12} cm^2 / W$.

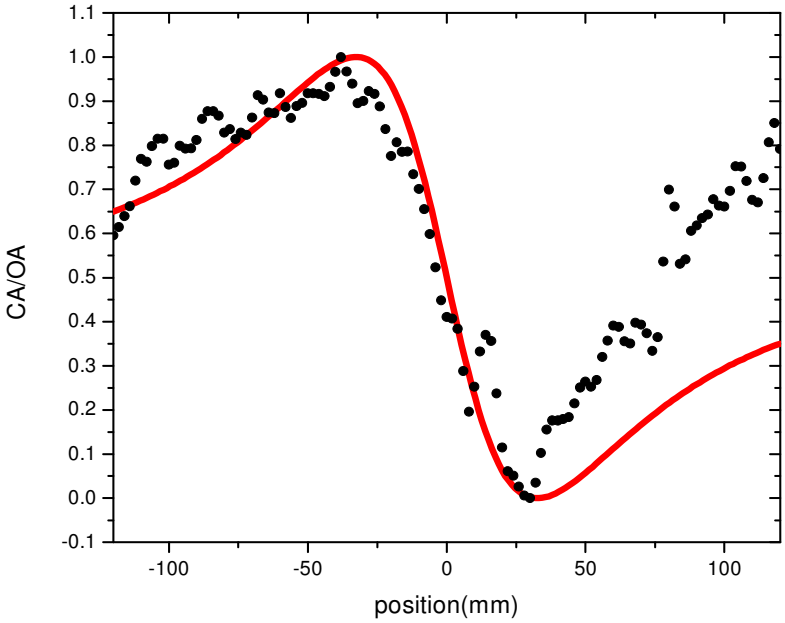

Figure 4.8 Normalized fitted spectra of closed divided by open aperture data of the single composite film

4.6 PHOTONIC STRUCTURES EMBEDDED WITH METAL NANOPARTICLES

The linear and nonlinear optical properties of photonic crystals can be manipulated by control of electromagnetic field through the modification of their geometry and dielectric properties. This capability has in turn led to a variety of applications of both fundamental

and technological importance such as control of luminescence properties of emitters, engineering group velocity and refraction properties of light, development of efficient photodetectors, sensors and novel devices like super prisms [7-14]. More recently metal-dielectric photonic crystals have received much interest due to their highly dispersive properties and the possibility to exploit the optical nonlinearity of metals. Such structures have been realized in one, two and three-dimensions and use a combination of bulk metal and dielectric materials [15-20]. The optical properties in these structures are controlled by their geometry, and the plasmon frequency of the bulk metal. It was shown that by engineering these characteristics through careful design, it is possible to exploit the linear and nonlinear optical properties of the metals. [21-28]

Here a new degree of tunability is added to the optical properties of the metal-dielectric photonic crystals by replacing the metal component of the structure with a composite material containing metal nanoparticles. Through control of fill factor, size and shape of metal nanoparticles one can control the metallicity of the layers and their plasmon resonance, thus providing two additional tuning parameters. In this section the optical properties of a one-dimensional photonic crystal consisting of alternating layers of a metal composite is studied. An enhancement in reflectivity band is demonstrated, when the photonic bandgap approaches the plasmon resonance of the embedded silver nanoparticles. This enhancement is attributed to the interaction between the absorption due to plasmon resonance of the metal nanoparticles and the Bloch modes of the photonic crystal. The nonlinear optical properties of this structure are investigate via z-scan measurements and compared to single metal nanocomposite film of comparable thickness. It is shown that the nonlinear properties of the one-dimensional metal-

nanocomposite dielectric photonic crystal are significantly enhanced. The section begins with a brief introduction outlining the basic theory of photonic crystals for the benefit of the reader.

4.6.1 THEORETICAL FRAMEWORK OF ONE-DIMENSIONAL PHOTONIC CRYSTALS

The study of electromagnetic wave propagation through periodic media dates back to Lord Rayleigh in his paper [29] where he derived the magnitude of a forbidden gap. The term "photonic crystal" was coined a century later after Eli Yablonovitch and Sajeev John published two very notable papers on photonic crystals [30, 31].

A one-dimensional photonic crystal consists of alternating stacks of materials with varying refractive index is shown as an inset in Figure 4.9.

This sort of periodic arrangement is the optical analogue of electrons propagating through a periodic potential which may consist of gaps in the energy band structure where electrons are forbidden to propagate with certain energies in certain directions.

In a photonic crystal we replace the periodic atomic potential with a structure consisting of periodic dielectric function. An important characteristic of a one-dimensional photonic crystal is its high reflectance in the photonic band gap. A plot showing the reflectivity of a one-dimensional photonic crystal is shown in Figure 4.9.

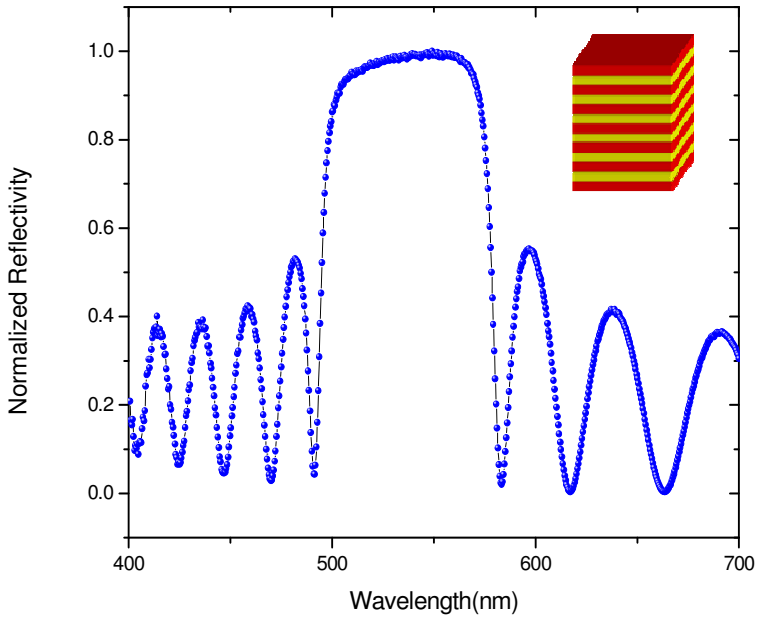

Figure 4.9 Reflectivity plot of a one-dimensional photonic crystal consisting of alternating layers of SiO_2 (n=1.45) and SiN (n=1.78) (inset shows schematic of the 1D structure)

In photonic crystals the periodicity of the structure allows one to define a Brillouin zone in the **k**-space. The photonic band gap is created by discontinuities of the dispersion curve at the end of the Brillouin zone. Optical modes in this photonic band gap are not allowed to propagate or exist in the photonic crystal. The shape and width of the reflection band depends on the dielectric contrast of the layers as well as their thicknesses. Thus through appropriate design, photonic crystals can be used to control the spatial and spectral properties of the electromagnetic field.

These one-dimensional photonic crystals can be used to engineer the linear and nonlinear optical properties of various materials. Much work has been done to introduce bulk metal into these photonic crystals. However the inclusion of bulk metal considerably suppresses

the field due to their high absorption. In this thesis we explore the linear and nonlinear optical properties of a one-dimensional photonic crystal embedded with a metal nanocomposite. By integrating the photonic crystal with a metal composite one is able to tune the optical properties of the metal composite to allow for enhancement in the linear and nonlinear optical effects while rendering the structure fairly transparent.

4.6.2 Linear Optical Properties of a One-Dimensional Metal-Nanocomposite Dielectric Photonic Crystal

Schematic drawing of a one dimensional metal nanocomposite dielectric photonic crystal is shown in Figure 4.10 (a). Transfer matrix based simulation is used to model the one dimensional structure where the alternating layers are assigned to be Polymethyl methacrylate (PMMA) with refractive index of 1.489 and the silver nanocomposite (with a fill factor of 7%) whose index was described in section 4.1.2. The index of PMMA is taken to be constant in the range of interest as PMMA is seen to have negligible dispersion in the wavelength range of interest. The thicknesses of the layers (d_{PMMA} ~ 96 nm, and d_{AgNC} ~ 115 nm) are chosen such that the spectral position of the Bragg reflection band can be tuned into the plasmon resonance of the silver nanoparticles.

Under this condition we see the modification of the reflection band which becomes much wider than the Bragg bandgap as seen in Figure 4.10(b).

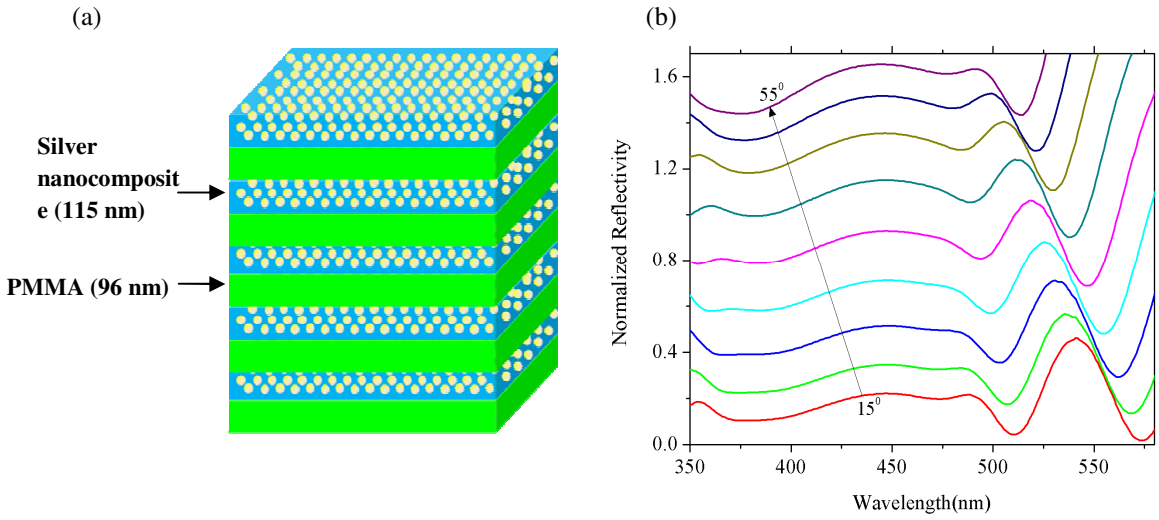

Figure 4.10 (a) Schematic drawing of one-dimensional metal nanocomposite-dielectric photonic crystal. (b) Results of transfer matrix based simulation carried out on such a structure consisting of alternating layers of silver nanocomposite and PMMA indicating the modification of reflection band near the plasmon resonance.

To demonstrate the effect of the silver nanocomposite on the one-dimensional photonic crystal, a similar transfer matrix based simulation is carried out on a structure not consisting of the silver composite. The structure is assigned the same thicknesses of PVA and PMMA as shown in Figure 4.10 (a). Without the silver composite, a standard Bragg reflectivity is predicted and seen and is shown in Figure 4.11.

The one-dimensional photonic crystal structure is then realized by spin coating alternating layers of PMMA and the silver nanocomposite. Spin coating can be used to realize these structures because PMMA dissolves in nonpolar solvents such as toluene and PVA dissolves polar solvents such as water.

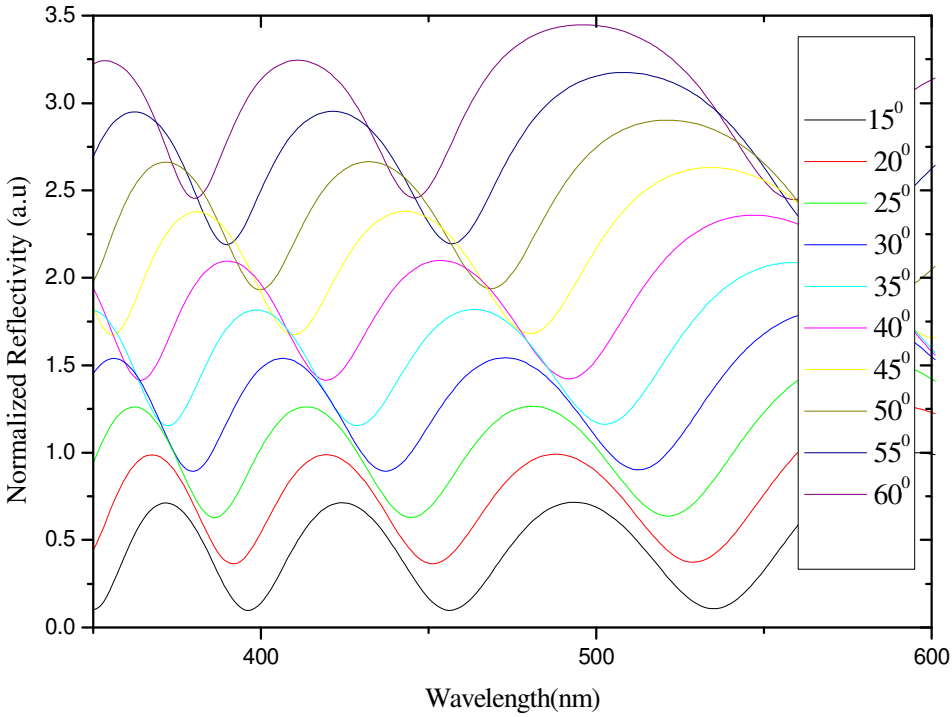

Figure 4.11 Transfer matrix based simulation on the one-dimensional structure consisting of alternating layers of PVA (115nm) and PMMA (96nm).

This incompatibility of the solvents preserve the integrity of the layers while spin coating multiple layers on top of each other. Similar technique has been used in the past to realize flexible microcavities [32]. The PMMA solution is prepared by mixing 0.27g of PMMA with 13.5 ml toluene. The silver nanocomposite prepared using technique discussed in section 4.2.1 is spun at 3000 rpm for 20 seconds giving a layer thickness of 115 nm, while the PMMA layer is spin coated at 7000 rpm for 30 seconds to attain a 96nm thick layer.

The one-dimensional metal-dielectric photonic crystal structure is composed of 10 alternating layers of PMMA and the silver nanocomposite. Angle dependent reflectivity measurements are carried out using a white- light source and a CCD based spectrometer.

Results of these measurements are shown in Figure 4.12. It can be seen that as the reflectivity peak is tuned in toward the silver plasmon resonance a modification in the bandgap is observed. The reflectivity peak broadens due to the overlap of the band edge of the Bragg reflection band with the plasmon resonance of the silver nanoparticles shown in Figure 4.12.

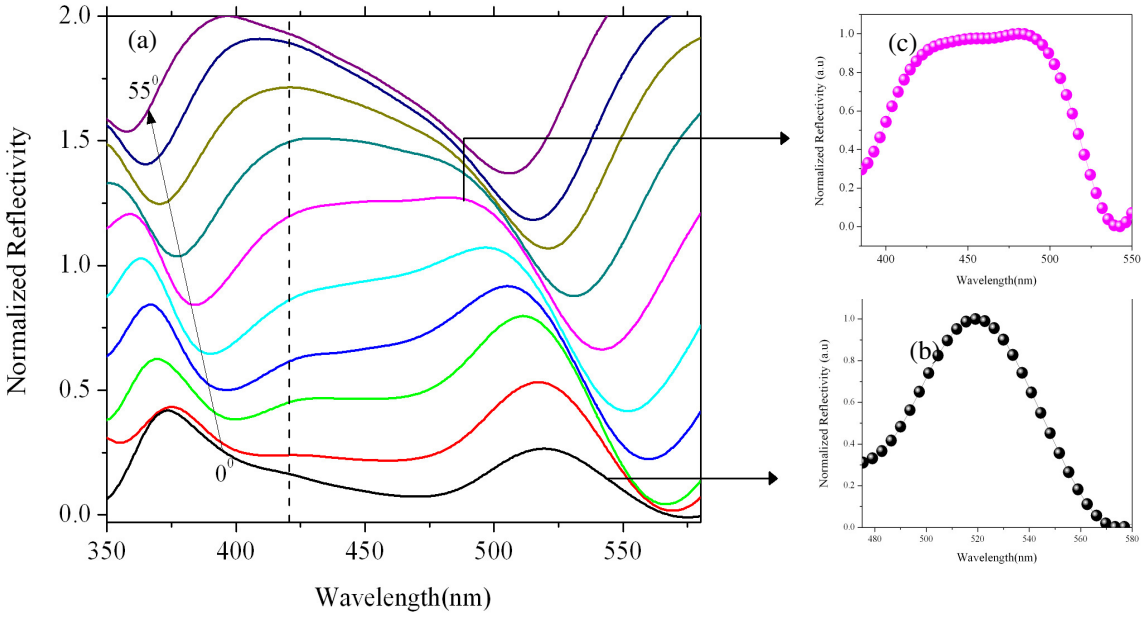

Figure 4.12 (a) Angle dependent reflectivity on 1-D metal dielectric structure. The panel on the right shows the zoomed in plots of the reflection band when the Bragg peak is far from the silver NP resonance (b) and in resonance (c).

In Figure 4.13 a comparison of the one-dimensional structure with the presence and absence of the silver composite is shown for reflectivity at 35°. The reflection band is seen to be significantly broader than the Bragg related bandgaps of the one-dimensional structure without the silver composite.

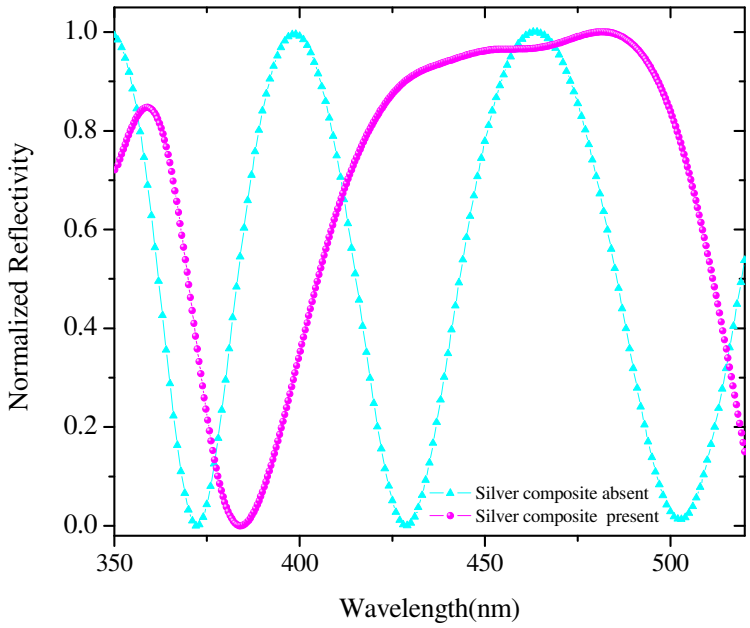

Figure 4.13 Reflectivity comparison of a one-dimensional structure with and without the silver composite (at an angle of 35°). It is seen that the metal nanocomposite dielectric structure exhibits a significantly broader reflection band compared to the 1D structure consisting of only PVA and PMMA layers.

Although the absolute maximum reflectivity of the present structure is only ~ 40%, this can be improved by increasing the number of periods and the refractive index contrast between the layers. The latter can be engineered by controlling the fill factor of the metal nanoparticles

For a system without absorption, bandgaps are defined as spectral regions with complex-valued solutions to the dispersion equations for Bloch wave numbers $kD = \pi m + i\xi(\omega)$, where D is the period of the structure and $m = 0,1,2\cdots$. A weak absorption usually makes the real part of the wave vector differ from $m\pi$ and weakly dependent on frequency, therefore blurring the boundaries of the bandgaps. In the system under consideration the plasmon-induced resonance absorption plays a more peculiar role. We analyzed the band structure of our structure using effective refractive index of Maxwell-

Garnett effective medium [3], which can be presented in the form typical for a polar dielectric $n_c = \sqrt{\varepsilon_{eff} \frac{\omega^2 + i\gamma\omega - \omega_L^2}{\omega^2 + i\gamma\omega - \omega_T^2}}$ where we introduced effective parameters:

$$\varepsilon_{eff} = \varepsilon_h \frac{\varepsilon_\infty (1+f) + \varepsilon_h (2-f)}{\varepsilon_\infty (1-f) + \varepsilon_h (2+f)} \text{ and}$$
$$\omega_L^2 = \omega_p^2 \frac{\varepsilon_\infty (1+f)}{\varepsilon_\infty (1+f) + \varepsilon_h (2-f)}; \omega_T^2 = \omega_p^2 \frac{\varepsilon_\infty (1-f)}{\varepsilon_\infty (1-f) + \varepsilon_h (2+f)} \quad (4.11)$$

expressed in terms of bulk plasmon frequency ω_p, fill factor f, dielectric constant of the host material ε_h and parameters ε_∞ and γ characterizing dielectric function of the metal inclusions taken in the Drude model: $\varepsilon_i = \varepsilon_\infty \left(1 - \omega_p^2 / \omega(\omega + i\gamma)\right)$.

In the absence of absorption the structure under consideration would have possessed a polariton band between ω_T and ω_L as well as a set of Bragg related bandgaps, which would accumulate in the vicinity of ω_T [33]. In this spectral region the Bloch phase kD would have experienced increasingly fast changes between 0 and π caused by divergence of the refractive index n_c at ω_T as shown in black in Figure 4.14.

Absorption washes out such oscillations producing a Bloch bandgap adjacent to ω_T, where the real part of Bloch wave number stays approximately equal to π, followed by the propagating band. If this band-gap is far enough from ω_T, (and absorption is small) the respective propagating band is characterized by the Bloch phase decreasing from π to 0 as the frequency approaches ω_T, after which a polariton band-gap is situated.

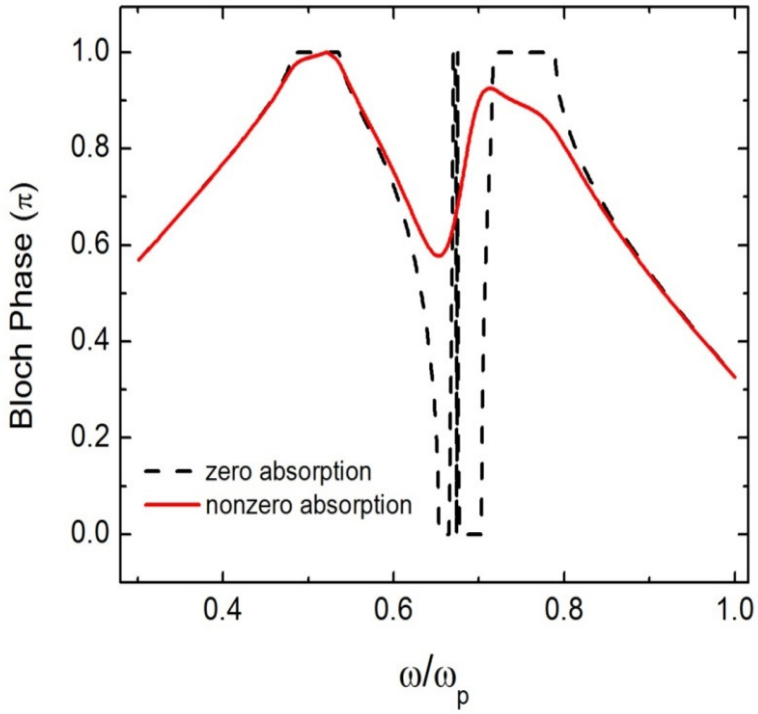

Figure 4.14 Calculated Bloch phase for the metal nanocomposite – dielectric photonic crystal structure in the presence (red) and absence (black) of absorption. It is seen that the Bloch phase stays in the vicinity of π when absorption is introduced which explains the broader reflection band observed experimentally. Here ω_p is the bulk plasmon frequency of silver.

By changing the angle of propagation the Bragg bands move toward to the polariton band. In this scenario, the role of absorption becomes much more significant, and it prevents the real part of the Bloch wave number to decrease significantly from π before it starts increasing again due to effects of the polariton band as shown in red in Figure 4.14. As a result, the band structure is significantly modified as the Bloch phase remains very close to π over a broad spectral region, which essentially mimics formation of a broad bandgap and is manifested in the observed reflection spectra. It should be emphasized

that this is a result of interplay between Bragg band structure and plasmon related absorption.

In summary, we have demonstrated the enhancement of reflectivity band in a one-dimensional photonic crystal consisting of alternating layers of silver nanocomposite and a dielectric. This enhancement is attributed to the interplay between the absorption at the plasmon resonance of the metal nanoparticles and the Bloch modes of the photonic crystal which causes the Bloch phase to remain close to π over a wider spectral range. This effect should be observable with any type of metal nanoparticle and the reflectivity can be controlled by changing the refractive index contrast and the number of periods of the structure. Such metal nanoparticle embedded photonic crystals will allow one to realize structures with engineered linear and nonlinear optical properties for applications such as all-optical switches, broadband reflectors and optical limiters.

4.6.3 NONLINEAR OPTICAL PROPERTIES OF ONE-DIMENSIONAL METAL DIELECTRIC PHOTONIC CRYSTAL

The one-dimensional metal nanocomposite dielectric structure discussed above was probed for its nonlinear optical properties via open- and closed-aperture z-scan measurement. The Z-scan set up consists of an optical parametric amplifier operating with a 120fs pulse duration and a repetition rate of 1KHz. The excitation wavelength used in this experiment is 840nm which is double the plasmon resonance frequency of silver nanoparticles to induce two photon absorption (TPA).

The entire structure as shown in Fig. 4.10(a) was realized by spin coating ten alternating layers of the silver composite and polymethy-methacrylate (PMMA). The PMMA

solution is prepared by mixing 0.59 g of PMMA with 21.6ml toluene. The PMMA is spin coated for 50 seconds at 8000 rpm to give a thickness of 120 nm while the silver composite layer is spin coated for 5 seconds at 500 rpm and then ramped to 1000 rpm for 10 seconds to attain a thickness of 160 nm. The combined thickness of the silver composite in the one-dimensional structure is created so as to be comparable with that of the single thick film (of 1000 nm) mentioned in section [4.6.2]. The layer thicknesses in the one-dimensional structure are chosen such that the band edge mode overlaps with the metal composite layers as shown in Figure 4.15 (a). The intensity with respect to the index profile is shown in Figure 4.15 (b), here it is shown that with the chosen layer thicknesses the field is localized mostly in the metal composite layers. This is done so as to enhance the nonlinear absorption.

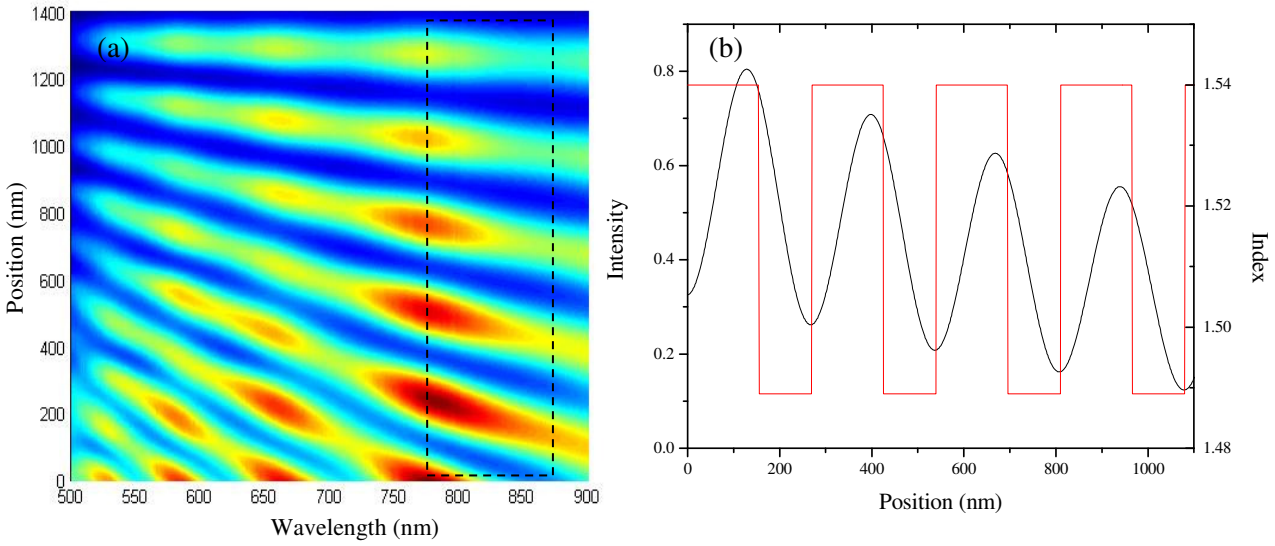

Figure 4.15 (a) Shows E-field localized at ~ 840 nm to enhance nonlinear response (b) Intensity profile in the one-dimensional metal nanocomposite dielectric structure with respect to position and index, shows Field localized within metallic layers.

Furthermore, linear transmission measurements were carried out on the one-dimensional metal nanocomposite dielectric structure, which is shown in Figure 4.16. By using a metal nanocomposite, a transmission of > 90% at the excitation wavelength is achieved. This design was used to enhance the nonlinear optical response of the structure.

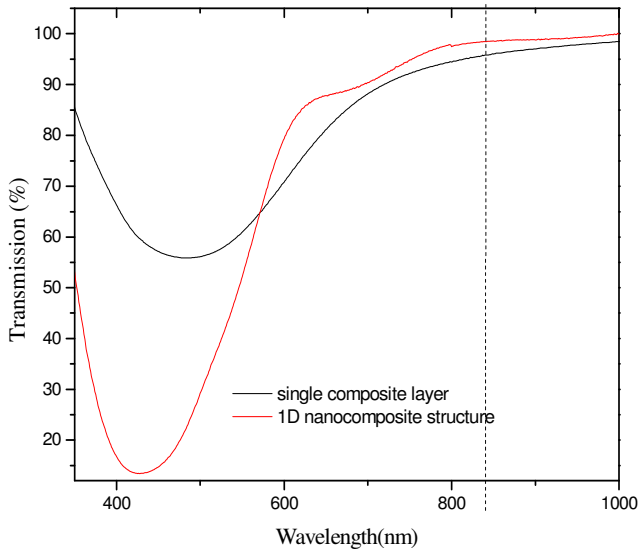

Figure 4.16 Transmission measurements carried out on the 1-D structure shows linear transmission >90%

Open aperture z-scan measurements are carried with an intensity of 21GW, which is calculated as described in section using the fitting parameters $z_0 = 52.8mm$ and $q_0 = 0.984$. Figure 4.17 shows the enhancement of nonlinear transmission of the one-dimensional metal dielectric structure compared to the single composite of comparable thickness. The nonlinear transmission is fit to the equation 4.8 and the fitting parameters are $z_0 = 52.8mm$ and $q_0 = 0.984$. It is seen that the one-dimensional structure has a significantly higher nonlinear transmission than the single composite film. Using equations 4.8 the nonlinear absorption coefficient β is calculated to be $3.67 \times 10^{-7} cm/W$.

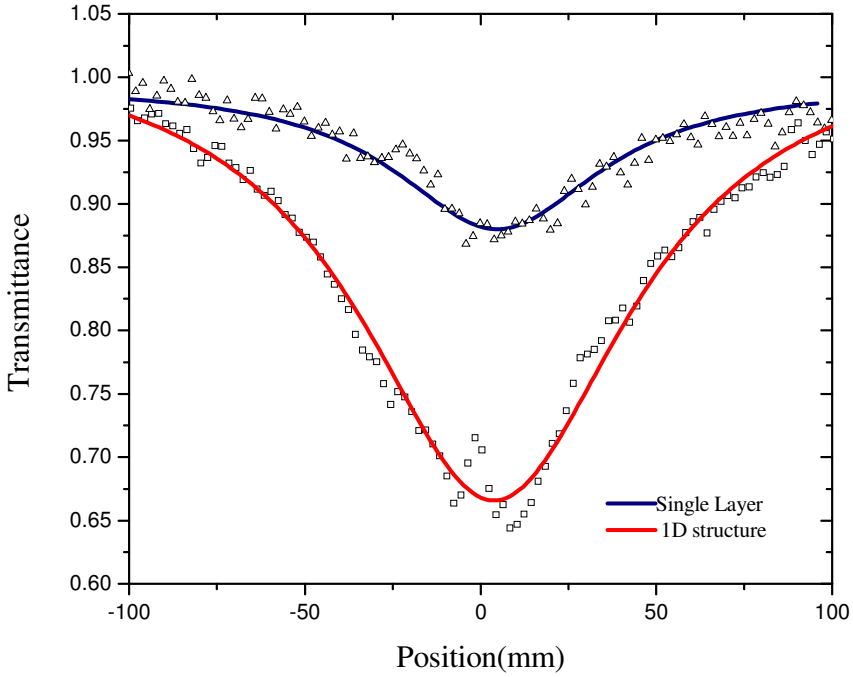

Figure 4.17 Open aperture nonlinear transmission for 1D metal nanocomposite dielectric structure showing greater nonlinear enhancement that single layer nanocomposite of comparable thickness

To estimate the nonlinear enhancement of the 1-D structure compared to the single nanocomposite layer, an enhancement ratio is calculated as follows:

$$\frac{\beta_{1D}}{\beta_{single}} \approx 3 \tag{4.12}$$

Thus through control of the electromagnetic field in the one-dimensional metal nanocomposite structure, a higher nonlinear absorption coefficient as compared to a single layer of silver nanocomposite consisting of approximately the same thickness of the composite is demonstrated.

4.7 CHAPTER SUMMARY

In summary, the optical properties of single metal composite films were studied. Temperature and concentration studies of the single metal composite films show that the optical properties can be varied quite easily. In addition by varying fill-factor one can alter the dielectric constant of the metal composite. Finally, by embedding the nanocomposite into a one-dimensional photonic crystal, a Plasmon induced enhanced reflection band was observed. It is shown that due to the interaction between the Plasmon resonance of the silver nanoparticles and the Bloch modes of the photonic crystal a broadened feature in the reflectivity spectra is seen.

In addition, nonlinear z-scan measurements show a enhancement factor of 3 in the nonlinear absorption for the one-dimensional structure compared to a single layered of metal composite consisting of the same thickness of the silver composite.

4.8 REFERENCES

1. G. Chumanov, and D.D. Evanoff Jr , " Synthesis and Optical Properties of Silver nanoparticles and Arrays," Chem Phys., **6**, 1221-1231 (2005)

2. S. Porel, S. Singh, S.S. Harsha, D.N. Rao, and T.P. Radhakrishanan, "Nanoparticle-Embedded Polymer: In Situ Synthesis, Free-Standing Films with Highly Monodisperse Silver Nanoparticles and Optical Limiting," Chem. Mater., **17**, 9-12 (2005)

3. J.C Maxwell Garnett, "Colors in metal glasses and in metallic films," Philosophical Transactions of the Royal Society of London. Series A., Containing Papers of a Mathematical of Physical Character., **203**, 385-420 (1904).

4. A. Moores, and F. Goettmann, " The Plasmon band in noble metal nanoparticles: an introduction to theory and applications," New J. Chem., **30**, 1121-1132 (2006)

5. R.J. Gehr, and R.W. Boyd, " Optical Properties of Nanostructures Optical Materials," Chem. Mater., **8**, 1807-1819

6. J.A. Woolam Co., Inc, Guide to using WVASE- Spectroscopic Ellipsometers and Thin film Characterization.

7. P. Lodahl. P, A.F van Driel, I.S Nikolaev, A. Irman, K. Overgaag, D. Vanmaekelbergh, and W.L Vos, "Controlling the dynamics of spontaneous emission from quantum dots by photonic crystals," Nature., **430**, 654-657 (2004).

8. Y.A. Vlasov, M. O'Boyle, H.F. Hamann, and S.J. McNab, "Active control of slow light on a chip with photonic crystal waveguides," Nature., **438**, 65-69 (2005).

9. H. Gersen, T.J. Karle, R.J.P. Engelen, W. Bogaerts, J.P. Korterik, N.F. val Hulst, T.F Krauss, and L. Kuipers, "Real space observation of ultraslow light in photonic crystal waveguides," Phys. Rev. Lett., **94**, 073903 (2005).

10. D. Goldberg, L.I. Deych, A.A. Lisyansky, Z. Shi, V.M. Menon, V. Tokranov, M. Yakimov, and S. Oktyabrsky, "Exciton-lattice polaritons in multiple-quantum-well-based photonic crystals," Nat. Photonics., **3**, 662-666 (2009).

11. B. Temelkuran, E. Ozbay, J.P. Kavanaugh, G. Tuttle, and K.M. Ho, "Resonant cavity enhanced detectors embedded in photonic crystals," Appl. Phys. Lett., **72**, 2376 (1998).

12. M. Lee, and P.M. Fauchet, “Two-Dimensional Silicon Photonic Crystal Based Biosensing Platform For Protein Detection,” Opt. Express., **15**, 4530-4535 (2007).

13. H. Kosaka, T. Kawashima, “Superprism phenomena in photonic crystals,” Phys. Rev. B., **58**, 10096-10099 (1998).

14. T. Ochiai, and J. Sanchez-Dehesa, “Superprism effect in opal-based photonic crystals,” Phys. Rev. B., **64**, 245113 (2001).

15. N. N. Lepeshkin, W. Kim, V.P. Safonov, J.G. Zhu, R.L. Armstrong, C.W. White, R.A. Zuhr, and V.M. Shalaev, “ Optical Nonlinearities of Metal Dielectric Composites,” Journal of Nonlinear Optical Physics and Materials., **8**, 191-210 (1999)

16. V. Kuzmiak, and A.A. Maradudin, "Photonic band structures of one- and two-dimensional periodic systems with metallic components in the presence of dissipation," Phys. Rev. B., **55**, 7427 (2007).

17. K.A. McIntosh, L.J. Mahoney, K.M. Molvar, O.B. McMahon, S. Verghese, M. Rothschild, and E.R. Brown, “Three-dimensional metallodielectric photonic crystals exhibiting resonant infrared stop bands,” Appl. Phys. Lett., **70**, 2937-2939 (1997).

18. M. Scalora, M.J. Bloemer, A.S. Pethel, J.P. Dowling, C.P. Bowden, A.S. Manka, and A.S. Dowling “Transparent metallo-dielectric, one-dimensional, photonic band-gap structures,” J. Appl. Phys., **83**, 2377 – 2382 (1998).

19. J. Yu, Y. Shen, X. Liu, R. Fu, J. Zi, and Z. Zhu, “Absorption in one dimensional metallo-dielectric photonic crystals,” J. Phys Condens Matter., **16**, L51-L56 (2004).

20. A. Christ, S.G. Tikhodeev, N.A. Gippius, J. Kuhl, and H. Giessen, “Waveguide-Plasmon Polaritons: Strong coupling of Photonic and Electronic Resonances in a Metallic Photonic crystal slab,” Phys. Rev. Lett., **91**, 183901-4 (2003).

21. R.S. Bennink, Y.K. Yoon, R.W. Boyd, and J.E. Sipe, “Accessing the Optical Nonlinearity of Metals with Metal-Dielectric Photonic Bandgap Structures,” Opt. Lett*.,* **24**, 1416 -1418 (1999).

22. R.S. Bennink, Y.K. Yoon, R.W. Boyd, and J.E. Sipe, “Accessing the Optical Nonlinearity of Metals with Metal-Dielectric Photonic Bandgap Structures,” Opt. Lett,. **24**, 1416 -1418 (1999).

23. J.L. Zhang, H.T. Jiang, S. Enoch, G. Tayeb, B. Gralak, and M. Lequime, "Two-dimensional complete band gaps in one-dimensional metal-dielectric photonic structures," Appl. Phys. Lett., **92**, 053104 (2008).

24. R.W. Boyd, R.J. Gehry, G.L. Fishery, and J.E. Sipe, " Nonlinear optical properties of nanocomposite materials," J.E, Pure Appl. Opt., **5**, 505-512 (1996).

25. N.N. Lepeshkin, A. Schweinsberg, G. Piredda, R.S Bennink, and R.W. Boyd, "Enhanced Nonlinear Optical Response of One-Dimensional Metal-Dielectric Photonic Crystals," Phys. Rev. Lett., **93**, 123902 (2004).

26. D.D. Smith, G. Fischer, R. Boyd, and D.A. Gregory, "Cancellation of photoinduced absorption in metal nanoparticle composites through a counterintuitive consequence of local field effects," J. Opt. Soc. Am. B., **14**, 1625-1631 (1997).

27. R.L. Nelson, and R.W. Boyd, "Enhanced electro-optic response of layered composite materials," Appl. Phys. Lett., **74**, 2417-2419 (1999).

28. T.K. Lee, A.D. Bristow, J. Hubner, H.M. van Driel, "Linear and nonlinear optical properties of Au-polymer metallodielectric Bragg stacks," J. Opt. Soc. Am. B., **23**, 2142-2147 (2006).

29. Lord Rayleigh., " On the Maintenance of Vibrations by Forces of Double Frequency and on the Propagaion of Waves through a Medium Endowed with a Periodic Structure," Phil. Mag., S.5., **24**, 145-159 (1887)

30. E. Yablonovitch, "Inhibited Spontaneous Emission in Solid-State Physics and Electronics," Phys. Rev. Lett., **58**, 2059-2062 (1987).

31. S. John, " Strong Localization of photons in certain disordered dielectric superlattices," Phys. Rev. Lett., **58**, 2486-2489 (1987)

32. V.M. Menon, M. Luberto, N. Valappil, and S. Chatterjee, "Lasing from quantum dots in a spin-coated flexible microcavity," Opt. Express., **16**, 535-540 (2008).

33. L.I. Deych, D. Livdan, and A.A. Lisyansky, "Resonance tunneling of electromagnetic waves through polariton gaps." Phys. Rev. E., **57**, 7254-7258 (1998).

Chapter 5. FUTURE WORK

5.1 Optical Studies of Colloidal Quantum Dot based Photonic Structures

Following up on the work discussed in chapter 3, the reasons for luminescence quenching when quantum dots are embedded in various hosts have to be investigated in greater detail. The faster decay of the drop coated samples of the colloidal quantum dots is speculated to be due to inter dot energy transfer. This needs to be further verified by performing time resolved luminescence measurements in dot clusters of varying concentrations and at several different spectral positions.

Following this quantum dot embedded waveguides will be fabricated and characterized for their linear and nonlinear transmission properties. Microdisk resonators embedded with quantum dots will be investigated for potential lasing applications.

5.2 Nonlinear Optical Properties of Metal Dielectric Nanocomposite Photonic Crystal

In chapter 4 z-scan measurements on the one-dimensional metal dielectric-nanocomposite structure were carried out. In the process of these measurements the beam profile on the sample was investigated. The beam profile is shown in Figure 5.1. Here it is seen that as the sample is translated in and out of focus, the beam distorts itself. Initially this was attributed to the high intensity pulse damaging the sample. However the beam profile returns to its Gaussian form when returned to focus. With the beam returning to its original form while translated along the axis, scattering off the sample was also speculated upon. However at the time of writing this thesis, the exact reason for

this beam profile distortion is not fully understood. This needs to be investigated in greater detail.

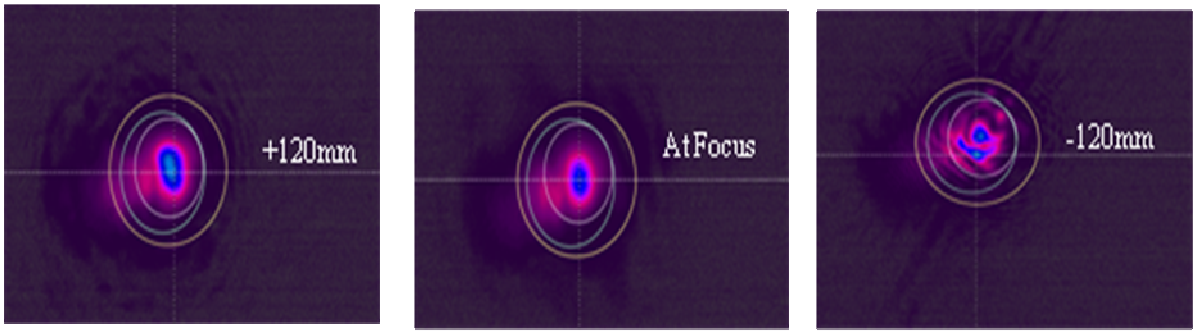

Figure 5.1 Beam profile on sample during z-scan as sample moves in and out of focus

5.3 HYBRID NANOCOMPOSITE

The final state of this project will involve the processing of a composite/structure consisting of metal nanoparticles and quantum dots. The aim is to create a structure consisting of alternating layers of a gain (quantum dots) and loss (metal nanoparticles) medium. Such structures have garnered much interest recently due to ability to demonstrate novel optical phenomena both from a fundamental as well as technological view point. One such example is discussed below.

Structures having compensated gain and loss have been shown to exhibit $\mathcal{PT}$ (Parity-Time reversal) symmetry which leads to the possibility of developing pseudo-Hermitian synthetic materials. A $\mathcal{PT}$ -Symmetric system is described by a non-Hermition Hamiltionian with a real energy spectrum. Recently much work has been done to observe $\mathcal{PT}$ -Symmetry in optics which are able to exhibit interesting optical properties such as

double refraction, power oscillations, nonreciprocal transmission and secondary emission. To obtain $\mathcal{PT}$-Symmetry in optics [1-4] one must choose a "judicious" design involving a combination of gain and/or loss regions. Furthermore composites created using two materials one with an absorptive resonance and the other with a gain can also be explored for achieving lossless negative dielectric constant materials at a single frequency [5]. A negative dielectric constant can be achieved by a material with resonant absorption (e.g. metal nanoparticles) if the secondary component (QDs) has a high oscillator strength and gain (achieved through optical or electrical pumping) to offset the background.

5.4 REFERENCES

1. K.G. Makris, R. El-Ganainy, and D. N. Christodoulides, " Beam dynamics in PT Symmetric Optical Lattices," Phys. Rev. Lett., 100, 103904 (2008)

2. Z. H. Musslimani, K. G. Makris, R. El-Ganainy, and D. N. Christodoulides, " Optical Solitons in PT Periodic Potentials," Phys. Rev. Lett., 100, 030402 (2008)

3. Z.H. Musslimani, K.G. Makris, R. El-Ganainy, and D.N. Christodoulides," Analytical solutions to class of nonlinear Schroedinger equations with PT like potentials," J. Phys. A: Math. Theor. 41, 244019 (2008)

4. O. Bedrix, R. Fleischmann, T. Kottos, and B. Shapiro, " Exponentially fragile PT-Symmetry in Lattices with Localized Eigenmodes,"

5. K. J. Webb, and A. Ludwig, " Semiconductor quantum dot mixture as a lossless negative dielectric constant optical material," Phys. Rev. B., 78, 153303 (2008)

BIBLIOGRAPHY

Chapter 1

1. A. Kongkanand, K. Tvrdy, K. Takechi, M. Kuno, and P.V. Kamat, "Quantum dot solar cells. Tuning Photoresponse through size and shape control of CdSe-TiO_2 Architecture," J. Am. Chem. Soc., **130**, 4007-4015 (2008)

2. J. Zhao, J.A. Bardecker, A.M. Munro, M.S. Liu, Y. Niu, I.K. Ding, J. Luo, B. Chen, and A.K.-Y. Jen, " Efficient CdSe/CdS Quantum Dot Light Emitting diodes using a thermal polmerzied hole transport layer," Nano. Lett., **6**, 463-467 (2006)

3. L.E. Brus, "Electron-electron and electron-hole interactions in small semiconductor crystallites: The size dependence of the lowest excited electronic state," J. Chem. Phys., **80**, 4403–4409 (1984)

4. L. Novotny, and B. Hecht, "Principles of Nano-Optics," Cambridge University Press, New York (2006)

5. P.N. Prasad, " Nanophotonics," John Wiley & Sons Inc., Hoboken, New Jersey (2004).

6. V.I. Klimov, " Nanocrystal Quantum Dots: From fundamental photophysics to multicolor lasing," Los Alamos Science., **28** (2003)

7. V.A. Singh, V. Ranjan, and M. Kapoor, "Semiconductor quantum dots: Theory and phenomenology," Bull. Mater. Sci., **3**, 563-569 (1999)

8. Y. Kayanuma, " Quantum-size effects of interacting electrons and holes in semiconductor microcrystals with spherical shape," Phys. Rev. B., **38**, 9797-9805 (1988)

9. A.P. Alivisatos, " Semiconductor Clusters, Nanocrystals, and Quantum dots," Science, New Series., **271**, 5251, 933-937 (1996)

10. Y. Masumoto, and T. Takagahara, "Semiconductor quantum dots: physics, spectroscopy and applications," Springer (2002).

11. D. Gammom, E.S. Snow, B.V. Shanabrook, D. S. Katzer, and D. Park, " Fine Structure Splitting in the Optical Spectra of Single GaAs Dots," Phys. Rev. Lett., **76**, 16 (1996)

12. G. Schmid, " Nanoparticles: from Theory to Application," Wiley-VCH (2010)

13. E.M. Boatman, G.C. Lisensky, and K.J. Nordell, " A Safer, Easier, Faster Synthesis of CdSe Quantum dot Nanocrystals," Jour. Chem. Education., **82**, 169 (2005)

14. H.Q. Nguyen, "Synthesis and Optical properties of CdSe nanocrystals and CdSe/ZnS core shell nanostructures in non-coordinating solvents," Adv. Nat. Sci.: Nanotechnol., **1**, 025004 (2010)

15. D.N Sathyanarayana, " Electronic Absorption Spectroscopy and Related Techniques," Universities Press (India) Limited (2001)

16. J. D. Jackson, "Classical Electrodynamics," Wiley, New York (1999)

17. A. Moores, and F. Goettmann, "The Plasmon band in noble metal nanopartles: an introduction to theory and applications," New J. Chem., **30**, 1121-1132 (2006)

18. G. Mie, "Contributions to the optics of turbid media, particularly colloidal metal suspensions," Ann. Phys. Leipzig., **25**, 377 (1908)

19. D.D. Evanoff, Jr. and G. Chumanov, "Synthesis and Optical Properties of Silver nanoparticles and Arrays," Chem.Phys., ,**6,**1221-1231 (2005)

20. L.M. Liz-Marzan, " Nanometals, formation and color," Materials Today (2004)

21. M. Faraday, Philos. Trans. R. Soc. London., **147**, 145 (1857)

22. S.A. Maier, " Plasmonics: Fundamentals and Applications," Springer Verlag (2007)

23. U. Kreibig, and M. Vollmer, " Optical Properties of Metal Clusters," Springer Series in Material Sciences., **25** (1995)

24. N. Halas, " The optical properties of Nanoshells," Optics and Photonics News., 26-30 (2002)

25. J.J. Mock, M. Barbic, D.R. Smith, D.A. Schultz, and S. Schultz, " Shape effects in Plasmon resonance of individual colloidal silver nanoparticles," J. Chem. Phys., **116**, 6755-6759 (2002)

26. K. L. Kelly, E. Coronado, L.L Zhao, and G. C. Schatz, " The optical properties of metal nanoparticles : The influence of Size, Shape and Dielectric Environment," J. Phys. Chem. B.,**107**, 668-677 (2003)

27. J.J. Mock, D.R. Smith, and S. Schultz, " Local Refractive Index Dependence of Plasmon Resonance Spectra from Individual Nanoparticles," Nanoletters, **3**, 485-491 (2003)

28. J.R. Sambles, G.W. Bradbery, and F. Yang, "Optical excitation of surface plasmons: an introduction," Contemporary Physics, **32**, 173-183 (1991)

29. R.W. Boyd, " Nonlinear Optics," Academic Press, Second Edition (2003)

30. M.G. Papadopoulos, A. J. Sadlej, and J. Leszczynski, "Non-linear optical properties of matter," Springer (2006)

Chapter 2

1. FluoroHub User Guide, Single photon counting controller, Courtesy of HORIBAJOBIN YVON

2. David L. Andrews, and Andrey A. Demidov, " An Introduction to Laser Spectroscopy," Second Edition, Springer (2002)

3. Ralf Menzel, " Photonics: Linear and Nonlinear Interactions of Laser Light and Matter," Springer- Verlag (2001)

4. L. Novotny, and B. Hecht, " Principles of Nano-Optics," Cambridge University Press (2006)

5. D.N. Sathyanarayana, " Electronic Absorption Spectroscopy and Related Techniques," Universities Press (India) Limited (2001)

6. Guide to using WVASE 32, Courtesy of J.A. Woollam Co., Inc

7. M. Sheikh-Bahae, A.A. Said, and E.W. Van Stryland, " High Sensitivity, Single Beam n_2 Measurements," Opt. Lett., **14**, 955-957 (1989)

8. M. Sheik-Bahae, A.A. Said, T.H. Wei, D.J. Hagan, and E.W. Van Stryland, " Sensitive Measurements of Optical Nonlinearities Using a Single Beam," Journal of Quantum Electronics., **26**, 760-769 (1990)

9. H. Shen, B.L. Cheng, G.W. Lu, D.Y. Guan, Z.H. Chen, and G.Z. Yang, " Picosecond nonlinear optical responses of Au/PVP composite films," J. Phys. D: Appl. Phys., **39**, 233-236 (2006)

10. E. Shahriari, and W.M Mat Yunus, " Single Beam Z-Scan Measurements of Nonlinear Refraction and Nonlinear Absorption coefficients in Silver Nano-Fluid," Amer. J. of Engineering and Applied Sciences., **3**, 98-101 (2010)

11. C. Fuentes-Hernandez, L.A. Padilha, D. Owens, S.Y. Tseng, S. Webster, J.Y. Cho, D. Hagan, E.W. van Stryland, S.R. Marder, and B. Kippelen, " Linear and nonlinear optical properties of highly transmissive one-dimensional metal-organic photonic band gap structures," Proc. Of SPIE., **7049**, 704900 (2008)

12. P.R. Griffiths, and J.A. De Haseth, " Fourier Transform Infrared Spectrometry," Wiley-Interscience (2007)

13. A. Kumer, and G.M. Whiteside, " Features of gold having micrometer to centimeter dimensions can be formed through a combination of stamping with elastomeric stamp and an alkanethio 'ink' followed by chemical etching," Appl. Phys. Lett., **63**, 2002-4 (1993).

14. Y.N. Xia, and G.M. Whitesides, Soft lithography, Angewandte Chemie-International Edition, **37**, 551-575 (1998).

15. S. Franssila, " Introduction to Microfabrication," John Wiley and Son (2010)

16. S.Nonogaki, T. Ueno and T. Ito, "Microlithography fundamentals in semiconductor devices and fabrication," CRC Press (1998)

17. H.J. Levinson, " Principles of Lithography," SPIE Press (2005)

18. User Guide of Quanta 200F (2007)

Chapter 3

1. A. Kongkanand, K. Tvrdy, K. Takechi, M. Kuno, and P.V. Kamat, "Quantum dot solar cells. Tuning Photoresponse through size and shape control of CdSe-TiO_2 Architecture," J. Am. Chem. Soc., **130**, 4007-4015 (2008)

2. J. Zhao, J.A. Bardecker, A.M. Munro, M.S. Liu, Y. Niu, I.K. Ding, J. Luo, B. Chen, and A.K.-Y. Jen., " Efficient CdSe/CdS Quantum Dot Light Emitting diodes using a thermal polmerzied hole transport layer," Nano. Lett., **6**, 463-467 (2006)

3. P. Guyot-Sionnest, and M.A. Hines, " Intraband transitions in semiconductor nanocrystals," Appl. Phys. Lett., **72**, 6, (2008)

4. B.L. Wehrenberg, C. Wang, and P. Guyot-Sionnest, " Interband and intraband Optical studies of PbSe Colloidal Quantum Dots," J. Phys.Chem. B., **106**, 10634-10640 (2002)

5. M. Shim, S.V. Shilov, M.S. Braiman, and P Guyot-Sionnest, " Long-Lived Delocalized Electron States in Quantum Dots : A Step-Scan Fourier Transform Infrared Study," J. Phys. Chem. B., **104**, 1494-1496 (2000)

6. P. Snee, Y. Chan, D. Nocera, and M. Bawendi, " Whispering-Gallery-Mode lasing from a semiconductor nanocrystal laser," Appl. Phys. Let., **80**, 4614-4616 (2002).

7. A.V. Malko, A.A. Mikhailovsky, M.A. Petruska, J. A. Hollingsworth, H. Htoon, M.G. Bawendi, and V. I. Klimov, " From amplified spontaneous emission to microring lasing using nanocrystal quantum dot solids," Appl. Phys. Lett., **81**, 1303-1305 (2002).

8. C. Finlayson, D. Ginger, and N. Greenham, " Optical microcavities using highly luminescence films of semiconductor nanocrystals," Appl. Phys. Lett., **77**, 2500-2502 (2000)

9. P. Lodahl, A. Floris van Driel, I.S. Nikolaev, A. Irman, K. Overgaag, D. Vanmaekelbergh, and W. L. Vos, " Controlling the dynamics of spontaneous emission from quantum dots by photonic crystals," Nature., **430**, 654-657 (2004)

10. C. Poitras, M. Lipson, H. Du, M. Hahn, and T. Krauss, " Photoluminescence enhancement of colloidal quantum dots in a monolithic microcavity," Appl. Phys. Lett., **82**, 4032-4034 (2003)

11. M. Kahl, T. Thomay, V. Kohnle, K. Beha, J. Merlein, M. Hagner, A. Halm, J. Ziegler, T. nann, Y. Fedutik, U. Woggon, M. Artemyev, F. P. Willard, A. Leitenstorfer, and R. Braschitsch, " Colloidal quantum dots in all-dielectric high-Q pillar microcavities," Nano. Lett., **7**, 2897-2900 (2007)

12. K. Srinivasan, M. Borselli, O. Painter, A. Stintz, and S.Krishna., " Cavity Q, mode volume, and lasing threshold in small diameter AlGaAs microdisk with embedded quantum dots," Optics Express, **14**, 1094 (2006)

13. A. Yariv, " Critical Coupling and Its Control in Optical Waveguide-Ring Resonator systems," IEEE Photonics Technology Letters., **14**, 483-485 (2002).

14. A. Yariv, "Univeral relations for coupling of optical power between microresonators and dielectric waveguides," Electronics Letters., **36**, 4 (2000)

15. M.K. Chin, and S.T. Ho, " Design and Modelling of Waveguide Coupled Single Mode microring Resonators," Journal of Lightwave Technology., **16**, 8 (1998).

16. S.O. Kasap, " Optoelectronics and Photonics, Principles and Practices," Prentice Hall Inc., (2001)

17. K. Srinivasan, A. Stintz, S. Krishna, and O. Painter, " Photoluminescence Measurements of quantum-dot containing semiconductor microdisk resonators using optical fiber taper waveguides," Phys. Rev. B., **72**, 205318 (2005).

18. K. Srinivasan, and O. Painter, " Mode coupling and cavity-quantum dot interactions in a fiber-coupled microdisk cavity," Phys. Rev. A., **75**, 023814 (2007).

19. M. Pelton, C. Santori, J. Vuckovic, B. Zhang, G.S. Soloman, J. Plant, and Y. Yamamoto, " Efficient source of single photons: A single quantum dot in a micropost microcavity," Phys. Rev. Lett., **89**, 23 (2002).

20. P. T. Snee, Y. Chan. D.G. Nocera, and M.G. Bawendi, " Whispering-Gallery-Mode Lasing from a semiconductor nanocrystal/microsphere resonator composite," Adv. Mater., **17**, 11

21. J. Furst, H. Pascher, T. Schwarzl, M. Boberl, W. Heiss, G. Springhol, and G. Bauer, "Midinfrared IV-VI vertical-cavity surface-emitting lasers with zero-, two-,and three-dimensional systems in the active region," Appl. Phys. Lett., **81**, 2. (2002)

22. A. Mata, A.J. Fleischman, and S. Roy, "Fabrication of multi-layer SU-8 microstaructures," J. Micromech. Microeng., **16**, 276-284 (2006)

23. L. Pang, K. Tetz, Y. Shen, C.H. Chen, and Y. Fainman, " Photosensitive quantum dot composites and their applications in optical structures," J. Vac. Sci. Technol. B., **23** (2005)

Chapter 4

1. G. Chumanov, and D.D. Evanoff Jr , " Synthesis and Optical Properties of Silver nanoparticles and Arrays," Chem Phys., **6**, 1221-1231 (2005)

2. S. Porel, S. Singh, S.S. Harsha, D.N. Rao, and T.P. Radhakrishanan, "Nanoparticle-Embedded Polymer: In Situ Synthesis, Free-Standing Films with Highly Monodisperse Silver Nanoparticles and Optical Limiting," Chem. Mater., **17**, 9-12 (2005)

3. J.C Maxwell Garnett, "Colors in metal glasses and in metallic films," Philosophical Transactions of the Royal Society of London. Series A., Containing Papers of a Mathematical of Physical Character., **203**, 385-420 (1904).

4. A. Moores, and F. Goettmann, " The Plasmon band in noble metal nanoparticles: an introduction to theory and applications," New J. Chem., **30**, 1121-1132 (2006)

5. R.J. Gehr, and R.W. Boyd, " Optical Properties of Nanostructures Optical Materials," Chem. Mater., **8**, 1807-1819

6. J.A. Woolam Co., Inc, Guide to using WVASE- Spectroscopic Ellipsometers and Thin film Characterization.

7. P. Lodahl. P, A.F van Driel, I.S Nikolaev, A. Irman, K. Overgaag, D. Vanmaekelbergh, and W.L Vos, "Controlling the dynamics of spontaneous emission from quantum dots by photonic crystals," Nature., **430**, 654-657 (2004).

8. Y.A. Vlasov, M. O'Boyle, H.F. Hamann, and S.J. McNab, "Active control of slow light on a chip with photonic crystal waveguides," Nature., **438**, 65-69 (2005).

9. H. Gersen, T.J. Karle, R.J.P. Engelen, W. Bogaerts, J.P. Korterik, N.F. val Hulst, T.F Krauss, and L. Kuipers, "Real space observation of ultraslow light in photonic crystal waveguides," Phys. Rev. Lett., **94**, 073903 (2005).

10. D. Goldberg, L.I. Deych, A.A. Lisyansky, Z. Shi, V.M. Menon, V. Tokranov, M. Yakimov, and S. Oktyabrsky, "Exciton-lattice polaritons in multiple-quantum-well-based photonic crystals," Nat. Photonics., **3**, 662-666 (2009).

11. B. Temelkuran, E. Ozbay, J.P. Kavanaugh, G. Tuttle, and K.M. Ho, "Resonant cavity enhanced detectors embedded in photonic crystals," Appl. Phys. Lett., **72**, 2376 (1998).

12. M. Lee, and P.M. Fauchet, “Two-Dimensional Silicon Photonic Crystal Based Biosensing Platform For Protein Detection,” Opt. Express., **15**, 4530-4535 (2007).

13. H. Kosaka, T. Kawashima, “Superprism phenomena in photonic crystals,” Phys. Rev. B., **58**, 10096-10099 (1998).

14. T. Ochiai, and J. Sanchez-Dehesa, “Superprism effect in opal-based photonic crystals,” Phys. Rev. B., **64**, 245113 (2001).

15. N. N. Lepeshkin, W. Kim, V.P. Safonov, J.G. Zhu, R.L. Armstrong, C.W. White, R.A. Zuhr, and V.M. Shalaev, “ Optical Nonlinearities of Metal Dielectric Composites,” Journal of Nonlinear Optical Physics and Materials., **8**, 191-210 (1999)

16. V. Kuzmiak, and A.A. Maradudin, "Photonic band structures of one- and two-dimensional periodic systems with metallic components in the presence of dissipation," Phys. Rev. B., **55**, 7427 (2007).

17. K.A. McIntosh, L.J. Mahoney, K.M. Molvar, O.B. McMahon, S. Verghese, M. Rothschild, and E.R. Brown, “Three-dimensional metallodielectric photonic crystals exhibiting resonant infrared stop bands,” Appl. Phys. Lett., **70**, 2937-2939 (1997).

18. M. Scalora, M.J. Bloemer, A.S. Pethel, J.P. Dowling, C.P. Bowden, A.S. Manka, and A.S. Dowling “Transparent metallo-dielectric, one-dimensional, photonic band-gap structures,” J. Appl. Phys., **83**, 2377 – 2382 (1998).

19. J. Yu, Y. Shen, X. Liu, R. Fu, J. Zi, and Z. Zhu, “Absorption in one dimensional metallo-dielectric photonic crystals,” J. Phys Condens Matter., **16**, L51-L56 (2004).

20. A. Christ, S.G. Tikhodeev, N.A. Gippius, J. Kuhl, and H. Giessen, “Waveguide-Plasmon Polaritons: Strong coupling of Photonic and Electronic Resonances in a Metallic Photonic crystal slab,” Phys. Rev. Lett., **91**, 183901-4 (2003).

21. R.S. Bennink, Y.K. Yoon, R.W. Boyd, and J.E. Sipe, “Accessing the Optical Nonlinearity of Metals with Metal-Dielectric Photonic Bandgap Structures,” Opt. Lett*.,* **24**, 1416 -1418 (1999).

22. R.S. Bennink, Y.K. Yoon, R.W. Boyd, and J.E. Sipe, “Accessing the Optical Nonlinearity of Metals with Metal-Dielectric Photonic Bandgap Structures,” Opt. Lett,. **24**, 1416 -1418 (1999).

23. J.L. Zhang, H.T. Jiang, S. Enoch, G. Tayeb, B. Gralak, and M. Lequime, "Two-dimensional complete band gaps in one-dimensional metal-dielectric photonic structures," Appl. Phys. Lett., **92**, 053104 (2008).

24. R.W. Boyd, R.J. Gehry, G.L. Fishery, and J.E. Sipe, " Nonlinear optical properties of nanocomposite materials," J.E, Pure Appl. Opt., **5**, 505-512 (1996).

25. N.N. Lepeshkin, A. Schweinsberg, G. Piredda, R.S Bennink, and R.W. Boyd, "Enhanced Nonlinear Optical Response of One-Dimensional Metal-Dielectric Photonic Crystals," Phys. Rev. Lett., **93**, 123902 (2004).

26. D.D. Smith, G. Fischer, R. Boyd, and D.A. Gregory, "Cancellation of photoinduced absorption in metal nanoparticle composites through a counterintuitive consequence of local field effects," J. Opt. Soc. Am. B., **14**, 1625-1631 (1997).

27. R.L. Nelson, and R.W. Boyd, "Enhanced electro-optic response of layered composite materials," Appl. Phys. Lett., **74**, 2417-2419 (1999).

28. T.K. Lee, A.D. Bristow, J. Hubner, H.M. van Driel, "Linear and nonlinear optical properties of Au-polymer metallodielectric Bragg stacks," J. Opt. Soc. Am. B., **23**, 2142-2147 (2006).

29. Lord Rayleigh., " On the Maintenance of Vibrations by Forces of Double Frequency and on the Propagaion of Waves through a Medium Endowed with a Periodic Structure," Phil. Mag., S.5., **24**, 145-159 (1887)

30. E. Yablonovitch, "Inhibited Spontaneous Emission in Solid-State Physics and Electronics," Phys. Rev. Lett., **58**, 2059-2062 (1987).

31. S. John, " Strong Localization of photons in certain disordered dielectric superlattices," Phys. Rev. Lett., **58**, 2486-2489 (1987)

32. V.M. Menon, M. Luberto, N. Valappil, and S. Chatterjee, "Lasing from quantum dots in a spin-coated flexible microcavity," Opt. Express., **16**, 535-540 (2008).

33. L.I. Deych, D. Livdan, and A.A. Lisyansky, "Resonance tunneling of electromagnetic waves through polariton gaps." Phys. Rev. E., **57**, 7254-7258 (1998).

Chapter 5

1. K.G. Makris, R. El-Ganainy, and D. N. Christodoulides, " Beam dynamics in PT Symmetric Optical Lattices," Phys. Rev. Lett., 100, 103904 (2008)

2. Z. H. Musslimani, K. G. Makris, R. El-Ganainy, and D. N. Christodoulides, " Optical Solitons in PT Periodic Potentials," Phys. Rev. Lett., 100, 030402 (2008)

3. Z.H. Musslimani, K.G. Makris, R. El-Ganainy, and D.N. Christodoulides," Analytical solutions to class of nonlinear Schroedinger equations with PT like potentials," J. Phys. A: Math. Theor. 41, 244019 (2008)

4. O. Bedrix, R. Fleischmann, T. Kottos, and B. Shapiro, " Exponentially fragile PT-Symmetry in Lattices with Localized Eigenmodes,"

5. K. J. Webb, and A. Ludwig, " Semiconductor quantum dot mixture as a lossless negative dielectric constant optical material," Phys. Rev. B., 78, 153303 (2008)